Break the Trilemma: design of high-loading, high-capacity, high-stability zinc-ion battery cathode towards industrialization

Xuan Gao
A thesis presented for the degree of
Doctor of Philosophy

Supervised by
Professor Claire J. Carmalt
Professor Ivan P. Parkin

Department of Chemistry
Mathematical and Physical Sciences Faculty
University College London
20 May 2025

Declaration

I, Xuan Gao, confirm that the work presented in this thesis is my own. Where information has been derived from other sources (publications, websites, and databases), I confirm that this has been indicated in the thesis. All the Figures from publications (including my own work) have obtained their copyright permission from the journal publisher.

Abstract

Aqueous zinc-ion batteries (AZIBs) are increasingly seen as promising options for stationary energy storage, given their high volumetric capacity, intrinsic safety, and affordability. To enable their widespread adoption for large-scale applications, improvements in AZIB performance and stability, particularly in cathode materials like MnO_2, are essential. Enhancing cathode properties—specifically achieving high-loading, high-capacity, and high-stability—is critical for AZIBs industrialization. High-loading cathodes accommodate more active material per unit area, increasing energy density and reducing the battery's footprint. High-capacity cathodes store more energy per unit mass or volume, crucial for applications requiring long-duration energy storage, such as grid-level energy balancing. Moreover, high-stability cathodes ensure long-term performance and reliability, crucial for industrial environments where downtime is costly. Nevertheless, with the escalation of unit mass loading, the dynamics of electron and ion transport within the electrode diminish, significantly impacting both capacity and cycle stability. This phenomenon is commonly referred to as the "Trilemma" in battery technology. This thesis proposes a decoupling enhancement strategy for surface and bulk materials to achieve these cathode properties simultaneously, advancing AZIBs industrialization. By focusing on electron and ion transport dynamics in Mn-based cathodes of AZIBs, the research develops a high-loading cathode based on designs of electrode structure (free-standing three-dimensional network), material property (double-ion pre-intercalation), fabrication process design (slurry treatment), facilitating high-loading cathode applications in Ah-level full cells. The study employs physicochemical and electrochemical characterizations, along with ex-situ material characterization and computational simulations, to elucidate cathode engineering details. Overall, this research aims to address critical factors in AZIBs development, laying the groundwork for their widespread industrial use in energy storage applications. The PhD project encompasses three primary works, outlined below:

(1) MnO_2-based cathodes in AZIBs offer stability and safety yet face challenges in slow kinetics due to low electrical conductivity, crucial for rapid charging devices. Addressing these hurdles, a sodium-intercalated manganese oxide (NMO) with 3D varying thinness carbon nanotubes (VTCNTs) network is proposed as a binder-free cathode (NMO/VTCNTs) without heat treatment. This novel network, utilizing low-

thinness CNTs (LTCNTs) and high-thinness CNTs (HTCNTs), enhances specific capacity and mass loading. The interconnected CNTs withstand deformation, providing extra Zn^{2+} storage and efficient ion/electron migration routes. The NMO is evenly distributed within CNTs, improving structural stability and transport rates. The cathodes achieve loading of 5 mg cm^{-2}, retaining high specific capacities of 329 mAh g^{-1} after 120 cycles at 0.2 A g^{-1}, 225 mAh g^{-1} after 200 cycles at 1 A g^{-1}, and 158 mAh g^{-1} after 1000 cycles at 2 A g^{-1}. This construction strategy offers insights into achieving high mass loading and capacity, presenting significant potential for industrial application.

(2) This study introduces a dual-ion co-intercalation strategy to enhance Mn-based cathodes in AZIBs. By incorporating both sodium and copper ions into δ-MnO_2 (NCMO), stable cycling performance and high specific capacity are simultaneously achieved, even under high mass loading. Pre-intercalated Na^+ boosts the Cu^{2+}-driven activation of the Mn^{2+}/Mn^{4+} redox process, while the smaller ionic radius of Cu^{2+} accelerates diffusion for improved charge/discharge kinetics. At lower mass loadings, the synergistic action of Na^+ and Cu^{2+} sustains a prolonged capacity enhancement, whereas at higher loadings it enables a reversible Mn deposition/dissolution process. *Ex-situ* XRD and XPS analyzes clarify how Cu^{2+} promotes these redox dynamics. Remarkably, the NCMO cathode displays a continuous activation process under low mass loading condition, delivering 576 mA h g^{-1} capacity after 100 cycles at 0.5 A g^{-1}. Under higher mass loading (~10.9 mg cm^{-2}), it exhibits a high areal capacity of 2.10 mA h cm^{-2} at 1.09 mA cm^{-2}. These findings underscore co-intercalated Mn-based cathodes as promising candidates for practical, high-performance energy storage applications.

(3) In this study, acetic acid (HAc) was introduced during the mixing process to enhance the chemical activity of the cathode surface. This addition led to notable improvements, particularly under low loading conditions, where the surface ratio increased, resulting in a very high specific capacity and prolonged activation process of the cathode. As the loading gradually increased, the activation process diminished due to a decrease in the surface ratio. Remarkably, the traditional coating process achieved a high load capacity of 21 mg cm^{-2}. Moreover, the 8 Ah pouch cell with the

HAc-treated cathodes exhibited an impressive 89% capacity recovery in the 100th cycle at a current density of 0.2 A g^{-1}. These results underscore the effectiveness of HAc treatment in enhancing cathode performance, highlighting its potential for practical application in battery technology. Investigations into the underlying mechanisms and optimization based on *in-situ* Raman *ex-situ* XRD, *ex-situ* XPS, and X-ray Computed Tomography (XCT) of the HAc treatment process has been discussed for more significant advancements in AZIBs electrochemical performance and lifespan.

Impact statement

This PhD project emphasizes the understanding and development of high-loading cathodes and their fabrication engineering in achieving high-capacity and high-stability for rechargeable aqueous zinc ion batteries (AZIBs) in practical use. The impact and highlights of this thesis were summarized below:

(1) In the first study, a free-standing, binder-free cathode was developed for AZIBs that exhibits excellent specific capacity and cycle stability. In addition to improving the loading capacity per unit area, this work also explores strategies to enhance ion transport at the interface between NMO and CNTs. The energy storage mechanism based on NMO/VTCNTs was first studied, and then detailed *ex-situ* characterizations and DFT simulation were performed. By comparison with traditional NMO cathodes, its excellent electrochemical performance was verified by cyclic voltammogram (CV), galvanostatic cycle tests, and high-rate tests. The most important achievements are summarized below:

i. This study introduces a pioneering strategy for creating Mn-based, free-standing cathodes without the use of binders, utilizing carbon nanotubes of varying thinness (VTCNTs). The approach increases the mass loading of active materials per unit area while simultaneously enhancing ionic and electronic conductivity, all without compromising the electrode's flexibility—an essential feature for potential applications in electronics and portable devices. The resulting cathodes demonstrate exceptional capacity performance and long-term cycling stability in zinc-ion batteries (ZIBs), representing a significant advancement in the field of cathode technology for energy storage applications. These free-standing, binder-free cathodes demonstrate favorable capacity—329 mAh g^{-1} after 120 cycles at 0.2 A g^{-1} and 225 mAh g^{-1} after 200 cycles at 1 A g^{-1}—along with sustained cycling stability, maintaining 158 mAh g^{-1} at 2 A g^{-1} over 1000 cycles.

ii. Insights into Nanocomposite Interfaces. Through density functional theory (DFT) calculations, this work offers insights into the ion conduction channels at the interface of CNTs and NMO, providing valuable information for the study of nanocomposite interfaces. This understanding not only enhances our knowledge of the fundamental properties of nanomaterials but also guides future research in optimizing the design of composite materials for improved battery performance and stability.

iii. Scalability and Industrial Relevance. The proposed strategy not only offers scalability but also introduces a crucial aspect of flexibility, catering to the evolving demands of diverse applications, especially those requiring flexible energy storage solutions. By incorporating varying thinness carbon nanotubes (CNTs) into the cathode design, the research enables the development of flexible battery electrodes with high mass loading and capacity. This flexibility opens doors to a wide range of industrial applications, including wearable electronics, flexible displays, and bendable energy storage devices. Moreover, the scalable nature of the proposed approach ensures its feasibility for large-scale production processes, essential for meeting the growing demand for advanced battery technologies in various industries. The ability to mass-produce flexible, high-capacity cathodes using readily available materials like CNTs slurry represents a significant step towards the commercialization and widespread adoption of flexible energy storage solutions.

(2) In this study, co-intercalation was explored as a strategy to enhance the performance of δ-MnO_2 cathodes in AZIBs. By fabricating Na^+ and Cu^{2+} co-intercalated δ-MnO_2 (NCMO) cathodes, the activation effect of Cu^{2+} for the Mn^{2+}/Mn^{4+} redox pair conversion was amplified, leading to higher specific capacity and cycling stability in high mass loading. The achievements are as follows:

i. The synergistic mechanism of Na^+ and Cu^{2+}. Owing to its smaller ionic radius, Cu^{2+} diffuses more readily into the electrolyte, thereby expediting the redox reactions throughout the charge/discharge process. The co-intercalation of Na^+ and Cu^{2+}, along with the deposition and dissolution of $Zn_xMnO(OH)_y$ and ZHS, enabled prolonged capacity increase at low mass loadings and highly reversible Mn deposition/dissolution at high mass loadings.

ii. Surface and bulk phase decoupling enhancement strategy. This study integrates electrochemical testing and *ex-situ* characterization to validate a strategy aimed at enhancing the surface chemistry and bulk microstructure stability of Mn-based cathode materials. The dual-ion co-intercalation approach simultaneously facilitates Mn^{2+}/Mn^{4+} two-electron transfer on the surface while ensuring the stability of the host material, particularly under high-mass loading conditions.

iii. Achievement of excellent high-rate performance with high retention. Furthermore, NCMO demonstrates outstanding high-rate performance, where a current density of 2 A g^{-1} was applied to assess its cycling performance. AZIBs equipped with NCMO cathodes exhibit nearly 100% capacity retention, with a specific capacity of 200 mA h g^{-1} after 1000 cycles.

(3) In the third study, the development and optimization of the production of prototype AZIBs for high-power and high-safety energy storage is discussed. By integrating acetic acid (Hac) into the cathode slurry mixing process, the research achieved enhanced proton dehydration and intercalation, leading to improved power density and cycling stability for high mass loading cathodes. This modification allowed the conversion of a lithium-ion battery production line to produce AZIBs efficiently, significantly reducing costs and increasing the power density and production capacity.

i. Cathode Optimization with Acetic Acid. The research introduced HAc into the cathode slurry mixing process of AZIBs, which significantly enhanced proton dehydration and intercalation at the cathode. This method improved the power density and electrochemical stability of high mass loading cathodes, crucial for high-performance energy storage applications.

ii. Production Line Adaptation. The study demonstrated the successful adaptation of a lithium-ion battery production line for manufacturing AZIBs, which led to a 44.2% increase in power production capacity and a reduction in production costs, making the process more efficient and scalable.

iii. Superior Performance and Cost Efficiency. AZIB prototypes showcased remarkable cycling stability with 98% capacity retention after 100 cycles and lower production costs. These batteries offer a cost-effective alternative to traditional lithium-ion batteries for high-power applications, emphasizing their potential in sustainable energy storage solutions.

These advancements, encompassing both mechanistic insights and material innovations, are poised to expedite the progress of zinc-ion batteries in both academic research and commercialization endeavors. The comprehension of high-loading cathodes and advancements in fabrication engineering offer a versatile approach to bolster battery stability, addressing concerns from the perspective of decoupling of surface and bulk. Transitioning from fundamental physiochemical understanding to enhanced electrochemical performance, the evolution of AZIBs holds promise for transitioning from laboratory settings to widespread market adoption.

Acknowledgements

First and foremost, I would like to extend my deepest gratitude to my principal supervisor, Prof. Claire J. Carmalt. Her unwavering support and guidance were pivotal in igniting my determination to pursue a research career, especially during the challenging initial phase of my doctoral journey. Her meticulous approach to scientific inquiry instilled in me the core ethics of research, an invaluable lesson that will guide me throughout my life. Prof. Carmalt's transformative influence provided both a guiding light and a source of inspiration, shaping the direction and success of my work and making her an indispensable mentor. I am also profoundly thankful to my subsidiary supervisor, Prof. Ivan P. Parkin. His expertise, confidence in my abilities, and consistent encouragement have played a crucial role in my growth as a researcher. Prof. Parkin's depth of knowledge, combined with his rigorous approach to problem-solving, has significantly expanded my academic perspective. Together, Prof. Carmalt and Prof. Parkin created an environment that fostered intellectual curiosity, perseverance, and academic integrity. Their mentorship not only reinforced my commitment to scientific excellence but also prepared me to face future challenges with confidence. I remain truly grateful for their guidance, patience, and belief in my potential.

I am particularly grateful to my co-supervisor, Dr. Guanjie He, whose pioneering work in zinc-ion batteries laid the foundation for my research project and publications. His profound academic insight and fervent dedication to research have been instrumental in driving me to deliver research of the highest caliber. Furthermore, my gratitude extends to Prof. Paul Shearing, my esteemed visiting research advisor at the University of Oxford, who honed my experimental skills. Prof. Shearing's mastery in sophisticated research techniques profoundly broadened my analytical capabilities and offered me a more comprehensive understanding of my field. His supportive guidance and valuable critiques during my stay at Oxford played a crucial role in the refinement of my research questions and methods, significantly augmenting the caliber of my thesis. Their mentorship has been vital in achieving the milestones in my research career.

In addition, I would like to extend my gratitude to all my collaborators throughout my

doctoral studies, including Prof. Dan Brett and Prof. Christ Howard at UCL. My thanks also go to the technicians and departmental staff for their invaluable support and training, which significantly contributed to the progress of my research. I am particularly appreciative of the members of Prof. Claire Carmalt's and Prof. Ivan Parkin's groups—Dr. Yiyang Liu, Dr. Yuhang Dai, Dr. Haobo Dong, Dr. Chen Shen, Dr. Chengyi Zhang, Dr. Siyu Zhao, Dr. Jianwei Li, Dr. Wei Zong, Dr. Fangjia Zhao, Dr. Tianlei Wang, and Ms. Xueying Hu—whose assistance and friendship enriched my doctoral journey. Working alongside such a dedicated team has been an honor, and I value the lifelong connections we have forged.

Finally, I owe my deepest thanks to my family and girlfriend for their boundless love and steadfast support throughout my PhD. Moreover, the financial support provided by the UCL-CSC scholarship was instrumental in bringing this project to fruition, and I am sincerely thankful for this vital assistance.

Abbreviation

AZIBs	Aqueous zinc-ion batteries
CE	Coulombic efficiency
CV	Cyclic voltammetry
DFT	Density Functional Theory
EDLC	Electrochemical double layer capacitance
EDS	Energy dispersive X-Ray spectrometer
EES	Electrochemical energy storage
EIS	Electrochemical impedance spectroscopy
EW	Electrochemical window
FTIR	Fourier-transform infrared spectroscopy
HER	Hydrogen evolution reaction
LIBs	Lithium-ion battery
OCP	Open circuit potential
OER	Oxygen evolution reaction
PBA	Prussian blue analogue
PTFE	Polytetrafluoroethylene
PVDF	Polyvinylidene fluoride
SEM	Scanning electron microscope
SHE	Standard hydrogen electrode
SPE	Solid polymer electrolyte
STEM	Scanning transmission electron microscopy
TEM	Transmission electron microscopy
TGA	Thermal gravimetric analysis
TMO	Transition metal oxides
WIS	Water-in-salt
XPS	X-ray photoelectron spectroscopy
XRD	X-ray diffractometer

Table of Content

List of Figures

List of Tables

Chapter 1 Literature review

1.1 Introduction

The Paris Agreement, signed by nearly 200 countries, aims to keep this century's global temperature rise well below 2°C above pre-industrial levels—and strive for 1.5°C—while requiring each country to submit and continually update its "Nationally Determined Contributions" (NDCs) to mitigate global warming and encourage clean energy transformation.[1] These commitments are significantly propelling the transition to renewable energy across nations. Solar and wind energy have become the main sources of renewable energy, and the global renewable energy installed capacity is 510 GW in the single year of 2023.[2] Despite their prevalence, the variability and unpredictability of these energy sources pose challenges to the continuous transmission of electricity across the grid, highlighting the critical need for effective energy storage solutions. The role of energy storage devices, particularly batteries, has become increasingly pivotal.[3] These devices are essential for harnessing the power of new energy sources.[4] They also enhance the reliability and stability of electrical grids while simultaneously working to lower energy costs.[5] As societies worldwide strive for cleaner and more reliable energy solutions, the significance of energy storage technologies and their contribution to environmental sustainability is expected to grow exponentially in the foreseeable future.[6] The surge in demand for sustainable energy solutions has catalyzed a flurry of research and development efforts in the realm of energy storage devices. Among the forefront of these endeavors is the pursuit of batteries that are not only more efficient but also safer, more flexible, and cost-effective.[7] This quest involves a comprehensive exploration of novel materials, innovative manufacturing techniques, and advanced designs, all aimed at meeting the stringent requirements of next-generation batteries.[8] Such advancements are crucial for supporting the integration of renewable energy sources into the grid, thereby facilitating a transition towards a more sustainable and eco-friendly energy landscape.[9]

Lithium-ion batteries (LIBs) have been widely adopted because of high energy density, especially ternary (NCM) Li batteries with a high capacity of ~350 Wh kg^{-1}, enabling longer usage periods between charges.[10] This feature is particularly valuable in portable electronics and electric vehicles, where maximizing energy storage within a compact space is crucial.[11] Additionally, LIBs offer higher energy efficiency compared to other battery technologies, with the ability to reduce the loss of energy.[12] However, stationary storage systems, particularly those integrated into the grid, require attributes such as scalability, longevity, and safety. Safety concerns detract from the suitability of LIBs for stationary use.[13] The flammability of the organic electrolytes used in LIBs poses a significant risk, as evidenced by several reported battery fire incidents.[14] These safety issues are particularly critical in stationary storage applications, where the consequences of a fire could be catastrophic.[15] Additionally, the lower power density of LIBs limits their effectiveness in scenarios that require rapid charging or power compensation for the grid.[16] This deficiency underscores the necessity for the development of post-lithium-ion-battery technologies that not only offer high power density and extended lifetimes but also meet stringent safety standards.[17]

Aqueous Zn-ion batteries (AZIBs) represent a burgeoning class of rechargeable batteries that have captured the attention of the research community due to their promising attributes for low-cost, high-safety and high-performance energy storage systems.[18] Leveraging zinc ions as the charge carriers, AZIBs offer a suite of advantages that make them a compelling alternative to their lithium-ion counterparts.[19] Zn, the element central to these batteries, is not only abundant and inexpensive but also boasts an inherently low environmental footprint.[20] This aligns perfectly with the global imperative for sustainable energy solutions that do not compromise on ecological well-being.[21] A critical aspect of AZIBs that significantly influences their performance is the cathode material.[22] The cathode is pivotal in dictating both the capacity and stability of the battery, serving as the linchpin for the efficient storage and release of energy.[23] Consequently, a considerable segment of AZIBs research is dedicated to the optimization of cathode materials, aiming to enhance the energy density, cycle life, and overall efficiency of these batteries.[24] Innovations in cathode technology are thus a focal point, with researchers delving into novel compounds and nano-engineering techniques to unlock the full potential of AZIBs.[25]

Furthermore, the development of AZIBs is not isolated to academic and laboratory settings. There is a growing interest from industry in transitioning these innovations from the bench to the market. This transition requires not only technological breakthroughs but also considerations of scalability, cost-effectiveness, and compatibility with existing infrastructure.[26] As such, the journey of AZIBs from concept to commercial product involves a multidisciplinary approach, encompassing materials science, engineering, economics, and environmental science. As society move forward, the development of AZIBs and other advanced energy storage solutions will be instrumental in addressing the twin challenges of energy security and environmental sustainability.[27] These technologies offer a pathway to a future where renewable energy can be efficiently stored and deployed, ensuring a steady and reliable supply of clean power. The implications for global energy systems are profound, promising a reduction in reliance on fossil fuels, a decrease in carbon emissions, and a significant step towards achieving the ambitious goals of the Paris Agreement.[28]

1.2 Post-lithium-ion batteries

1.2.1 Overview of different energy storage technologies

The evolution of energy storage technologies, particularly those utilizing monovalent cations like Li^+, Na^+, and K^+ ions, alongside multivalent cations such as Zn^{2+}, Mg^{2+}, Ca^{2+}, Al^{3+} and other ions, reflect the growing demand for more efficient and cost-effective solutions.[29] Among these, LIBs stand out as the most prevalent, benefiting from substantial advancements in energy density. However, the exploration of sodium-ion batteries (NIBs) and potassium-ion batteries (KIBs) marks the industry's effort to identify viable alternatives to LIBs due to the escalating costs of Li resources and the pursuit of safer anode materials.[30]

Multivalent cation batteries, employing divalent or trivalent cations, offer a promising avenue due to their potential for promising energy density, abundant reserves, lower raw material prices, and higher safety profiles, as shown in Figure 1.1.[31] These batteries operate on a "rocking chair" mechanism, similar to LIBs, where cations shuttle between electrodes without significantly altering the electrolyte's composition.[32] This similarity leverages the extensive knowledge and manufacturing expertise developed for LIBs, facilitating the transition towards industrial applications of multivalent technologies.[33] Despite their promise, the adoption of multivalent cation batteries hinges on their ability to offer clear advantages over lithium-based counterparts.[34] Concerns such as the lower oxidation-reduction potential of multivalent metals compared to lithium challenge researchers to enhance their performance further.[35] Nonetheless, the higher volumetric energy density of multivalent cation batteries positions them as attractive candidates for next-generation energy storage systems.[35] As research progresses, the field witnesses not only the competition between multivalent and monovalent cation batteries but also an internal competition among various multivalent technologies, each vying for a dominant role in the future of energy storage.

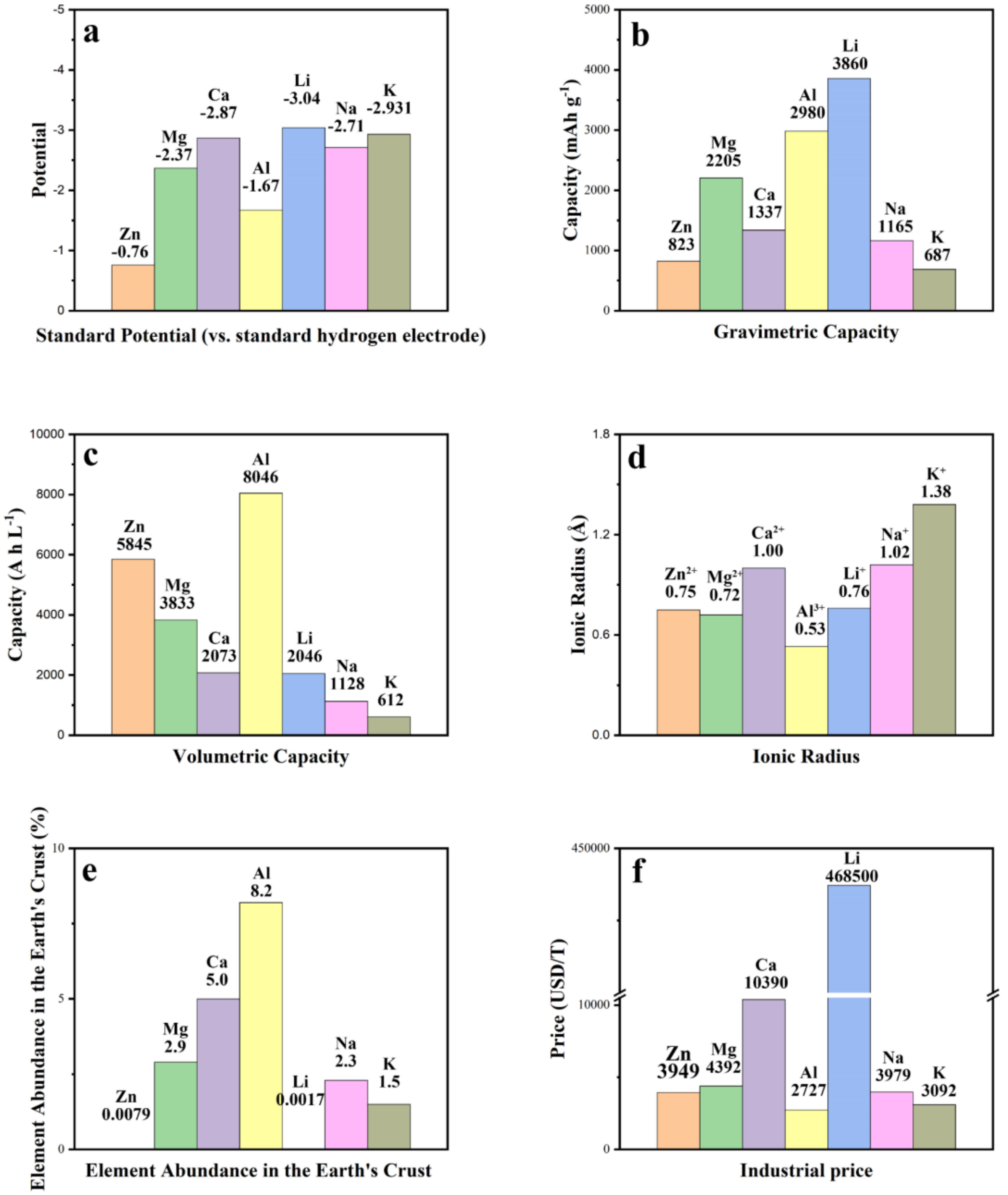

Figure 1.1 (a) Standard potential (vs. standard hydrogen electrode), (b) gravimetric capacity, (c) volumetric capacity, (d) ionic radius, and (e) element abundance in the earth's crust of multivalent metal element Zn, Mg, Ca, Al and monovalent metal element Li, Na, and K, respectively.[29] Reused with permission from The Royal Society of Chemistry.

1.2.2 Maturity of different element-based energy storage technologies

Various energy storage technologies that utilize metal cations as charge carriers are currently being developed at different stages within the industry.[36] Patents play a crucial role in protecting these innovations from being replicated by competitors, offering a robust mechanism for securing commercial advantages.[37] Therefore, analyzing patent trends can provide insightful snapshots of the technological landscape. A review of patent distributions for diverse energy storage technologies reveals notable trends and the leading organizations or companies in each sector, as shown in Figure 1.2.

LIBs, experiencing a surge in patent filings until 2012, began to see a decline from 2017. Japanese firms lead in the Li-ion industrial application.[38] Na-ion technology ranks as the second, with over 3,440 patents filed in the past decade, predominantly by Chinese academic institutions. This suggests a gap in commercialization efforts by Chinese companies in Na-ion technology. Zn-based energy storage technology patents, mainly held by Japanese entities such as Panasonic Co., Ltd, Semiconductor Energy Laboratory, and HITACHI, showed a significant increase in 2017 and 2019, amidst fluctuations in other years. In the arena of KIBs technology, both China and the USA demonstrate strong capabilities, though U.S. patents are mostly held by companies, whereas in China, academic and research institutions predominate. Mg-based and Al-based energy storage technologies see Japan and the Netherlands, respectively, leading in patent filings, although the overall patent count for Mg-based technology remains low. The progress of Ca-based energy storage technology is the slowest among reviewed technologies, with just 1,200 patents issued over the last decade, indicating intense competition and interest from multiple countries, including the UK, USA, Japan, China, and Germany. This diverse patent landscape underscores the dynamic nature of the energy storage sector, with various technologies vying for dominance in the quest for efficient, reliable, and scalable energy storage solutions.

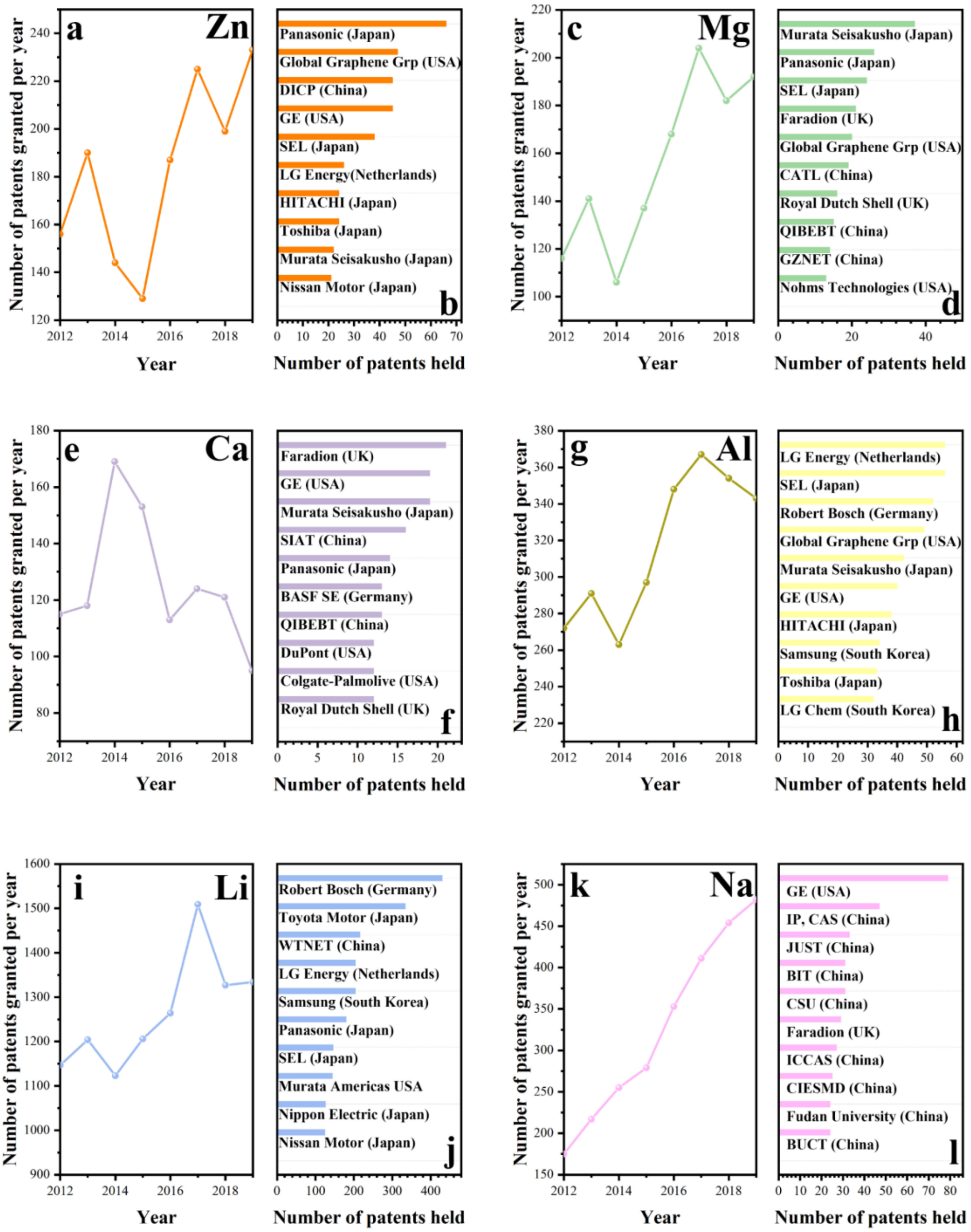

Figure 1.2 Comprehensive Patent Landscape of Various Energy Storage Technologies based on different element of Zn, Mg, Ca, Al, Li, and Na.[29] Reused with permission from The Royal Society of Chemistry.

1.3 Development of aqueous Zn-ion batteries

Advancements in AZIBs are propelling the field of aqueous multivalent cation batteries forward, driven by three key attributes: Zn's abundance, a theoretical volumetric energy density reaching 5855 mAh cm^{-3}, and a notable redox potential of -0.76V versus the Standard Hydrogen Electrode (SHE).[39] This innovation is not the first instance of zinc's utilization in battery technology; its roots trace back to Alessandro Volta's 1799 invention, the Volta Pile.[40] The subsequent centuries saw an evolution in zinc-based batteries, culminating in a variety of types such as Zn-Ag_2O, Zn-NiOOH, Zn-air, and Zn-MnO_2, which once led the primary battery market.[41] Historically, these batteries faced challenges, particularly with the use of alkaline aqueous electrolytes (concentrated KOH), which led to issues like the irreversible zinc dendrites and byproducts, impacting rechargeability due to low Coulombic efficiency (CE).[42] A shift towards mild-acidic aqueous electrolytes, leveraging Zn^{2+} salts like $ZnSO_4$ and $ZnCl_2$, marked a significant turning point.[43] This change enabled a reversible Zn^{2+} transmission process between the cathode and anode, overcoming the limitations associated with alkaline solutions and heralding the era of rechargeable AZIBs.

The discovery of H^+ and Zn^{2+} co-insertion mechanisms in 2018 further accelerated AZIBs development, coinciding with advances in zinc-based flow batteries.[44] These systems, particularly Zn-halogen flow batteries developed in the 1970s, introduced a scalable energy storage solution through an innovative electroplating mechanism.[45] For instance, Zn-Br_2 batteries facilitate energy storage across two tanks, improving efficiency through bromine-adduct oil formation in the catholyte.[46]

Recent explorations into rechargeable Zn-MnO_2 technologies have expanded the scope of Zn-based batteries, though the debate over the reversibility of MnO_2 mechanisms persists.[47] The comprehensive investigation into AZIBs spans cathode materials, Zn anode enhancements, and electrolyte formulation improvements.[48] Focus areas include metal oxides like manganese dioxide and vanadium oxides, Prussian blue analogues (PBAs), etc., illustrating the ongoing quest to refine and optimize AZIBs technology for future energy storage applications.[49]

1.3.1 Fundamentals of rechargeable aqueous Zn-ion batteries

AZIBs are emerging as promising candidates for energy storage systems. These batteries consist of three essential components: the cathode, anode, and electrolyte, as illustrated in Figure 1.3. Zn metal, chosen for its anode due to its suitable standard electrode potential (Zn/Zn^{2+}: -0.76V v.s. SHE) and benign chemical behavior in aqueous solutions, offers a high theoretical volumetric (5855 mAh cm^{-3}) and gravimetric capacity (820 mAh g^{-1}).[50]

Cathode materials in AZIBs are categorized into four main types: Mn-based, V-based, PBA-based, and organic cathodes.[51] These materials operate through ion intercalation and chemical conversion reactions to store energy.[52] A distinctive advantage of AZIBs is the use of aqueous neutral or mildly acidic electrolytes (pH: 3.6~6.0), which provide non-flammability and high ionic conductivity (approximately 1 S cm^{-1}), using charge carriers like $ZnSO_4$, $Zn(CF_3SO_3)_2$, $ZnCl_2$, and $Zn(TFSI)_2$.[53]

However, AZIBs face challenges due to the limited thermodynamic stability window of water (~1.23 V), which restricts the operational potential window.[54] Exceeding this range triggers hydrogen evolution reaction (HER) and oxygen evolution reaction (OER), leading to electrolyte decomposition.[55] Additionally, water-induced side reactions can cause rapid capacity decline, marked by Zn dendrite growth, dissolution of cathode materials, and the formation of undesirable byproducts on cathodes, presenting hurdles that need to overcome to enhance the performance and longevity of AZIBs.[56]

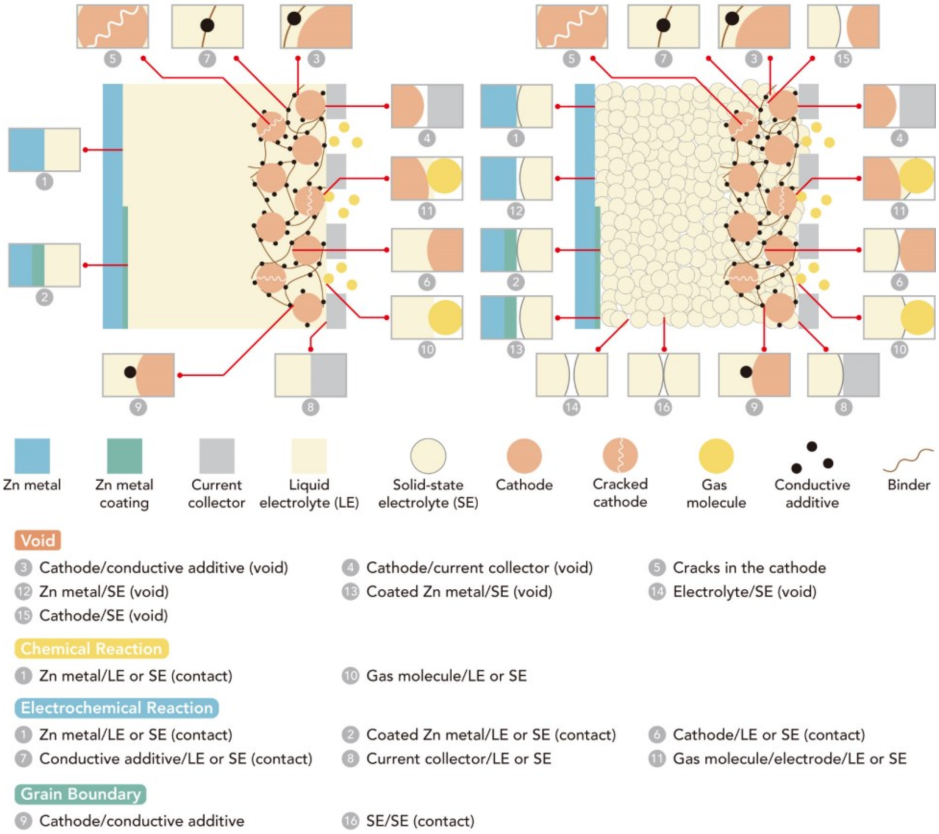

Figure 1.3 Scheme of composition of AZIBs and related interfaces and interphases.[23] Reused with permission from Wiley.

1.3.2 Application scenarios and potential markets of aqueous Zn-ion batteries

AZIBs are an advantageous solution for various energy storage needs due to their safety, cost-effectiveness, and environmental compatibility.[57] These batteries are exceptionally well-suited for stationary energy storage applications, such as grid storage where they store surplus power from renewable sources like solar and wind, contributing to grid stability and providing backup during peak demands.[52] Additionally, their rapid charge-discharge capability renders them ideal for frequency regulation in the energy grid, aiding in maintaining balance between electricity supply and demand, and thus ensuring grid reliability.[58] AZIBs also find applications in portable devices, including electric tools and medical equipment, where safety is paramount, making them a safer alternative to traditional LIBs.[59]

The potential markets for AZIBs are vast, including renewable energy integration, where they can help offset the intermittency of wind and solar energy, enhancing the viability of these green technologies.[33] Their safety and efficiency also make them suitable for emergency power supplies in critical settings like hospitals and data centers, as well as in electric mobility for lower-range vehicles such as electric bicycles and scooters, especially in cost-sensitive regions.[60] Moreover, as consumer electronics manufacturers increasingly seek environmentally friendly battery technologies, AZIBs may provide a lower-risk, sustainable option, especially as advancements in this technology continue to improve their energy density, power density and performance metrics.[61]

1.4 Modern main choice and fundamental challenges for AZIBs cathode

In AZIBs, the fundamental mechanism of energy storage, akin to LIBs, involves the shuttling of Zn^{2+} ions between the anode and cathode. Specifically, at the anode, Zn^{2+} undergoes electrochemical plating and stripping processes during charging and discharging.[62] The reactions at the cathode, however, vary based on the material composition; metal oxides (like MnO_2 and V_2O_5) may undergo intercalation or conversion reactions, whereas organic cathodes (such as polyaniline) participate in redox reactions.[63] AZIBs face significant challenges in real-world applications. Uneven electrodepositions can cause the formation of zinc dendrites and passivation layers, shortening battery life and posing safety risks due to potential short-circuiting. Additionally, side reactions can form inactive by-products layered double hydroxides (LDH) at the surface of anode, severely affecting the battery's CE.[64] Each Zn^{2+} in water is typically coordinated with six water molecules, resulting in strong electrostatic interactions that hinder ion diffusion and complicate the selection of suitable cathode materials.[65] Moreover, the standard potential for Zn^{2+} ion deposition is more negative compared to the hydrogen evolution reaction in aqueous solutions, challenging the stability of the electrolytes. The dissolution of active materials also degrades the battery's durability.[24]

1.4.1 Mn-based cathodes

Currently, Mn-based materials are extensively explored as cathodes for aqueous zinc-ion batteries (AZIBs) owing to their affordability and eco-friendly properties.[66] Manganese oxides are particularly noted for their varied crystal structures, morphologies at the nano and micro scale, and porosity, which are attributed to the different oxidation states of manganese, such as Mn^{2+}, Mn^{3+}, Mn^{4+}, and Mn^{7+}.[67] A wide range of Mn-based oxides, including α-MnO_2, β-MnO_2, γ-MnO_2, ε-MnO_2, δ-MnO_2, Mn_2O_3, and Mn_3O_4, have been extensively studied in recent years.[68] A significant challenge is the ongoing dissolution of manganese into the electrolyte. Liu et al. noted a marked decrease in the capacity of α-MnO_2 nanofibers within the first ten cycles; subsequent analysis using inductively coupled plasma (ICP) techniques revealed that Mn^{2+} present in the electrolyte could mitigate manganese dissolution from the cathode.[69] This observation led to the development of a pre-addition strategy, where 0.1 м Mn^{2+} was incorporated into the base electrolyte, enhancing electrode stability and enabling a capacity retention of 92% after 5000 cycles at a rate of 5 C.[69] Their findings highlighted the benefits of this Mn^{2+} additive in 1) buffering the active material dissolution; 2) boosting initial Coulombic efficiency and ionic conductivity; and 3) forming a cohesive, interconnected porous MnO_x layer post-charging, which significantly enhances the structural integrity and facilitates charge transfer across the electrode.

The effectiveness and underlying mechanisms of Mn^{2+} pre-addition in manganese oxide (MnO_2) cathodes remain subjects of debate. MnO_2 cathodes are particularly susceptible to Mn^{3+} Jahn–Teller distortions, and it has been traditionally argued that pre-adding Mn^{2+} can mitigate these effects by suppressing disproportionate reactions, thus reducing the dissolution of active materials. However, the stability of Mn^{2+} in aqueous electrolytes is questionable; it can redeposit on the MnO_2 cathode, contributing additional capacity through cycling. Studies by Xia et al. challenge the effectiveness of Mn^{2+} pre-addition in preventing dissolution of MnO_2.[70] They suggest that electro-oxidation of Mn^{2+} could lead to the formation of $ZnMn_2O_4$, inadvertently affecting capacity assessment due to changes in the MnO_2 phase and its dissolution. This hypothesis is primarily supported by phase transformations observed through *ex-situ* XRD analysis. To clarify these mechanisms, employing various *in-situ* characterization techniques, such as Raman spectroscopy, can provide more comprehensive insights into the dynamics of MnO_2 during charge and discharge cycles.

Regarding the energy storage mechanisms of Mn-based cathodes, the situation is complex, involving potential mechanisms such as Zn^{2+} intercalation/deintercalation, conversion reactions, and simultaneous H^+/Zn^{2+} co-insertion.[71] The prevailing model suggests a reversible intercalation/deintercalation of Zn^{2+}; however, Liu et al. reported that α-MnO_2 might react with H^+ to form MnOOH during discharge, subsequently interacting with $ZnSO_4$ and water to achieve charge balance.[69] Moreover, investigations have noted that Zn^{2+} intercalation can induce structural transformations in Mn-based cathodes. Further research is essential to understand these complex interactions fully and refine the designs of Mn-based cathodes for enhanced performance in AZIBs.

Additionally, the pre-intercalation strategy, also known as interstitial doping, has proven effective. This method involves incorporating polymers, anions, or water molecules into cathode materials. Xia and colleagues pioneered this approach with a polyaniline pre-intercalated layered MnO_2, achieving impressive stability of approximately 90% capacity retention over 200 cycles and a high specific capacity of 280 mAh g^{-1} at 200 mA g^{-1}.[72] Similarly, Zhi et al. developed a quasi-solid-state AZIBs using a $Na_{0.44}Mn_2O_4 \cdot H_2O$ electrode created by pre-intercalating Na^+ and water molecules into δ-MnO_2. This adjustment expanded the interlayer spacing from 0.55 to 0.72 nm, markedly boosting the cycling stability to 98% capacity retention after 10,000 cycles at 20C, a significant improvement over the baseline δ-MnO_2 electrode, which maintained 79.6% capacity retention after 2,000 cycles at 6.67C.[73] These advancements underscore the potential of interstitial doping to enhance the performance and stability of Mn-based cathodes in AZIBs.

1.4.2 Vanadium-based cathodes

V-based materials have garnered significant interest due to their abundant mineral reserves, cost-effectiveness, inherent stability, and chemical versatility.[74] The variability in valence states of vanadium allows these materials to maintain local electroneutrality, which helps mitigate the polarization of Zn^{2+} ions, enhancing the performance of AZIBs. Recent research has particularly focused on various vanadium oxides such as VO_2, V_2O_5, mixed-valence vanadates like $M_xV_2O_5 \cdot H_2O$, $H_2V_3O_8 \cdot nH_2O$, $M_xV_3O_8 \cdot nH_2O$, and $M_xV_6O_{16} \cdot nH_2O$, each offering unique benefits to battery technologies.[75] Despite their advantages, vanadium-based materials face challenges including toxicity, low operational voltages typically ranging from 0.2 to 1.6 V, and sluggish Zn^{2+} diffusion kinetics. To address these issues, various strategies such as the pre-intercalation technique, water-in-salt (WIS) electrolytes, defect engineering, and size regulation have been employed.[55]

A recognized approach to enhance the stability of AZIBs involves increasing the interlayer spacing of cathode materials. Dou et al. developed a high-performance cathode from a layered $H_2V_2O_3$ structure, suggesting that larger interlayer spacings could significantly improve electrochemical stability during Zn^{2+} ion insertion and extraction.[76] Additionally, introducing structural water, cations, and other modifiers into the host lattice to expand interlayer spacings has become a focus of recent research, aiming to stabilize the materials further. For instance, Yang and colleagues observed that intercalation of Zn^{2+} into $V_2O_5{\cdot}nH_2O$/graphene composites increased the interlayer spacing from 10.4 to 13.5 Å, contrary to earlier reports of lattice contraction.[77] They proposed a "lubricating" effect whereby the water-based shielding layer reduces the effective charge of Zn^{2+}, thus facilitating its diffusion. Furthermore, Nazar et al. demonstrated that intercalation of water molecules into $Zn_{0.25}V_2O_5{\cdot}H_2O$ before discharge, followed by their removal during Zn^{2+} insertion, uses the "pillar" effect of Zn^{2+} to stabilize the structure while allowing reversible expansion and contraction of the layered galleries, thereby enhancing both diffusion kinetics and overall battery performance.[78]

While materials like $Zn_{0.25}V_2O_5$, $Na_{0.33}V_2O_5$, and $Mg_{0.34}V_2O_5$ have been explored for their "lubricating" and "pillar" effects to enhance battery performance, the complexity of their crystal structures and the challenging evaluation of pre-intercalated ions' functions have restricted further advancements in these cathode materials. Another prominent approach to enhancing AZIBs involves optimizing electrolyte composition. Chen and colleagues discovered that using a 1M $ZnSO_4$ electrolyte led to the rapid dissolution of NaV_3O_8 (NVO) and the formation of vertical dendrites.[79] They improved the cycling stability by adding 1M Na_2SO_4 to the electrolyte, which helps mitigate NVO dissolution by altering its dissolution equilibrium and curbs the growth of Zn dendrites through the electrostatic shielding effect (as Na^+ has a lower reduction potential than

Zn^{2+}).

In another study, Liu et al. utilized a 3 M $Zn(CF_3SO_3)_2$ electrolyte in an aqueous Zn-V_2O_5 battery, achieving the highest specific capacity (470 mAh g^{-1} at 0.2 A g^{-1}) observed among V-based cathode materials, along with impressive durability (91.1% capacity retention over 4000 cycles at 5 A g^{-1}).[80] This WIS electrolyte expanded the electrochemical stability window, coupled with pseudocapacitive behavior, and enhanced mass diffusion, which in turn led to higher active material utilization. However, the high cost of $Zn(CF_3SO_3)_2$ (\$5.90 g^{-1}) compared to more conventional aqueous electrolytes like $ZnSO_4$ (\$0.25 g^{-1}) may limit its practical application for large-scale energy storage.

1.4.3 PBAs-based cathode

While Prussian blue analogues (PBA)-based cathodes might not excel in energy density or durability compared to Mn-based and V-based materials, they have garnered significant interest due to their exceptional power density, minimal cost, and straightforward synthesis routes.[51] PBAs, typically represented by the formula $A_xM_A[M_B(CN)_6]_z{\cdot}wH_2O$, involve alkali metals (A) and transition metals (M) and are noted for their open-framework structures that facilitate the insertion and extraction of various metal ions.[81] Research has increasingly focused on PBAs like ZnHCF, FeHCF, NiHCF, $FeFe(CN)_6$, and $Na_2MnFe(CN)_6$.[82-85] However, publications on ternary transition metal PBAs remain sparse. Introducing transition metals can increase the weight and reduce the specific capacity of PBAs, but using metal ions capable of undergoing multielectron redox reactions at both M_A and M_B sites could enhance specific capacity.

PBAs cathodes face challenges like dissolution and phase changes in aqueous electrolytes, leading to capacity losses and reduced durability. Electrolyte optimization is crucial for stabilizing PBAs structures. While adding excess Zn^{2+} can delay transformation and dissolution of ZnHCF, higher concentrations may expedite aging due to phase transformations, impacting stability. Additionally, surface modifications and coatings may help preserve PBA framework integrity, although more research is needed in this area.

1.5 Challenges for AZIBs Mn-based cathode industrialization

Mn-based cathode materials are emerging as a leading choice for industrial applications of AZIBs, primarily due to their cost-effectiveness and moderate operating voltages.[86] The abundance and low cost of manganese make these materials economically attractive for large-scale production.[87] Furthermore, Mn-based cathodes, such as various oxides of manganese, offer a median voltage range that is suitable for many applications, striking a good balance between energy density and stability.[88] These characteristics not only enhance the commercial viability of batteries but also align with industry requirements for sustainable and efficient energy storage solutions, positioning Mn-based cathodes closer to widespread industrialization.

1.5.1 The Trilemma of cathode performance

In the post-LIBs era, the advancement of multivalent-ion batteries is crucial due to their potential to surpass LIBs in terms of resource availability and cost.[89] Some key progress during the past 20 years is shown in Figure 1.4. However, the development of battery faces the "Trilemma" challenge in cathode research, where achieving high mass loading, high specific capacity, and high stability simultaneously proves difficult. This triangular challenge is a common barrier across various battery technologies, reflecting the intrinsic trade-offs in battery material properties.[90] Researchers are actively seeking innovative strategies to break through these constraints, aiming to optimize cathode materials to balance these competing factors effectively, thereby enhancing the overall performance and sustainability of battery systems.[25]

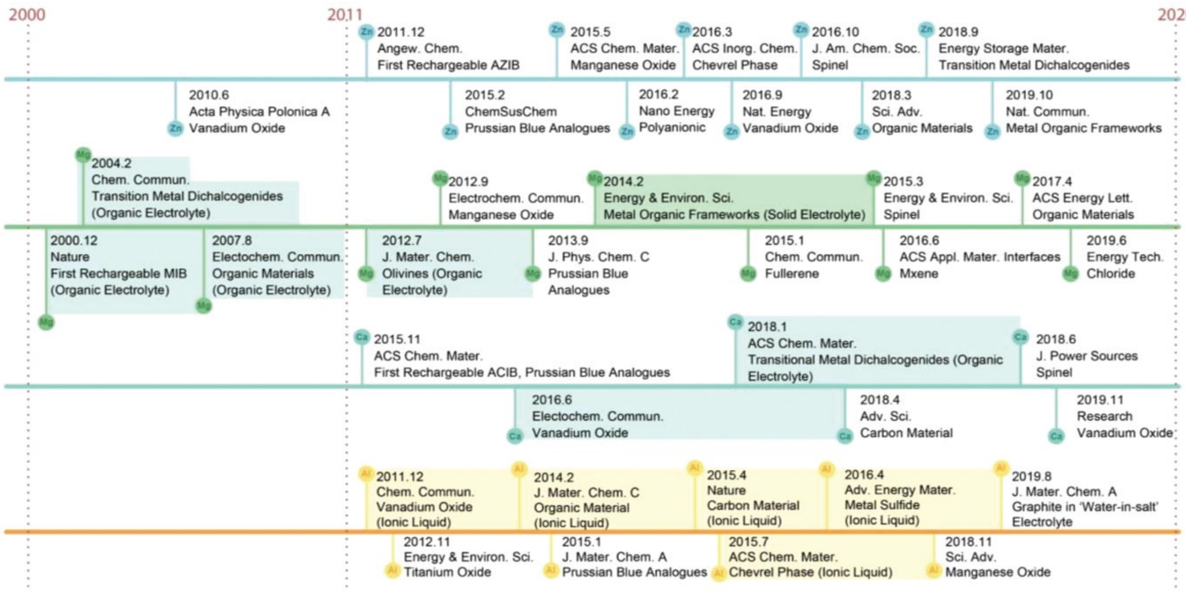

Figure 1.4 The main achievements of rechargeable multi-ion battery cathodes in the past 20 years.[75] Reused with permission from Wiley.

The "Trilemma" in battery cathode research—balancing high mass loading, high specific capacity, and high stability—arises from fundamental conflicts within the material and electrochemical properties of batteries. High mass loading entails a greater quantity of active material within the cathode, aiming to enhance energy density per unit area, but often results in thicker electrodes that impede efficient ion and electron transport. This increase in internal resistance can lead to reduced rate capability and exacerbate heat management issues, potentially compromising thermal stability and safety.[91] High specific capacities, meanwhile, are usually achieved through materials capable of undergoing multiple electron transfer reactions per formula unit. However, these materials can experience substantial volume changes during ion intercalation and deintercalation, leading to mechanical stresses that cause structural breakdown over time. Such volume expansions and contractions can severely impact the long-term electrochemical performance and stability of the battery.

Moreover, materials designed for enhanced stability tend to have robust structures that support lower specific capacities and are not conducive to high mass loadings.[92] The stability of a battery system also depends on maintaining stable interfaces between the electrode and electrolyte, which becomes more challenging as mass loading and specific capacity increase. Increased degradation products and interface resistance can arise from strained interactions at these interfaces under the stresses of higher capacities and faster charge-discharge cycles. Additionally, the role of electrolyte in managing efficient ion transport across these more complex electrode structures becomes critical, yet more difficult with thicker and denser electrodes. Addressing these challenges often requires trade-offs between the amount of active material and the ability of the electrolyte to sustain adequate ion transport paths, underlining the systemic nature of the Trilemma" that complicates scaling from laboratory prototypes to full-scale production.

1.5.2 Scalable production challenges

Although many industrialization challenges are similar for various cathode material systems, this thesis focuses on Mn-based cathodes. The scalable production of Mn-based cathodes for AZIBs faces several significant challenges that stem from material properties, manufacturing processes, and market demand dynamics. One of the primary hurdles is maintaining the consistency and quality of manganese oxide materials during large-scale synthesis.[93] Manganese oxides are preferred in AZIBs due to their favorable electrochemical properties, such as high theoretical capacity and environmentally benign nature.[94] However, these materials are sensitive to synthesis conditions, including temperature, pH, and precursor concentrations, which can vary widely in large-scale production settings. Ensuring uniformity in the physicochemical properties of Mn-based cathodes—such as particle size, morphology, and crystallinity—is crucial, as these factors directly influence the electrochemical performance and stability of the batteries. Scaling up from laboratory-scale synthesizes to industrial production requires tightly controlled processes to avoid significant batch-to-batch variations that can lead to performance inconsistencies in the final product.

Similar to LIBs manufacturing, in the processes of missing for cathode material, a solvent of N-methyl-2-pyrrolidone (NMP) is typically used to create a homogeneous slurry of active materials, conductive agents, and binders.[95] However, the inherent electrical conductivity of manganese oxide is lower than that of materials like lithium iron phosphate (LFP), necessitating a higher proportion of conductive additives such as carbon black and carbon nanotubes to enhance the electrode conductivity. This adjustment, however, complicates the mixing process considerably. The increased content of conductive agents, which often feature very low tap densities, presents substantial technical challenges. The low tap density of these carbon materials means they are less compact and can lead to issues in achieving uniform slurry consistency, which is crucial for the even coating of the cathode material on substrates. Handling and dispersing a larger volume of these fluffy materials evenly throughout the manganese oxide matrix while ensuring consistent viscosity and preventing sedimentation of the heavier manganese oxide particles demands highly precise and controlled mixing techniques. Addressing this challenge is essential for ensuring the quality and performance of Mn-based AZIBs, marking it as a priority for researchers and manufacturers working towards the commercial viability of these battery systems.

Furthermore, the integration of high mass loading in Mn-based cathodes while maintaining high specific capacity and stability poses a complex challenge in scalable manufacturing.[96] High mass loading is desirable because it increases the energy density of the battery, making the technology more competitive with existing battery systems like lithium-ion batteries.[97] However, as previously discussed, increasing mass loading often leads to thicker electrodes that suffer from slower ion diffusion rates, increased internal resistance, and potential structural instabilities during charge-discharge cycles. These issues are exacerbated at the scale of mass production, where even minor inconsistencies in electrode coating thickness or material composition can lead to significant performance degradation.[98] Developing advanced electrode manufacturing techniques, such as using doctor blade or slot-die coating processes that ensure uniform and precise electrode coatings, is essential for overcoming these challenges.[99] Additionally, the industry needs to innovate in areas like binder and conductive additive formulations to enhance electrode integrity and conductivity without compromising the active material's loading levels.[100]

The economic scalability of Mn-based AZIBs is closely tied to the optimization of the entire battery system's cost-effectiveness. While manganese is abundant and cheaper than materials like cobalt or nickel, the overall cost efficiency of Mn-based AZIBs depends not only on the cathode material but also on the associated electrolyte, separator, and cell assembly processes.[101] The selection of compatible, cost-effective electrolytes that can enhance the long-term stability of Mn-based cathodes is crucial, especially considering the sensitivity of manganese oxides to dissolution in certain aqueous electrolyte solutions. Moreover, market forces demand continuous improvements in battery performance, which in turn requires ongoing R&D investment. Addressing these economic and technical challenges requires a multi-faceted approach involving material innovation, advanced manufacturing technologies, and rigorous quality control mechanisms to ensure that scaling up production does not compromise the performance, safety, and cost parameters critical to the commercial success of Mn-based AZIBs.

1.6 References

[1] A. Das, A. Ghosh, *Environment, Development and Sustainability*, (2023) 1-37.

[2] P. Pal, *A Basic Overview of Environment and Sustainable Development*, **2** (2023) 408.

[3] I. Hadjipaschalis, A. Poullikkas, V. Efthimiou, *Renew. Sustain. Energy Rev.*, **13** (2009) 1513-1522.

[4] A. Blakers, M. Stocks, B. Lu, C. Cheng, R. Stocks, *IEEE Journal of Photovoltaics*, **9** (2019) 1828-1833.

[5] N.T. Narayanan, A. Kumar, P. Thakur, R. Sharma, A. Puthirath, A. Pulickel, (2021).

[6] L. Wang, S. Yan, C.D. Quilty, J. Kuang, M.R. Dunkin, S.N. Ehrlich, L. Ma, K.J. Takeuchi, E.S. Takeuchi, A.C. Marschilok, *Adv. Mater. Interfaces*, **8** (2021) 2002080.

[7] D. Qin, J. Ding, C. Liang, Q. Liu, L. Feng, Y. Luo, G. Hu, J. Luo, X. Liu, *Acta Phys. Chim. Sin.*, **40** (2024) 2310034.

[8] J. Peng, J. Meng, J. Wu, Z. Deng, M. Lin, S. Mao, D.-I. Stroe, *J. Energy Storage*, **71** (2023) 108197.

[9] X. Sun, J. Gao, C. Wang, X. Gao, J. Liu, N. Gao, H. Li, Y. Wang, K. Yu, *J. Chem. Eng.*, **383** (2020) 123198.

[10] H. Yu, S. Wang, Y. Hu, G. He, I.P. Parkin, H. Jiang, *Green Energy Environ.*, **7** (2022) 266-274.

[11] H. Li, W. Zhang, K. Sun, J. Guo, K. Yuan, J. Fu, T. Zhang, X. Zhang, H. Long, Z. Zhang, *Adv. Energy Mater.*, **11** (2021) 2100867.

[12] X. Yin, Y. Li, W. Cai, C. Fan, W. Liu, N. Wang, G. Qin, Z. Xie, X. Chen, Y. Han, *Appl. Surf. Sci.*, **624** (2023) 157124.

[13] S.S. Shah, F. Niaz, M.A. Ehsan, H.T. Das, M. Younas, A.S. Khan, H.U. Rahman, S.A. Nayem, M. Oyama, M.A. Aziz, *J. Energy Storage*, **79** (2024) 110152.

[14] Z. Shang, S. Wang, H. Zhang, W. Zhang, S. Lu, K. Lu, *Nanoscale*, **14** (2022) 14433-14454.

[15] Z. Ye, Z. Cao, M.O.L. Chee, P. Dong, P.M. Ajayan, J. Shen, M. Ye, *Energy Stor. Mater.*, **32** (2020) 290-305.

[16] R. Nagraj, R. Puttaswamy, P. Yadav, H.K. Beere, S.N. Upadhyay, N. Sanna Kotrappanavar, S. Pakhira, D. Ghosh, *ACS Appl. Mater. Interfaces*, **14** (2022) 56886-56899.

[17] H. Dong, X. Hu, R. Liu, M. Ouyang, H. He, T. Wang, X. Gao, Y. Dai, W. Zhang, Y. Liu, *Angew. Chem., Int. Ed.*, **135** (2023) e202311268.

[18] J. Chu, Z. Liu, J. Yu, L. Cheng, H.G. Wang, F. Cui, G. Zhu, *Angew. Chem., Int. Ed.*, **136** (2024) e202314411.

[19] B. Luo, Y. Wang, L. Sun, S. Zheng, G. Duan, Z. Bao, Z. Ye, J. Huang, *J. Energy Chem.*, **77** (2023) 632-641.

[20] S. Zheng, W. Zhao, J. Chen, X. Zhao, Z. Pan, X. Yang, *Nanomicro Lett.*, **15** (2023) 46.

[21] M. Chen, S. Xie, X. Zhao, W. Zhou, Y. Li, J. Zhang, Z. Chen, D. Chao, *Energy Stor. Mater.*, **51** (2022) 683-718.

[22] M. Wu, G. Zhang, H. Yang, X. Liu, M. Dubois, M.A. Gauthier, S. Sun, *InfoMat*, **4** (2022) e12265.

[23] Y. Liu, X. Lu, F. Lai, T. Liu, P.R. Shearing, I.P. Parkin, G. He, D.J. Brett, *Joule*, **5** (2021) 2845-2903.

[24] M.E. Pam, D. Yan, J. Yu, D. Fang, L. Guo, X.L. Li, T.C. Li, X. Lu, L.K. Ang, R. Amal, *Adv. Sci.*, **8** (2021) 2002722.

[25] W. Shi, W.S.V. Lee, J. Xue, *ChemSusChem*, **14** (2021) 1634-1658.

[26] S. Lee, J. Hwang, W.J. Song, S. Park, *Batteries Supercaps*, **5** (2022) e202200237.

[27] C. Li, S. Jin, L.A. Archer, L.F. Nazar, *Joule*, **6** (2022) 1733-1738.

[28] P. Agreement, in: report of the conference of the parties to the United Nations framework convention on climate change (21st session, 2015: Paris). Retrived December, HeinOnline, 2015, pp. 2.

[29] X. Gao, H. Wu, C. Su, C. Lu, Y. Dai, S. Zhao, X. Hu, F. Zhao, W. Zhang, I.P. Parkin, *Energy Environ. Sci.*, **16** (2023) 1364-1383.

[30] M. Huang, X. Wang, X. Liu, L. Mai, *Adv. Mater.*, **34** (2022) 2105611.

[31] H. Zhang, L. Qiao, H. Kühnle, E. Figgemeier, M. Armand, G.G. Eshetu, *Energy Environ. Sci.*, **16** (2023) 11-52.

[32] P. Canepa, G. Sai Gautam, D.C. Hannah, R. Malik, M. Liu, K.G. Gallagher, K.A. Persson, G. Ceder, *Chem. Rev.*, **117** (2017) 4287-4341.

[33] Y. Liang, H. Dong, D. Aurbach, Y. Yao, *Nature Energy*, **5** (2020) 646-656.

[34] A. Ponrouch, J. Bitenc, R. Dominko, N. Lindahl, P. Johansson, M.R. Palacín, *Energy Stor. Mater.*, **20** (2019) 253-262.

[35] X. Tang, D. Zhou, B. Zhang, S. Wang, P. Li, H. Liu, X. Guo, P. Jaumaux, X. Gao, Y. Fu, *Nat. Commun.*, **12** (2021) 2857.

[36] M. Liu, Z. Rong, R. Malik, P. Canepa, A. Jain, G. Ceder, K.A. Persson, *Energy Environ. Sci.*, **8** (2015) 964-974.

[37] S. Chen, D. Zhao, L. Chen, G. Liu, Y. Ding, Y. Cao, Z. Chen, *Small Structures*, **2** (2021) 2100082.

[38] M. Lowe, S. Tokuoka, T. Trigg, G. Gereffi, *The US Value Chain, Contributing CGGC researcher: Ansam Abayechi*, (2010).

[39] S. He, Z. Mo, C. Shuai, W. Liu, R. Yue, G. Liu, H. Pei, Y. Chen, N. Liu, R. Guo, *Appl. Surf. Sci.*, **577** (2022) 151904.

[40] S. Jin, J. Yin, X. Gao, A. Sharma, P. Chen, S. Hong, Q. Zhao, J. Zheng, Y. Deng, Y.L. Joo, *Nat. Commun.*, **13** (2022) 2283.

[41] X. Li, F. Ning, L. Luo, J. Wu, Y. Xiang, X. Wu, L. Xiong, X. Peng, *RSC Adv.*, **12** (2022) 8394-8403.

[42] Y. Lv, Y. Xiao, L. Ma, C. Zhi, S. Chen, *Adv. Mater.*, **34** (2022) 2106409.

[43] H. Li, Z. Chen, L. Zheng, J. Wang, H. Adenusi, S. Passerini, H. Zhang, *Small Methods*, (2023) 2300554.

[44] K. Zhu, T. Wu, S. Sun, W. van den Bergh, M. Stefik, K. Huang, *Energy Stor. Mater.*, **29** (2020) 60-70.

[45] G.P. Rajarathnam, T.K. Ellis, A.P. Adams, B. Soltani, R. Zhou, P.J. Cullen, A.M. Vassallo, *J. Electrochem. Soc.*, **168** (2021) 070522.

[46] Q.Y. Zhao, G.Y. Yin, Y.F. Liu, R.R. Tang, X.W. Wu, X.X. Zeng, *Carbon Neutralization*, **2** (2023) 90-114.

[47] N. Zhang, Y.-R. Ji, J.-C. Wang, P.-F. Wang, Y.-R. Zhu, T.-F. Yi, *J. Energy Chem.*, **82** (2023) 423-463.

[48] W. Zhang, Y. Dai, R. Chen, Z. Xu, J. Li, W. Zong, H. Li, Z. Li, Z. Zhang, J. Zhu, *Angew. Chem., Int. Ed.*, **62** (2023) e202212695.

[49] B. Zhao, P. Jia, L. Yu, Y. Song, Z. Li, Y. Wang, R. Feng, H. Li, X. Cui, H. Cui, *J. Energy Storage*, **73** (2023) 109174.

[50] Y. Zhao, S. Guo, M. Chen, B. Lu, X. Zhang, S. Liang, J. Zhou, *Nat. Commun.*, **14** (2023) 7080.

[51] J. Liu, Z. Shen, C.-Z. Lu, *J. Mater. Chem. A*, (2024).

[52] L.E. Blanc, D. Kundu, L.F. Nazar, *Joule*, **4** (2020) 771-799.

[53] J. Hao, X. Li, X. Zeng, D. Li, J. Mao, Z. Guo, *Energy Environ. Sci.*, **13** (2020) 3917-3949.

[54] A. Bayaguud, X. Luo, Y. Fu, C. Zhu, *ACS Energy Lett.*, **5** (2020) 3012-3020.

[55] L. Suo, O. Borodin, T. Gao, M. Olguin, J. Ho, X. Fan, C. Luo, C. Wang, K. Xu, *Science*, **350** (2015) 938-943.

[56] Z. Liu, A. Prowald, O. Höfft, G. Li, A. Lahiri, F. Endres, *ChemElectroChem*, **5** (2018) 2321-2325.

[57] C.F. Bischoff, O.S. Fitz, J. Burns, M. Bauer, H. Gentischer, K.P. Birke, H.-M. Henning, D. Biro, *J. Electrochem. Soc.*, **167** (2020) 020545.

[58] H. Dong, J. Li, S. Zhao, Y. Jiao, J. Chen, Y. Tan, D.J. Brett, G. He, I.P. Parkin, *ACS Appl. Mater. Interfaces*, **13** (2020) 745-754.

[59] J. Li, K. McColl, X. Lu, S. Sathasivam, H. Dong, L. Kang, Z. Li, S. Zhao, A.G. Kafizas, R. Wang, *Adv. Energy Mater.*, **10** (2020) 2000058.

[60] J. Shi, K. Xia, L. Liu, C. Liu, Q. Zhang, L. Li, X. Zhou, J. Liang, Z. Tao, *Electrochim. Acta*, **358** (2020) 136937.

[61] T. Zhang, Y. Tang, S. Guo, X. Cao, A. Pan, G. Fang, J. Zhou, S. Liang, *Energy Environ. Sci.*, **13** (2020) 4625-4665.

[62] Y. Zhang, S. Deng, Y. Li, B. Liu, G. Pan, Q. Liu, X. Wang, X. Xia, J. Tu, *Energy Stor. Mater.*, **29** (2020) 52-59.

[63] I. Khan, N. Baig, S. Ali, M. Usman, S.A. Khan, K. Saeed, *Energy Stor. Mater.*, **35** (2021) 443-469.

[64] M. Li, Z. Li, X. Wang, J. Meng, X. Liu, B. Wu, C. Han, L. Mai, *Energy Environ. Sci.*, **14** (2021) 3796-3839.

[65] H. Liu, J. Li, X. Zhang, X. Liu, Y. Yan, F. Chen, G. Zhang, H. Duan, *Adv. Funct. Mater.*, **31** (2021) 2106550.

[66] H. Chen, C. Dai, F. Xiao, Q. Yang, S. Cai, M. Xu, H.J. Fan, S.J. Bao, *Adv. Mater.*, **34** (2022) 2109092.

[67] Y. Chen, S. Gu, S. Wu, X. Ma, I. Hussain, Z. Sun, Z. Lu, K. Zhang, *J. Chem. Eng.*, **450** (2022) 137923.

[68] S. Gao, B. Li, H. Tan, F. Xia, O. Dahunsi, W. Xu, Y. Liu, R. Wang, Y. Cheng, *Adv. Mater.*, **34** (2022) 2201510.

[69] H. Pan, Y. Shao, P. Yan, Y. Cheng, K.S. Han, Z. Nie, C. Wang, J. Yang, X. Li, P. Bhattacharya, *Nature Energy*, **1** (2016) 1-7.

[70] C. Qiu, X. Zhu, L. Xue, M. Ni, Y. Zhao, B. Liu, H. Xia, *Electrochim. Acta*, **351** (2020) 136445.

[71] Y. Xu, G. Zhang, X. Wang, X. Li, J. Zhang, X. Wu, Y. Yuan, Y. Xi, X. Yang, M. Li, *Journal of Colloid and Interface Science*, (2024).

[72] J. Huang, Z. Wang, M. Hou, X. Dong, Y. Liu, Y. Wang, Y. Xia, *Nat. Commun.*, **9** (2018) 2906.

[73] D. Wang, L. Wang, G. Liang, H. Li, Z. Liu, Z. Tang, J. Liang, C. Zhi, *ACS Nano*, **13** (2019) 10643-10652.

[74] X. Chen, H. Zhang, J.-H. Liu, Y. Gao, X. Cao, C. Zhan, Y. Wang, S. Wang, S.-L. Chou, S.-X. Dou, *Energy Stor. Mater.*, **50** (2022) 21-46.

[75] Y. Liu, G. He, H. Jiang, I.P. Parkin, P.R. Shearing, D.J. Brett, *Adv. Funct. Mater.*, **31** (2021) 2010445.

[76] H. Luo, B. Wang, F. Wang, J. Yang, F. Wu, Y. Ning, Y. Zhou, D. Wang, H. Liu, S. Dou, *ACS Nano*, **14** (2020) 7328-7337.

[77] M. Yan, P. He, Y. Chen, S. Wang, Q. Wei, K. Zhao, X. Xu, Q. An, Y. Shuang, Y. Shao, *Adv. Mater.*, **30** (2018) 1703725.

[78] D. Kundu, B.D. Adams, V. Duffort, S.H. Vajargah, L.F. Nazar, *Nature Energy*, **1** (2016) 1-8.

[79] F. Wan, L. Zhang, X. Dai, X. Wang, Z. Niu, J. Chen, *Nat. Commun.*, **9** (2018) 1656.

[80] N. Zhang, F. Cheng, J. Liu, L. Wang, X. Long, X. Liu, F. Li, J. Chen, *Nat. Commun.*, **8** (2017) 1-9.

[81] G. Zampardi, F. La Mantia, *Current Opinion in Electrochemistry*, **21** (2020) 84-92.

[82] L. Zhang, L. Chen, X. Zhou, Z. Liu, *Adv. Energy Mater.*, **5** (2015).

[83] Z. Liu, P. Bertram, F. Endres, *Journal of Solid State Electrochemistry*, **21** (2017) 2021-2027.

[84] K. Lu, B. Song, J. Zhang, H. Ma, *J. Power Sources*, **321** (2016) 257-263.

[85] Z. Liu, G. Pulletikurthi, F. Endres, *ACS Appl. Mater. Interfaces*, **8** (2016) 12158-12164.

[86] N. Liu, B. Li, Z. He, L. Dai, H. Wang, L. Wang, *J. Energy Chem.*, **59** (2021) 134-159.

[87] Y. Guo, Y. Zhang, H. Lu, *Battery Energy*, **1** (2022) 20210014.

[88] A. Zhou, R. Chi, Y. Shi, X. Zhao, X. Li, Z. Kou, Z. Zhang, X. Zhang, G. Nie, *Materials Today Chemistry*, **27** (2023) 101294.

[89] H.J. Lee, J. Shin, J.W. Choi, *Adv. Mater.*, **30** (2018) 1705851.

[90] X. Gao, C. Zhang, Y. Dai, S. Zhao, X. Hu, F. Zhao, W. Zhang, R. Chen, W. Zong, Z. Du, *Small Structures*, **4** (2023) 2200316.

[91] H. Liu, N. Wang, L. Hu, M. Sun, Z. Li, C. Jia, *Electrochim. Acta*, **441** (2023) 141856.

[92] Y. Jiao, L. Kang, J. Berry-Gair, K. McColl, J. Li, H. Dong, H. Jiang, R. Wang, F. Corà, D.J. Brett, *J. Mater. Chem. A*, **8** (2020) 22075-22082.

[93] Y. Zhao, Y. Zhu, X. Zhang, *InfoMat*, **2** (2020) 237-260.

[94] T. Xiong, Y. Zhang, W.S.V. Lee, J. Xue, *Adv. Energy Mater.*, **10** (2020) 2001769.

[95] H. Liu, X. Cheng, Y. Chong, H. Yuan, J.-Q. Huang, Q. Zhang, *Particuology*, **57** (2021) 56-71.

[96] X. Gao, C. Shen, H. Dong, Y. Dai, P. Jiang, I.P. Parkin, H. Zhang, C.J. Carmalt, G. He, *Energy Environ. Sci.*, **17** (2024) 2287-2297.

[97] W. Zhang, S. Liang, G. Fang, Y. Yang, J. Zhou, *Nanomicro Lett.*, **11** (2019) 1-12.

[98] S. Deng, B. Xu, X. Liu, C.-W. Kan, T. Chen, *J. Chem. Eng.*, **475** (2023) 146098.

[99] L. Ma, X. Wang, J. Sun, *Journal of Electroanalytical Chemistry*, **873** (2020) 114395.

[100] K. Fang, F. Li, G.-G. Wang, Y.-L. Liu, M.-L. Tan, D.-Q. Zhao, H.-Y. Zhang, J.-C. Han, *Journal of Materials Science & Technology*, **143** (2023) 84-92.

[101] W. Zheng, Z. Cui, C. Liu, L. Yuan, S. Li, L. Lin, T. Meng, L. Yang, Y. Tong, D. Shu, *Chem. Sci.*, **15** (2024) 20303-20314.

Chapter 2 Characterization techniques

2.1 Overview

Before conducting further electrochemical characterizations, the intrinsic properties of materials were analyzed. This analysis includes *in-situ* and *ex-situ* structural characterizations of AZIBs at various charged states to explore energy storage mechanisms. In this chapter, a concise overview of characterization techniques is provided, divided into two main categories: structural and electrochemical characterizations, focusing on the standards and equipment used for testing.

2.2 Structural characterizations

2.2.1 X-ray powder diffraction (XRD)

X-ray diffraction (XRD) patterns, which measure crystal structures, were utilized to examine the structures of electrodes, particularly cathode materials. The crystal structure changes were explored via XRD (Rigaku miniFlex600) with Cu-Kalpha radiation (λ = 0.70 nm) in the 2θ range of 5° to 40°, and Mo-Kalpha radiation (λ = 0.15 nm) from 5° to 70°. Using Bragg's law (Equation 2.1), the spacing (d) between diffraction planes can be calculated, where θ represents the incident angle, n is an integer, and λ is the wavelength of the beam.

$$n \cdot \lambda = 2d \cdot sin\theta \tag{2.1}$$

2.2.2 X-ray photoelectron spectroscopy (XPS)

XPS, performed using a Thermo Scientific K-alpha photoelectron spectrometer, serves to analyze the surface topography (2-10 nm depth) and assess the elemental composition of the surface. The technique operates based on the photoelectric effect, where XPS spectra are generated by measuring the kinetic energy and the number of electrons emitted from the top 0 to 20 nm of the material when exposed to X-ray radiation. *Ex-situ* XPS spectra were utilized to track the changes in the valence states of metal ions within the cathode material throughout battery cycling. Additionally, a preprocessing step was applied to the data to calibrate it using carbon, which has a known binding energy of 284.8 eV.

2.2.3 Thermal gravimetric analysis (TGA)

TGA was performed on a PerkinElmer TGA 4000 System at a controlled heating rate of 3 $°C \cdot min^{-1}$ in air, monitoring mass changes in the material as the temperature varied. This technique is particularly useful for evaluating the crystal water content in cathodes and determining the decomposition temperatures of polymer electrolytes. The mass of each active material was accurately measured with an analytical balance (Ohaus; δ = 0.01 mg).

2.2.4 Scanning electron microscopy (SEM)

The morphologies of the samples were analyzed using a field emission scanning electron microscope (FE-SEM, FEI Verios G4 UC) that included an energy dispersive X-ray spectroscopy (EDS) attachment. Prior to the SEM analysis, the samples were coated with platinum to enhance imaging quality.

2.2.5 Transmission electron microscopy (TEM)

For transmission electron microscopy (TEM) using a JEOL JEM2100F, the procedure involved dispersing the samples in acetone to create a uniform solution. This solution was then carefully applied to a holey carbon grid, which serves as a support for high-resolution imaging. This preparation method ensures optimal sample stability and clarity during the TEM imaging process.

2.2.6 X-ray micro-computed tomography (X-CT)

The X-ray micro-Computed Tomography (X-CT, ZEISS Xradia 620 Versa with 40x lens) projections were reconstructed using a filtered-back projection algorithm (XMReconstructor, Carl Zeiss Inc.). The reconstructed X-CT datasets were imported into Avizo 2020.2 (ThermoFisher) for further segmentation and quantification. A median filter was applied to increase the signal to noise ratio.

2.2.7 Scanning transmission electron microscopy (STEM)

The detailed morphologies of the samples were analyzed using scanning transmission electron microscope (STEM), a JEOL ARM300CF, beamline E02 of Diamond Light Source (UK).

2.3 Electrochemical characterizations

2.3.1 Cyclic voltammetry (CV)

Cyclic Voltammetry (CV), conducted using the VMP3 Biologic electrochemical workstation, is employed to analyze the redox reactions and reversibility of the battery.

The three studies presented are all manganese-based cathodes with an electrochemical window (EW) of 0.8-1.9 V. Too high or too low potential will cause OER or HER, thus limiting the cycle life of AZIBs. This technique utilizes the Nernst equation, which links cyclic voltammograms to Gibbs free energy.[1] In equation 2.3, E represents the potential, F is the Faraday constant, n denotes the number of electrons transferred, and 0 indicates standard conditions. This relationship allows for predictions and interpretations of electrochemical behaviors under various conditions.

$$E^0 = E^0_{reduction} - E^0_{oxidation} \tag{2.2}$$

$$\Delta G^0 = -nFE^0 \tag{2.3}$$

During a voltage sweep, changes in Gibbs energy can be inferred from thermodynamics, where Q represents the ratio of concentrations between the oxidized and reduced forms. This approach allows for the analysis of energy shifts as a function of the chemical equilibrium within the system.

$$\Delta G = \Delta G^0 \ + RT\,ln\,Q \tag{2.4}$$

Hence,

$$-nFE = -nFE^0 \ + RT\,ln\,Q \tag{2.5}$$

$$E = E^0 - \frac{RT}{nF} ln(\frac{C_r}{C_o}) = E^0 - \frac{0.0592V}{n} ln(\frac{C_r}{C_o}) \tag{2.6}$$

Regarding the voltammogram, the distinct peaks observed signify various redox reactions occurring within the batteries. For a typical Zn//MnO_2 battery, the peaks at approximately 1.65 V, 1.35 V, and 1.25 V correspond to the oxidation of Mn^{2+}, the intercalation of Zn^{2+}, and the intercalation of H^+ respectively.[2] These peaks provide insights into the electrochemical processes and the dynamic interactions of ions in the battery.

2.3.2 Electrochemical impedance spectroscopy (EIS)

Electrochemical Impedance Spectroscopy (EIS) measurements were performed using a Gamry 1010E instrument to determine the equivalent series resistance (ESR) and ionic conductivity of batteries. A sinusoidal potential E_t was applied, creating a phase-shifted current signal φ, and the impedance Z was obtained through Ohm's law, with ω denoting the angular frequency. The resulting data are typically presented as Nyquist plots, which exhibit semicircular arcs described by Euler's equation. In constructing the equivalent circuit, five primary components—resistor, capacitor, inductor, Warburg element, and constant phase element (CPE)—are included to account for diffusion processes and the behavior of non-ideal capacitors.

$$E_t = E_0 \sin \omega t \tag{2.7}$$

$$I_t = I_0 \sin(\omega t + \varphi) \tag{2.8}$$

$$Z = \frac{E_t}{I_t} = Z_0 \frac{\sin \omega t}{\sin(\omega t + \varphi)} = Z_0(\cos \varphi + j \sin \varphi) \tag{2.9}$$

Understanding the physical and chemical properties of a battery system is important for determining the appropriate Electrochemical Impedance Spectroscopy (EIS) model. Zheng et al. suggested a widely accepted typical equivalent circuit model, which considers the physical structure of the battery.[3] This model segments the equivalent circuit into three primary components: combined internal resistance (R_s) and charge transfer resistance (R_{ct}), collectively referred to as the equivalent series resistance (ESR), as depicted in Figure 2.1. At high frequencies, the internal resistance is determined by the first x-intercept, while the charge transfer resistance, along with diffusion effects, is typically evident at medium to low frequencies, noted at the second x-intercept.

R_s: Combined internal resistance encompasses the interfacial contact resistance between the material and current collectors, the electrolyte's ohmic resistance, and the intrinsic resistance of the current collectors.

R_{ct}: Interfacial charge-transfer resistance, indicating the resistance of electrochemical reactions at the electrode surface.

W_0: Warburg element, describing electron and ion transport within the pores of the electrode materials.

CPE: Constant phase element.

C_{lsf}: Element accounts for the low-frequency surface capacitance.

R_{leak}: Low-frequency leakage resistance.

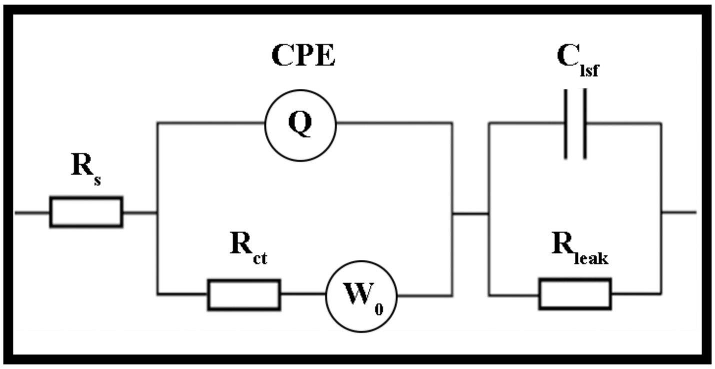

Figure 2.1 The equivalent circuit for EIS fitting.

2.3.3 Gravimetric charge-discharge test (GCD)

Gravimetric charge-discharge tests were performed using a NEWARE battery testing system at an EW of 0.8-1.9 V. This study investigates the rate capabilities of galvanostatic charge-discharge (GCD) tests under various current densities—0.1, 0.2, 0.5, 1, 2, 5, and 10 A g^{-1}—following the portico testing protocol. The achieved specific capacity is closer to the cathode's theoretical value under lower current density, whereas cycling stability is typically assessed at higher current densities (1, 2, and 5 A g^{-1}) to gauge performance under more demanding conditions. To confirm scalability, pouch cells were assembled and tested galvanostatically at 0.1 and 0.2 A g^{-1}.

2.4 References

[1] A.-S. Feiner, A. McEvoy, *J. Chem. Educ.*, **71** (1994) 493.

[2] Q. Chen, X. Lou, Y. Yuan, K. You, C. Li, C. Jiang, Y. Zeng, S. Zhou, J. Zhang, G. Hou, *Adv. Mater.*, **35** (2023) 2306294.

[3] P.L. Moss, G. Au, E.J. Plichta, J.P. Zheng, *J. Electrochem. Soc.*, **155** (2008) A986.

Chapter 3 Three-dimensional carbon networks supporting free-standing, high-loading Mn-based cathodes for high-performance aqueous Zn-ion batteries

3.1 Introduction

Aqueous batteries with neutral or mildly acidic electrolytes have showcased significant potential for future energy storage technologies due to their affordability, high safety, and eco-friendliness.[1] Among these, AZIBs stand out due to their abundant resource availability and a volumetric energy density of 5,855 mAh cm^{-3}, surpassing that of LIBs at 2,061 mAh cm^{-3}.[2] The development of suitable cathode materials for AZIBs is critical due to the strong electrostatic interactions between Zn^{2+} and the host material structures.[3] Various cathodes, including manganese-based, vanadium-based, and PBAs, have been explored.[4] Mn oxides, in particular, offer promising industrial prospects due to their lower cost compared to PBAs and vanadium oxides.[5]

Mn-based AZIBs are emerging as strong candidates, favored for their abundant and safe raw materials, along with an operational voltage of 1.5 V vs. Zn/Zn^{2+}.[6] These batteries feature diverse atomic structures like α-, β-, γ-, λ-, and δ-MnO_2, each contributing uniquely to Zn^{2+} diffusion and storage.[7] Despite their advantages, structures such as the tunnel-like and layered δ-MnO_2 are prone to structural collapse during discharge and significant volume changes during cycling, respectively, which impede long-term stability.[8] Pre-intercalation of cations such as H^+, Li^+, Na^+, K^+, Zn^{2+}, and Cu^{2+} has been shown to enhance stability and support sustainable Zn^{2+} storage in these systems, pointing towards viable improvements in AZIBs technology.[8-12]

Enhancing the rate performance of Mn-based cathodes, hampered by their low electrical conductivity (10^{-5} to 10^{-6} S cm^{-1}) and slow mass diffusion rates, is crucial for their application in fast-charging next-generation devices.[13] Methods like creating oxygen vacancies or applying surface carbon coatings have been proposed to enhance both ionic and electronic transfers within these cathodes.[14] However, these approaches typically require high-temperature processes like sintering, which are not ideal for large-scale industrial production due to their high energy demands and increased safety risks.[9] Alternative materials, such as CNTs, graphene, and nitrogen-doped carbon, offer superior electrical conductivity and surface areas, facilitating better electron transport and reducing the aggregation of active materials.[15] Despite the development of hybrid materials like MnO_2/CNTs and MnO_2/graphene, many cathodes are still made using traditional slurry coating methods.[16] During production, the use of poly(vinylidene fluoride) (PVDF) often impedes Zn^{2+} transport at the interface between the current collector and active material due to its polymer structure, which binds Zn^{2+} more tightly than Li^+, causing significant polarization and limited mobility.[17] This results in diminished rate capacity, reduced cycling stability, and lower energy density.[18] Therefore, the development of binder-free electrodes is critical to circumvent these issues of slow Zn^{2+} transport and underutilized active material mass.[19]

More importantly, the first step in realizing the industrialization of AZIBs cathodes is to find ways to achieve high mass loading, as discussed before. In this study, the challenges were addressed by introducing an innovative cathode design: a Na-intercalated manganese oxide (NMO) integrated with a three-dimensional CNTs network, creating a binder-free, free-standing, high-loading cathode structure known as NMO with varying thinness carbon nanotubes (NMO/VTCNTs), which requires no heat-treatment. This cathode employs a novel network architecture utilizing two types of carbon nanotubes with varying diameters, a design innovation that optimizes both the capacity and the mass loading. Specifically, low-diameter carbon nanotubes (LTCNTs, with a diameter range of 5-10 nm) and high-diameter carbon nanotubes (HTCNTs, with a diameter range of 110-150 nm) were used. These varied diameters help enhance the electrode's specific capacity, ensure a flat electrode surface, and improve the overall cathode mass loading. The robust network of interlinked CNTs, structured in a three-dimensional format, provides substantial resilience against mechanical stresses and aids in forming a cohesive interface with the NMO. This network facilitates additional Zn^{2+} storage capacities, smooth channels for the electrolyte to penetrate, and effective pathways for the migration of Zn^{2+} and electrons. Embedded within this network, the $Na_{0.55}Mn_2O_4\cdot1.5H_2O$ compound was uniformly dispersed and secured within the CNTs framework, which notably boosted the structure's overall stability and enhances the rates of ion and electron transport. The cathodes that have been developed are not only free-standing and binder-free but also achieve an electrode loading of approximately 5 mg cm^{-2}. They maintain superior electrochemical performance over extended use, demonstrating impressive specific capacities: 329 mAh g^{-1} after 120 cycles at a current density of 0.2 A g^{-1}, 225 mAh g^{-1} after 200 cycles at 1 A g^{-1}, and 158 mAh g^{-1} after 1000 cycles at 2 A g^{-1}. The fabrication process also ensures adequate interfacing between the LTCNTs and the NMO while allowing the HTCNTs to boost the loading of active materials, thereby preserving electrode uniformity and contributing to the robust, free-standing nature of these cathodes. This distinctive approach in using carbon nanotube networks of differing diameters marks a significant step forward in achieving high mass loading and capacity, offering a vital blueprint for future industrial applications.

3.2 Experimental section

3.2.1 Chemicals

All chemicals were used as purchased without further purification. Poly(vinylidene fluoride), average Mw ~534,000, powder (Sigma-Aldrich); 1-methyl-2-pyrrolidinone, 99% (Sigma-Aldrich); $Mn(NO_3)_2$, 99% (Sigma-Aldrich); NaOH, reagent grade, 97%, powder (Sigma-Aldrich); H_2O_2, 30 % (w/w) in H_2O (Sigma-Aldrich); $MnSO_4\cdot1H_2O$ (≥99%) (Sigma-Aldrich); $ZnSO_4\cdot7H_2O$ (≥99%) (Sigma-Aldrich).

3.2.2 Synthesis of NMO/LTCNTs hybrid nanomaterials

NMO/LTCNTs was synthesized via a simple co-precipitation method, as illustrated in Figure 3.1. All chemicals (Sigma-Aldrich) were used without further purification. First, 7.5 mmol of manganese(II) nitrate tetrahydrate was dissolved in 10 mL of deionized water to form solution **A**, while 27.5 mmol of NaOH was dissolved in 10 mL of deionized water to form solution **B**. Next, 5 mmol LTCNTs (with diameters of about 5–10 nm) was dispersed in 10 mL of deionized water to create solution **C**, and solution **D** consisted of 6 mL of 30 wt% H_2O_2 in 45 mL of deionized water. After sonicating solution **C** for 20 minutes and stirring solutions **A** and **B** for 10 minutes, solutions **B** and **C** were quickly combined with solution **A** and stirred for another 5 minutes. Then, solution **D** was rapidly poured into this mixture under vigorous magnetic stirring for an additional 10 minutes, immediately producing a black precipitate. The mixture was placed in an ice bath for 48 hours to form solution **E**. Following sufficient aging, solution **E** was centrifuged at 4500r min^{-1} for 10 minutes, and the resulting brown-black powder was freeze-dried for 48h, yielding the NMO/LTCNTs hybrid nanomaterial. For comparison, NMO was prepared through the same procedure but without the addition of CNTs.

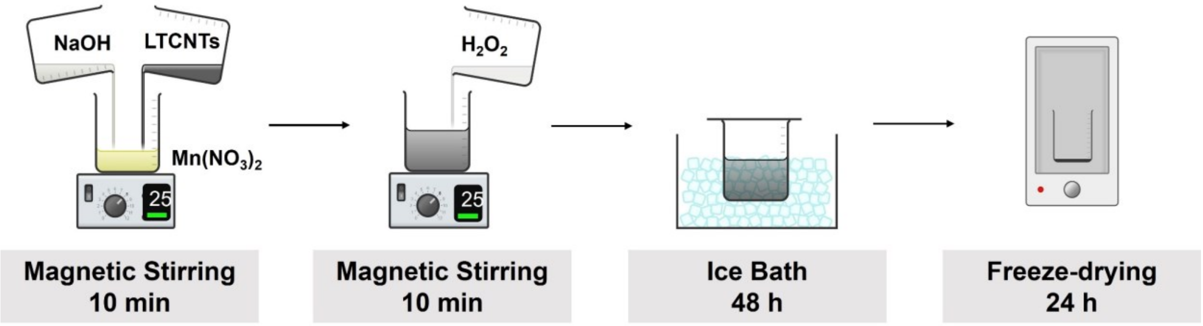

Figure 3.1 Schematic diagram of the synthesis method of NMO/LTCNTs.

3.2.3 Fabrication of free-standing, binder-free NMO/VTCNTs cathodes

The procedure for fabricating free-standing, binder-free cathodes is shown in Figure 3.2. The obtained NMO/LTCNTs were ground for 10 min and then mixed with HTCNTs in water in a ratio of 7:3 by mass and subjected to full sonication in an ultrasonic processor (UP400S, Scientific & Medical Products Ltd.) with a pause time of 0.5 s in the amplitude of 70% for 10 min. The final product was attached to the Polyethersulfone Membrane by suction filtration. After allowing it to dry naturally at room temperature, the electrode was peeled off to become a free-standing, binder-free cathode and achieved ≈ 5 mg cm^{-2} of the active materials.

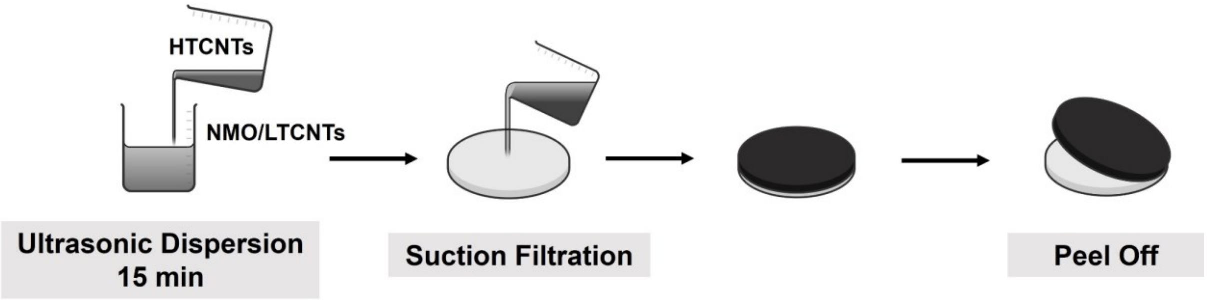

Figure 3.2 Schematic diagram of the preparation of free-standing binder-free NMO/VTCNTs cathodes.

3.2.4 Materials characterization

The alteration in the crystal structure due to the intercalation was methodically examined using X-ray diffraction (XRD) techniques, employing a Rigaku miniFlex600 system. For this analysis, two different radiations were utilized: Mo-Kα radiation with a wavelength of 0.70 nm, measured over a range of 5° to 40° in 2θ, and Cu-Kα radiation with a wavelength of 0.15 nm, spanning a range of 5° to 70° in 2θ. This comprehensive range allowed for a detailed characterization of the changes in the crystal lattice induced by the ion intercalation. To assess the external morphologies of the sample post-intercalation, a field emission scanning electron microscope (FE-SEM, FEI, Verios G4 UC) equipped with an energy-dispersive X-ray spectroscopy (EDS) attachment was utilized. Prior to SEM analysis, the samples underwent a platinum coating process to enhance the electron conductivity and image clarity. Additionally, the internal structural details were captured using a transmission electron microscope (TEM, JEOL, JEM2100F). For TEM imaging, the samples were first dispersed in acetone and then carefully placed onto a holey carbon grid, which provided an optimal background for high-resolution imaging. Further chemical composition and oxidation states at various voltages were investigated through X-ray photoelectron spectroscopy (XPS), utilizing a K-Alpha+ system from Thermo Fisher Scientific Messtechnik. This technique was critical in understanding the electronic environment of the materials following the ion intercalation. For in-depth internal structural analysis, micro-computed tomography (micro-CT) was performed using a ZEISS Xradia 620 Versa with a 40x lens. The imaging projections were reconstructed using a filtered-back projection algorithm (XMReconstructor, Carl Zeiss Inc.). Following reconstruction, the micro-CT datasets were transferred into Avizo 2020.2 (ThermoFisher) for advanced segmentation and quantification. To enhance the clarity and contrast of the images, a median filter was applied, effectively reducing noise without compromising the detail. The segmented micro-CT images delineated the pristine material into three distinct phases: active materials (NMO), carbon nanotubes, and pores, providing a clear visualization of the material's internal structure and phase distribution.

3.2.5 Electrochemical measurement

For the preparation of non-free-standing, non-binder-free cathode materials, a slurry composition was created by homogeneously mixing sodium intercalated manganese oxide (NMO) as the active material, carbon black (Super P, TIMCAL Graphite & Carbon) for conductivity, and PVDF (M.W. 534000, Sigma-Aldrich) as the binder. The components were blended in a weight ratio of 7:2:1 using N-methyl-2-pyrrolidone (NMP) as the solvent to ensure proper adhesion and dispersion. This mixture was then uniformly coated onto carbon paper substrates to form the cathode layer. After the coating process, the cathodes were subjected to a drying phase in a vacuum oven maintained at 60 °C for 24 hours to remove any residual solvent, ensuring the integrity and mechanical stability of the cathode films. This process yielded cathode sheets with an active material loading density ranging from approximately 0.45 to 1.5 mg cm^{-2}, optimized for electrochemical performance. The cathodes were then utilized to assemble CR2032 coin cells, a standard format in battery testing, in a controlled open-air environment. This assembly involved using glass-fiber separators (Whatman, GF/A) and metallic zinc foils as anodes, along with a specific electrolyte mixture of 2 M $ZnSO_4$ and 0.2 M $MnSO_4$ to facilitate ion transport. Electrochemical testing of these coin cells was conducted to evaluate their performance parameters. The testing regimen included using NEWARE test systems, maintained at a constant temperature of 25 °C, where the current density and specific capacity were determined based exclusively on the mass of the active materials. Additionally, CV tests were performed using a ZIVE SP1 potentiostat analyzer (WonA Tech, Korea) at various scan rates ranging from 0.8 to 1.9 V versus Zn^{2+}/Zn, to study the redox characteristics and kinetics of the electrode materials. Furthermore, EIS was executed using the same ZIVE SP1 impedance analyzer to investigate the internal resistance and charge transfer processes across the electrode/electrolyte interface, across a broad frequency range from 10^5 to 10^{-1} Hz.

3.3 Computation methods

First-principles calculations were rigorously conducted by Dr. Chengyi Zhang using the Vienna Ab-initio Simulation Package (VASP). For these simulations, a high cut-off energy of 550 eV was meticulously selected to ensure accurate wave function representation, while the Γ-centered k-mesh was meticulously configured as 3×3×3 for all calculations to optimize the balance between computational efficiency and accuracy. Full cell optimization was employed to comprehensively alleviate any stress within the atomic structure, thus ensuring the stability and realism of the modeled systems. Convergence criteria for these calculations were stringently set to maintain high precision: maximum force allowed was 0.01 eV/Å, the stress limit was established at 0.03 GPa, and displacement tolerance was finely tuned to 0.001 Å. These parameters were crucial for achieving reliable and repeatable results in the computational experiments. Additionally, the choice of the Perdew-Burke-Ernzerhof (PBE) formulation of the generalized gradient approximation (GGA) and the employment of ultrasoft pseudopotentials for each atom were adopted to enhance the accuracy of the electronic interactions modeled within the system.[20, 21]

The study extended to examining the crystalline structures derived both from databases of known crystal forms and experimental outcomes. This approach was fundamental in constructing accurate models for theoretical investigations. Specifically, to elucidate the dynamics of Zn^{2+} migration within the anode during intercalation processes, the migration barriers were calculated for Zn^{2+} transference both in the bulk structure of NMO and at the interface of NMO and CNTs. Advanced computational techniques such as the Linear Synchronous Transit (LST) and Quadratic Synchronous Transit (QST) methods were utilized to effectively search for the transition states (TS) in these systems.[22, 23] Moreover, the Nudged Elastic Band (NEB) method was applied to confirm these TS structures, where parameters such as cut-off energy, self-consistent field (SCF) convergence, maximum force, stress, and displacement were meticulously set to values of 550 eV, 2.0×10^{-5} eV/atom, 0.02 eV/Å, 0.1 GPa, and 0.002 Å, respectively, to ensure comprehensive and precise analysis.[24]

Additionally, charge density differences were quantitatively calculated as per Equation (3.1), further enhancing our understanding of electronic structure changes during ion migration and interaction scenarios.

$$\Delta\rho = \rho_{total} - \rho_{adsorbent} - \rho_{adsorbate} \tag{3.1}$$

Where ρ is the charge density of the corresponding structure.

3.4 Results and discussion

3.4.1 Material characterizations

The structural morphology of the synthesized sodium manganese oxide/low thinness carbon nanotubes (NMO/LTCNTs) composite was extensively characterized using both SEM and TEM techniques. SEM analysis, as depicted in Figure 3.3a, confirmed the integration of LTCNTs into the sheet-like structure of NMO, resulting in a uniform hybrid morphology. The SEM images revealed that the sheet-like NMO particles range in diameter from 80 to 300 nm, demonstrating a broad but controlled size distribution which is critical for consistent electrochemical performance. Further detailed examination by TEM, illustrated in Figure 3.3b, showcased the sheet-like overlapping morphology of NMO with LTCNTs, which are approximately 5 nm in diameter, interspersed throughout. This arrangement highlights the effective intercalation of nanotubes within the NMO sheets, facilitating enhanced electrical connectivity and ion transport pathways. Additionally, Figure 3.3c provides a closer look at the LTCNTs, which maintain a uniform diameter of about 5 nm and are intricately intercalated between the layers of sheet-like NMO structures. This configuration is crucial for optimizing the interface interactions between the active material and the conductive network, enhancing the electrochemical reactivity and stability of the composite.

Further insights into the elemental composition and distribution within the composite were obtained through energy-dispersive X-ray spectroscopy (EDS) mapping, represented in Figure 3.3d. This analysis technique was employed to visualize the spatial distribution of elements within the NMO/LTCNTs composite. Subsequent Figures 3.3e-h, detail the individual distributions of manganese (Mn), oxygen (O), sodium (Na), and carbon (C) elements. These images reveal a homogenous dispersion of sodium ions throughout the structure, indicating effective doping within the host matrix. Additionally, the carbon nanotubes were also uniformly distributed, confirming their role in providing a robust conductive framework that enhances the overall electronic conductivity and structural integrity of the material.

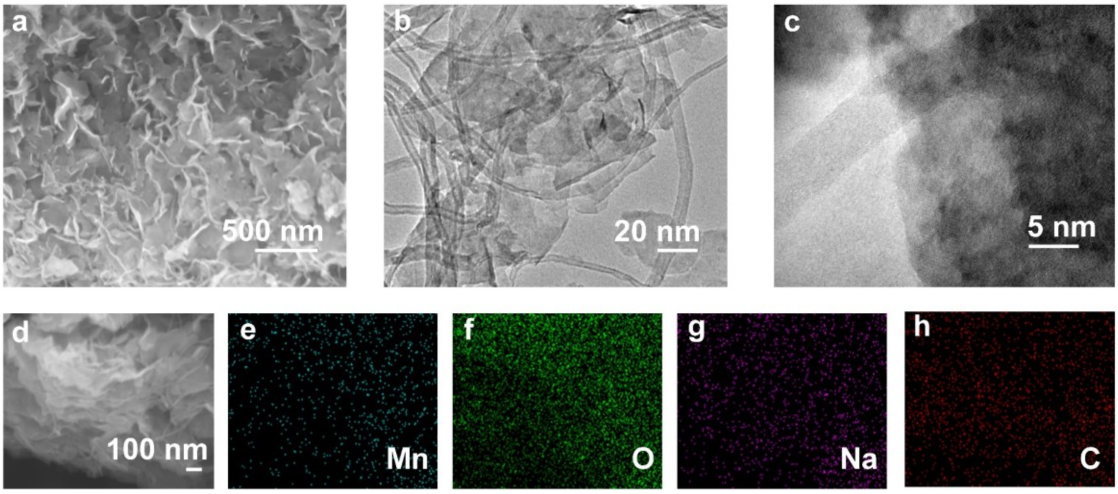

Figure 3.3 (a) SEM and (b)TEM of NMO/LTCNTs. (d) Higher-resolution TEM of NMO/LTCNTs clearly shows LTCNTs intercalated in the interlayer of sheet-like NMOs. (e-f) EDS mapping images of NMO/LTCNTs shows that NMO and LTCNTs are uniformly distributed.

The integration of HTCNTs within these cathodes provides essential mechanical support, minimizing cathode shrinkage during the drying process. For electrochemical evaluations, the NMO/VTCNTs were precisely cut into small discs measuring 1.2 cm in diameter, covering an area of approximately 1.13 cm^2. The digital image in Figure 3.4a showcases the NMO/VTCNTs electrode post-filtration, highlighting its remarkably flat and even surface which enhances the interface's reaction efficiency and electrical conductivity with the electrolyte. Additionally, the inset of Figure 3.4a reveals the cathodes' flexibility, demonstrating its ability to bend without damage. X- CT provided a visual of the macroscopic 3D morphology of the NMO/VTCNTs electrode, depicted in Figure 3.4b. This imaging technique revealed a three-dimensional arrangement of sheet-like NMO structures supported by a carbon nanotube network, enhancing the electrode's structural integrity. Using threshold segmentation based on grey scale levels, the active material (NMO) and pore phases were differentiated, allowing visualization of the cathode's complex three-dimensional structure and a wide distribution of pore sizes. The uniform distribution of CNTs within the network not only reinforces the mechanical stability of the active material but also establishes the NMO/VTCNTs as a robust free-standing cathode.

XRD analysis, displayed in Figure 3.4c, compares the patterns of the NMO/VTCNTs and pure NMO. The presence of CNTs increases the X-ray scattering, which slightly diminishes peak intensities, yet it's crucial to note that this does not alter the peak positions.[25, 26] The diffraction pattern aligns closely with that of Birnessite $Na_{0.55}Mn_2O_4 \cdot 1.5H_2O$ (JCPDS no. 43-1456), characterized by lattice parameters a = 5.175(3) Å, b = 2.849(1) Å, c = 7.338(5) Å, and unit cell volume V = 105.3(6) Å^3, with $\alpha = \gamma = 90°$ and $\beta = 103.19(4)°$, underscoring the structural fidelity of the hybrid NMO/CNTs material in maintaining its crystalline integrity.[27]

XPS was employed to meticulously assess the atomic ratio and average oxidation state (AOS) of each element present on the surface of the material. Notably, the substantial presence of oxygen (O) can be attributed to oxygen absorption at the surface. In the XPS spectra, sodium (Na) is clearly identified, as evidenced by a distinct peak at 1071 eV in Figure 3.4f (Na 1s). The Mn 2p spectrum (Figure 3.4g) exhibits two distinct peaks, indicative of a binding energy difference of 11.7 eV. Conversely, the Mn 3s spectrum (Figure 3.4h) presents a smaller binding energy difference of 4.90 eV. Utilizing this latter value, the AOS for Mn was meticulously calculated using the relationship AOS = 8.956 – 1.126ΔEs.[27] This calculation places the valence state of Mn at approximately 3.44, closely aligning with the estimations derived from the overall elemental analysis. The spectrum of O 1s as depicted in Figure 3.4i was analyzed and deconvoluted into three prominent peaks.[28] These peaks correspond to different oxygen-related species: adsorbed water, represented by H–O–H at 532.5 eV; surface-adsorbed oxygen ions, denoted as Mn–OH at 531.2 eV; and the lattice oxygen species, indicated as Mn–O–Mn at 529.6 eV.[29] Initial tests on wettability, as depicted in Figures 3.5a-b, showed that the porous CNTs network significantly boosts the cathode's compatibility with aqueous 2M $ZnSO_4$ electrolyte compared to those coated on carbon paper.

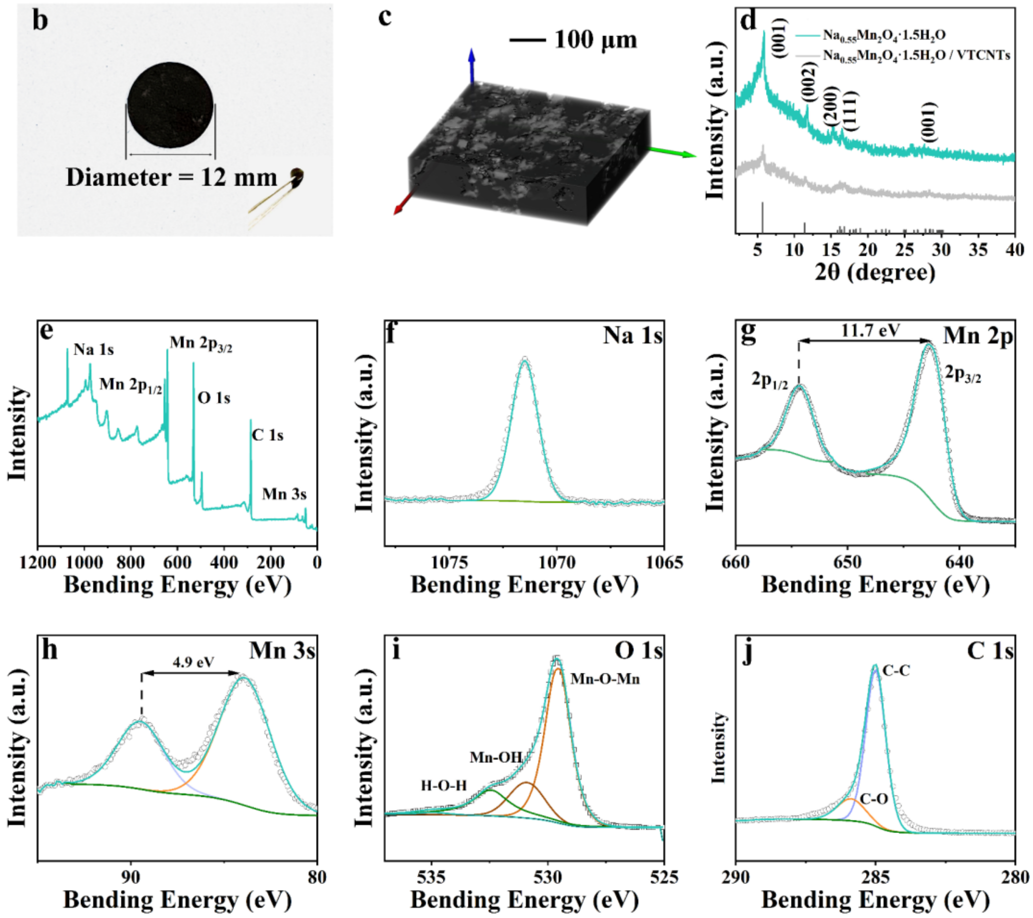

Figure 3.4 (a) Optical photo of free-standing, binder-free NMO/VTCNTs cathodes, with insets showing that the cathode is flexible and bendable. (b) The X-CT image of NMO/VTCNTs cathode shows a uniform distribution of active material in the electrode and the supporting role of carbon nanotubes. (c) XRD patterns of NMO/VTCNTs and NMO. (d) XPS pattern of NMO/VTCNTs with a focus on (e) Na 1s, (f) Mn 2p, (g) Mn 3s, (h) O 1s, and (i) C 1s.

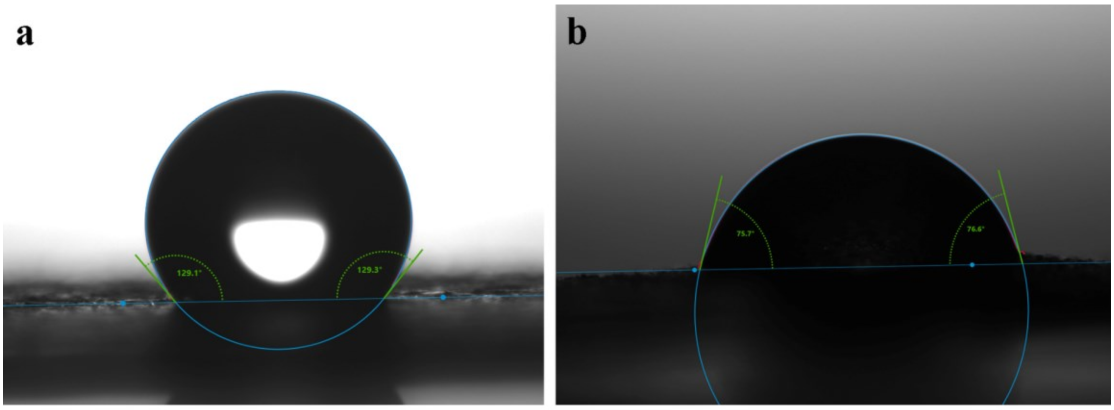

NMO on carbon paper

Free-standing binder-free NMO/VTCNTs

Figure 3.5 Contact angle tests of (a) the cathode of NMO on carbon paper and (b) free-standing binder-free NMO/VTCNTs cathode for 2 M $ZnSO_4$ electrolyte.

3.4.2 Electrochemical characterizations

CR2032-type coin cells were constructed to evaluate the electrochemical performances of NMO in the presence and absence CNTs, with metallic zinc serving as the anode—a common configuration in AZIBs research.[30] Different electrolyte concentrations (i.e., $ZnSO_4$ concentrations) were firstly compared, and it was found that the cycling performance of the $ZnSO_4$ electrolyte of 2 M performed well in the tests of both NMO and NMO/VTCNTs cathode materials, as shown in Table 3.1.

Table 3.1 Specific capacity of NMO and NMO/VTCNTs at 0.2 A g^{-1} under different electrolyte ($ZnSO_4$) concentrations.

Concentration	NMO	NMO/VTCNTs
1 M	270 mAh g^{-1} (Initial)	294 mAh g^{-1} (Initial)
	187 mAh g^{-1} (100th cycle)	257 mAh g^{-1} (100th cycle)
1.5 M	275 mAh g^{-1} (Initial)	286 mAh g^{-1} (Initial)
	190 mAh g^{-1} (100th cycle)	273 mAh g^{-1} (100th cycle)
2 M	290 mAh g^{-1} (Initial)	310 mAh g^{-1} (Initial)
	201 mAh g^{-1} (100th cycle)	305 mAh g^{-1} (100th cycle)
2.5 M	288 mAh g^{-1} (Initial)	301 mAh g^{-1} (Initial)
	169 mAh g^{-1} (100th cycle)	298 mAh g^{-1} (100th cycle)

3 M	265 mAh g^{-1} (Initial) 156 mAh g^{-1} (100th cycle)	307 mAh g^{-1} (Initial) 277 mAh g^{-1} (100th cycle)

As a benchmark, pure NMO was synthesized and used as control material. The CV analysis of the NMO/LTCNTs and pure NMO cathodes—both prepared using the same method involving binders and carbon paper collectors—was conducted at varying scan rates ranging from 0.1 to 1 mV s^{-1} within the potential window of 0.8 to 1.9 V to explore the influence of LTCNTs on the electrochemical behavior of NMO (as illustrated in Figures 3.6a and d). At lower scan rates, dual pairs of redox peaks were noted: the reduction peaks appeared at 1.32 and 1.18 V, while the oxidation peaks were observed at 1.57 and 1.62 V. The CV profile of the NMO/LTCNTs cathode showed redox peak positions similar to those of the pure NMO cathode, underscoring a comparable charge storage mechanism in both. This is indicative of typical redox reactions seen in manganese oxide-based cathodes within an aqueous $ZnSO_4$ electrolyte environment during cycling.[31] Notably, as depicted in Figure 3.6d, the dual redox peaks of the NMO cathode without CNTs began merging into a single pair starting at a scan rate of 0.3 mV s^{-1}, and by the time the scan rate increased to 1 mV s^{-1}, the two oxidation peaks combined and shifted to a higher voltage of 1.66 V—a net shift of approximately 0.2 V from the lowest scan rate of 0.1 mV s^{-1}. In contrast, the CV curves of the NMO/LTCNTs cathodes remained consistent across different scan rates, indicating similar reaction behaviors and kinetics under both high and low scan rates.[32] Interestingly, with increasing scan rates, the peak heights in the redox reactions of the NMO/LTCNTs cathodes were noticeably larger compared to those of the pure NMO cathodes, reflecting superior conductivity and electrochemical activity under higher scan rate conditions.[33] Typically, the potential difference $\Delta\varphi$ between the oxidation and reduction peaks in quasi-reversible electrochemical reactions tends to increase with the scan rate. However, in a well-reversible system, this trend is mitigated. In Figure 3.6d, as the scan rate escalated, the shifts in peaks P2 and P4 were measured at 0.059 and 0.048 V, respectively. Conversely, the shifts in peaks P1, P2, P3, and P4 in the NMO/LTCNTs configuration in Figure 3.6a were more restrained at only 0.026, 0.021, 0.030, and 0.025 V, respectively, highlighting the more reversible nature of the electrochemical system in the NMO/LTCNTs cathode.

To delve deeper into the kinetic properties of various cathode materials, their diffusion-controlled and capacitive behaviors were analyzed by examining the four peaks depicted in Figure 3a and the two peaks in Figure 3d. The relationship between peak current (i) and sweep rate (v) is expected to adhere to the equation shown below as Equation (3.2):

$$i = a\nu^{b} \tag{3.2}$$

hence, $\log(i) = \log(a) + b\cdot\log(\nu)$

This relationship is encapsulated in Equation (3.2), where the coefficients a and b are derived from this fitting. The coefficient b is particularly informative; a value close to 1 indicates that the electrochemical reaction is predominantly capacitive, while a value near 0.5 suggests that diffusion processes are more influential.[34] As illustrated in Figures 3b and e, for the NMO/LTCNTs cathodes, the calculated values of b—0.750, 0.780, 0.805, and 0.856—indicate a strong capacitive influence dominating the kinetics of these self-supporting cathodes. Conversely, the NMO cathode exhibited b values of 0.608 and 0.701, pointing towards a reaction kinetics that leans more towards being diffusion-controlled. The inclusion of CNTs in the cathode structure notably enhances its capacitive contribution, aligning with findings reported in previous studies. Additionally, the relationship between normalized capacity and sweep rate (v) was plotted, as seen in Figures 3c and f. As the scan rates increased, the normalized capacity of the NMO cathodes displayed a more pronounced decrease compared to that of the NMO/LTCNTs. This observation underscores the superior high-rate performance of the NMO/LTCNTs cathodes, demonstrating their enhanced ability to maintain capacity at elevated scan rates.

Ex-situ XRD analysis was employed to explore the energy storage mechanism of NMO/LTCNTs cathodes at specific voltages, as depicted in Figure 3.6i. The structural changes of the NMO/LTCNTs were monitored through XRD measurements taken at various states of charge and discharge, ranging from 0.8 to 1.9 V under a current density of 2 A g^{-1}. According to the XRD patterns displayed in Figure 3.6g, the charge and discharge cycles do not induce significant phase changes in the material. However, a noticeable 1° shift in the characteristic (002) peak occurs during charging, which gradually diminishes in prominence during the discharge phase. This change is attributed to the intercalation and deintercalation of Zn^{2+}, which diminish the intensity of these peaks throughout the cycling process. Similar to other AZIBs, the compound $Zn_4SO_4(OH)_6{\cdot}xH_2O$ (ZHS) forms on the cathode during the discharge phase. Notably, as revealed in Figure 3.6h, the peaks indicative of ZHS deposition vanish during the subsequent charging cycle, demonstrating the reversible nature of cation intercalation within this system. Specifically, during discharge, the cathode receives a flow of current along with H^+ and Zn^{2+}, adhering to the dual-ion intercalation mechanism characteristic of aqueous AZIBs, and resulting in ZHS formation on the cathode surface.[35] Upon charging, as H^+ and Zn^{2+} are extracted from the cathode, the ZHS compound dissipates. This reversible formation and decomposition of ZHS are critical for understanding the electrochemical behavior of the cathodes and are represented in Equation (3.3).

$$12OH^- + 2SO_4^{2-} + 8Zn^{2+} + 10H_2O \rightleftharpoons 2Zn_4(OH)_6SO_4 \cdot 5H_2O \tag{3.3}$$

Figure 3.6h illustrates the discharge process, transitioning from 1.9 V down to 0.8 V, during which there is a noticeable increase in the accumulation of ZHS on the cathode. This observation aligns with findings reported in other studies.[36] As characteristic of MnO_2-based cathodes, the NMO/VTCNTs cathode also exhibits proton intercalation, which is evident from the O 1s spectra in the *ex-situ* XPS analysis, as depicted in Figure 3.7b.

Alongside the formation of ZHS, there is a notable intensification of the Mn-OH peak during the initial cycle. This enhancement correlates with the proton intercalation and deintercalation processes in MnO_2-based cathodes, which are integral to the cathode's operation and are detailed in Equation (3.4). This interaction signifies the active involvement of hydrogen ions in the electrochemical reactions occurring within the cathode during the discharge cycle.

$$MnO_2 + H^+ + e^- \rightleftharpoons MnOOH \tag{3.4}$$

As cycling continues, the poor reversibility of ZHS leads to its accumulation on the cathode surface, which becomes increasingly apparent after extensive cycling—specifically after 50 cycles at a current density of 0.2 A g^{-1}. This accumulation is evident from the enhanced H-O-H peak signal observed in the XPS spectra shown in Figure

3.7a. This phenomenon underscores the ongoing accumulation of ZHS, which progressively covers the surface of the cathode material. Interestingly, throughout both the initial and prolonged cycling, the intensity of the Mn-O-Mn peak remains consistently higher in the charged state compared to the discharged state. This observation indicates the occurrence of reversible proton intercalation and deintercalation within each cycle, a critical aspect of the cathode's functionality. This reversible behavior is further corroborated by the Mn 2p spectra in *ex-situ* XPS, presented in Figure 3.7b, although the distinction in Mn signal intensity diminishes over time due to the long-term accumulation of ZHS. The accumulated ZHS typically forms a sheet-like structure that coats the cathode surface, as depicted in Figure S4a. However, this coverage by ZHS also impedes the detection of manganese, as the element's signal becomes increasingly obscured, showing minimal surface distribution in the spectral analysis shown in Figure 3.8. This effect highlights the impact of ZHS coverage on the visibility and analysis of underlying cathode materials in advanced electrochemical studies.

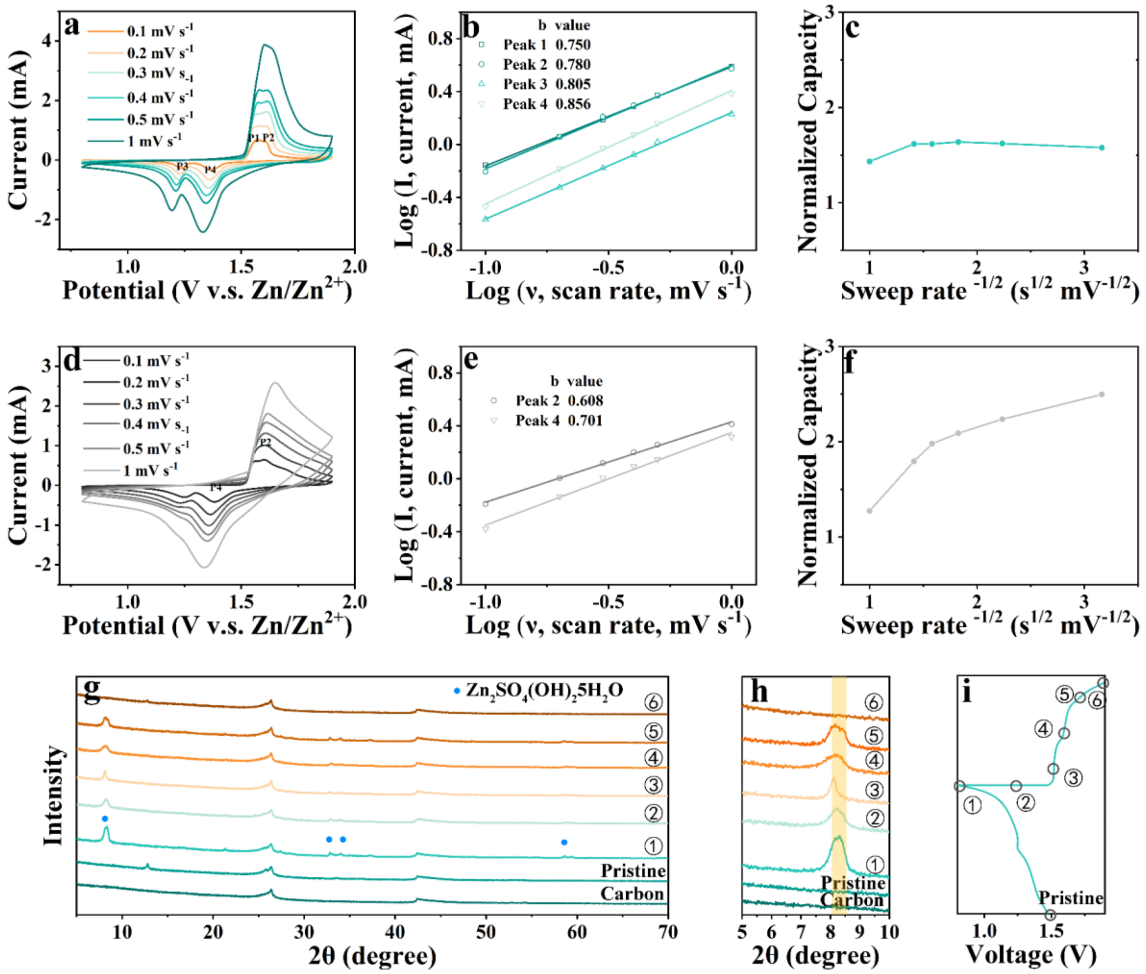

Figure 3.6 (a, d) CV curves with scan rates ranging from 0.1 mV s^{-1} to 1 mV s^{-1}, (b, e) diffusion-capacitive control contribution presented in the bar chart, and (c, f) the relationship between normalized capacity and sweep rate of NMO/VTCNTs and NMO, respectively. (g) *Ex-situ* XRD spectra for the NMO/VTCNTs cathode in the full cell with (h) amplified plots for peak (001) at different states which match with the point marked in (i) during the process of charge and discharge.

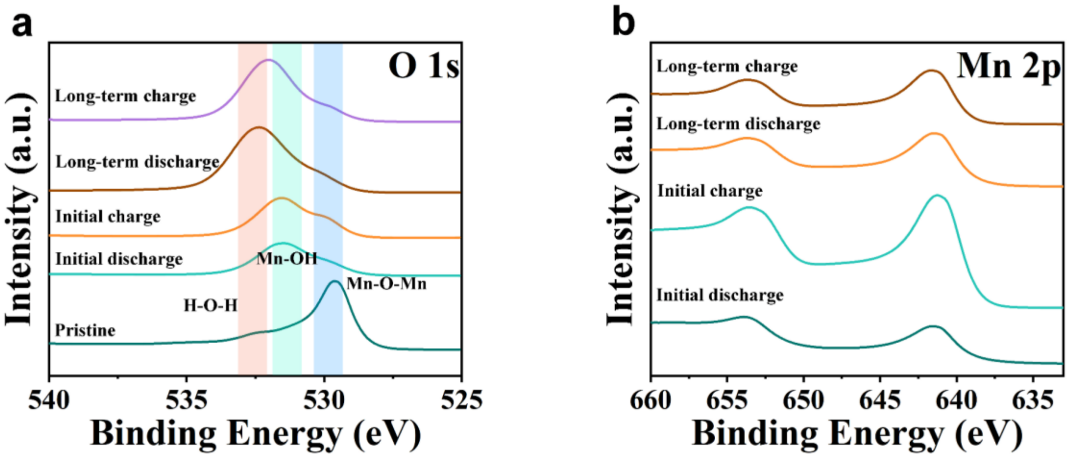

Figure 3.7 *Ex-situ* XPS of (a) O 1s and (b) Mn 2p for NMO/VTCNTs during the charge and discharge.

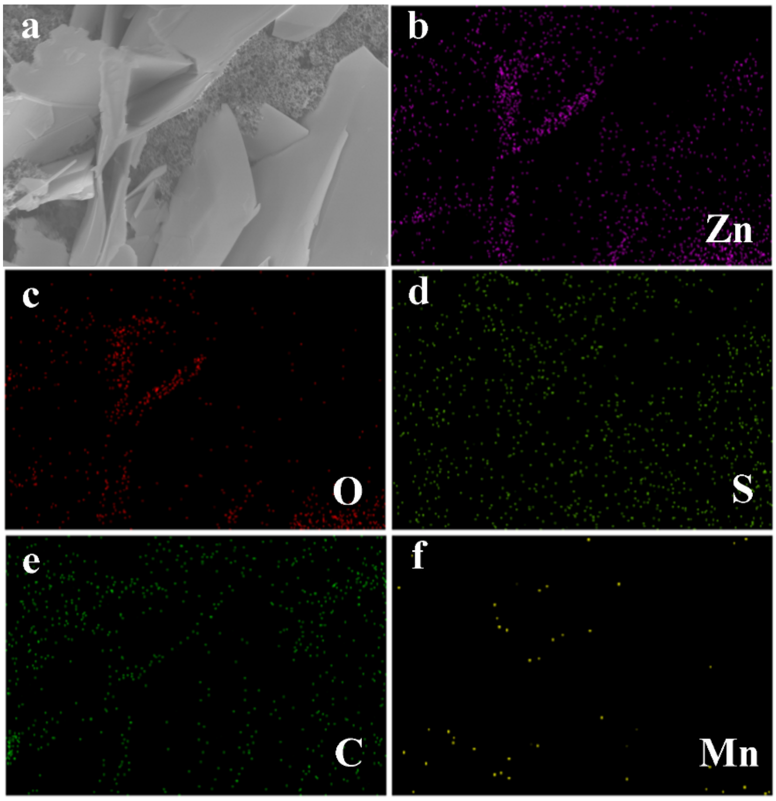

Figure 3.8 SEM image of zinc hydroxide sulfate (ZHS) and its corresponding EDS mapping generated under full discharge state.

Density functional theory (DFT) simulations were conducted to elucidate the mechanisms through which the interfacial structures between NMO and carbon CNTs enhance battery performance by facilitating ion migration and electron transfer. The computational analysis focused on comparing the migration barriers and electronic properties of bulk NMO versus the NMO/CNT interlayer structures. The results, as depicted in Figure 3.9a, show that Zn^{2+} encounter narrow migration channels within the bulk NMO, significantly impeding their movement and affecting the long-term cycling stability of the batteries. Conversely, at the NMO/CNT interface, the presence of larger spaces enables smoother Zn^{2+} migration within the cathode structure, enhancing ionic conductivity. The migration barriers for Zn^{2+} are quantified in Figure 3.9d, showing a reduction from 1.6 eV in the bulk to 1.2 eV at the interface, providing numerical evidence of the interface's beneficial effects on ion migration. Furthermore, the electron transfer dynamics are examined in Figure 3.9c, where a notable increase in electron transfer at the interface is observed, indicating that the Mn-O-C bond significantly alters the electronic environment of the Mn^{2+}.[37] To delve deeper into the electronic structural changes, the d orbitals of manganese ions at both the bulk and interface were analyzed, with results shown in Figure 3.9e. It was found that the d orbitals at the interface are more populated at the Fermi energy level, facilitating easier electron transfer during charge and discharge cycles.

Additionally, the d-band centers of Mn were calculated in both environments, revealing that the d-band center at the interface is closer to the Fermi level compared to the bulk, suggesting higher reactivity of Mn at the interface to participate in electrochemical reactions. To further validate the influence of the interface on the battery's specific capacity, Bader charge analysis was performed on the carbon atoms at the interface before and after zinc ion intercalation. As illustrated in Figure 3.9f, the Bader charges on C atoms change significantly upon Zn embedding, indicating that the CNTs also play a critical role in enhancing the battery's overall specific capacity through electron donation during zinc intercalation. These simulations collectively demonstrate that the interfacial structure not only enhances the ionic and electronic conductivity but also significantly contributes to the improvement of the specific capacity of NMO/CNTs cathodes, aligning well with experimental observations.

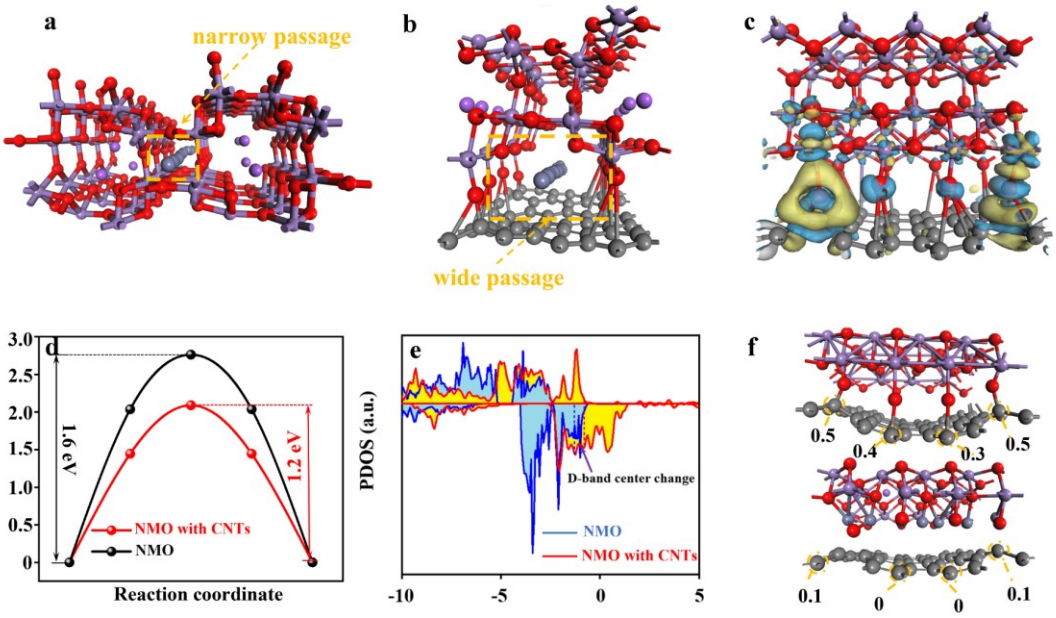

Figure 3.9 Schematic illustration of zinc ion migration in (a) bulk NMO and (b) at the NMO-CNT interface. (c) Charge density difference at the interface. (d) Migration barrier for Zn^{2+} transfer in bulk NMO and at the NMO-CNT interface. (e) Projected density of states of the Mn 3d orbital in both bulk NMO and at the NMO-CNT interface. (f) Bader charge variation of carbon before and after Zn insertion.

When exclusively utilizing HTCNTs for the development of free-standing, binder-free cathodes, even with a low mass loading of approximately 1 mg cm^{-2}, AZIBs equipped with NMO/HTCNTs cathodes demonstrated a specific capacity of 88 mAh g^{-1} at a current density of 2 A g^{-1} after 1000 cycles, as evidenced in Figure 3.10a. This performance is on par with conventional NMO cathodes that incorporate Super P and PVDF binders. In contrast, NMO/LTCNTs displayed exceptional electrochemical performance, achieving 147 mAh g^{-1} at 2 A g^{-1} under similar low mass loading conditions (Figure 3.10a). However, as mass loadings were increased for the fabrication of NMO/LTCNTs, a noticeable decline in specific capacity was observed. Despite LTCNTs having a larger surface area than HTCNTs, their higher degree of entanglement may raise the electron migration barrier, an effect that becomes more pronounced at higher mass loadings, thereby hindering electron dynamics as illustrated in Figure 3.10b.[38]

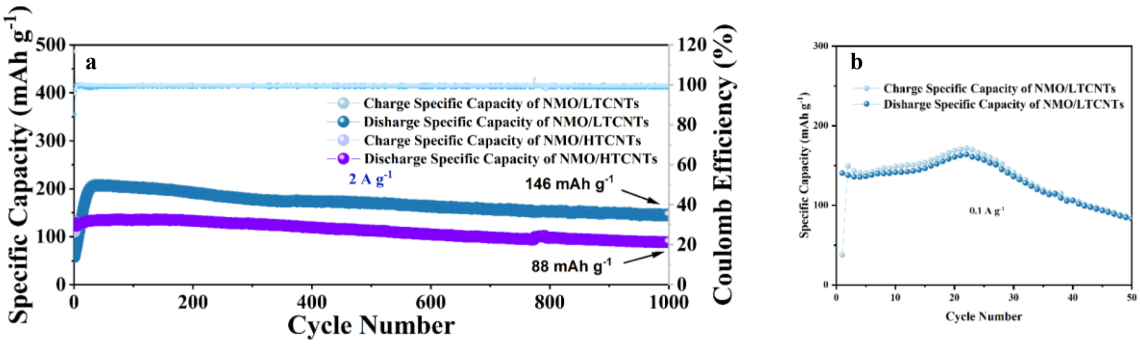

Figure 3.10 (a) Specific Capacity of low loading NMO/LTCNTs and NMO/HTCNTs at the current densities of 2 A g^{-1}. (b) Specific Capacity of high loading NMO/LTCNTs at the current densities of 0.1 A mA g^{-1}.

Further analysis was conducted on high mass loading NMO/VTCNTs cathodes through extensive electrochemical testing, particularly focusing on rate performance, a crucial attribute for practical applications. The rate testing profile for the AZIBs with the NMO/VTCNTs cathode is depicted in Figure 3.11a, providing insights into the electrochemical reactions during the charge and discharge cycles. Clearly defined voltage platforms were observed during both charging and discharging, highlighting the active electrochemical properties of the cathode material.[39] At a lower current density of 0.1 A g^{-1}, the charging voltage platforms were recorded at 1.51 and 1.58 V. With increasing current density, these platforms exhibited a slight upward shift, consistent with the charging behavior described in the CV curves from Figure 3.6a, indicating similar electrochemical properties to those of NMO/LTCNTs. At the peak current density of 5 A g^{-1}, the two charging platforms converged into a single voltage level of 1.62 V, while the discharging voltage platform was noted at 1.32 V at 0.1 mAh g^{-1}, also found in Figure 3.6a. A minor downward shift in the voltage platforms during discharging, correlating with increased current density, demonstrated good agreement with the CV curves.[40] Initial rate testing over the first 30 cycles revealed that the AZIBs with the NMO/VTCNTs cathode maintained a high specific capacity of nearly 400 mAh g^{-1} at 0.1 A g^{-1}. Even when the current density escalated from 0.1 to 5 A g^{-1} and then reverted to 0.1 A g^{-1}, the cathode exhibited a high capacity of 357 mAh g^{-1} (Figure 3.11b). At the highest tested current density of 5 A g^{-1}, the specific capacity of the NMO/VTCNTs cathode sustained at 110 mAh g^{-1}, nearly threefold higher than that of the NMO cathode, underscoring its superior high-rate performance. This enhanced high-rate capability is consistent with observations from previous CV curve analyses, affirming the superior performance of NMO/VTCNTs over standard NMO cathodes in high-rate tests. Additionally, the NMO cathode, without the inclusion of CNTs, exhibited a longer activation process, indicative of suboptimal reaction kinetics.

The incorporation of CNTs markedly enhances the electrochemical performance of NMO cathodes primarily by reducing polarization during battery operation. As depicted in Figure 3.12, the electrochemical profile of the initial reversible cycle for NMO/VTCNTs demonstrates significantly less polarization—167.1 mV—compared to 465.0 mV observed with traditional NMO cathodes on carbon paper. The integration of CNTs creates a 3D conductive network that significantly boosts both electrical and ionic conductivity, thereby enhancing transport kinetics during battery cycling.[41] Moreover, the interface between CNTs, particularly LTCNTs, and NMO facilitates additional ion storage capacities. When LTCNTs and HTCNTs are utilized as cathodes in AZIBs cycling between 0.8 and 1.9 V, they demonstrate relatively limited specific capacities as shown in Figures 3.13a and b. This suggests that the improvement in charge storage capabilities attributed to CNTs may be linked to the interfaces they create. Previous studies have explored the decoupled transport of ions and electrons at interfaces between ionic and electronic conductors, finding that storage at these interfaces tends to follow one-dimensional diffusion patterns more closely than conventional bulk transport within the space charge region. Electron conduction along CNTs, facilitated by their one-dimensional hollow structure, occurs much faster than through NMO, which functions as a semiconductor. As a result, both electron and ion transport mechanisms are theoretically quicker at the interface, enhancing charge storage efficiency compared to traditional bulk storage methods. Furthermore, the distinct heterostructure at the NMO/CNTs interface and the decoupled transport of electrons and Zn^{2+} enhance the mobility of these carriers, consistent with the observed lower energy barriers for Zn^{2+} transport at the interface, as detailed in Figure 3.9d.[42] This improved mobility is also supported by zinc diffusion calculations based on Fick's Law, indicated in the following equation (Equation 3.5).

$$\begin{aligned} j_{Zn} &= -\frac{1}{F^2}\frac{\sigma_{ion}^{\alpha}\sigma_e^{\alpha}}{\sigma_{ion}^{\alpha}+\sigma_e^{\alpha}}\left[\frac{\partial\mu_{ion}^{\alpha}}{\partial C_{ion}^{\alpha}}+\frac{\partial\mu_e^{\beta}}{\partial C_e^{\beta}}+F\frac{\partial\left(\varphi^{\alpha}-\varphi^{\beta}\right)}{\partial C_M}\right]\nabla C_M \\ &= -D^{\delta}\,\nabla C_M \end{aligned} \tag{3.5}$$

Equation 3.5 describes the driving force of the diffusive flux, which is the gradient of the concentration. The value of $\frac{\sigma_{ion}^{\alpha}\sigma_{e}^{\alpha}}{\sigma_{ion}^{\alpha}+\sigma_{e}^{\alpha}}$ can be higher in interface-dominated storage than in bulk storage because both σ_{ion}^{α} and σ_{e}^{α} are enhanced. The term $F\frac{\partial(\varphi^{\alpha}-\varphi^{\beta})}{\partial c_M}$ is zero in bulk because of the homogeneity but nonzero in interfacial storage, causing the Zn^{2+} diffusion coefficient (D_{Zn}) to increase even more during interfacial storage.

To assess the cycling stability of the synthesized materials, low-rate tests were conducted on NMO/VTCNTs and NMO cathodes at a current density of 0.2 A g^{-1}. As demonstrated in Figure 3.11c, the NMO/VTCNTs cathode, with an active material mass loading of approximately 5 mg cm^{-2} and a total cathode mass of about 7.1 mg cm^{-2}, exhibited a discharge capacity of 329 mAh g^{-1}—1.60 times greater than the NMO cathode at an active material mass loading of about 1 mg cm^{-2}. Additionally, the coulombic efficiency consistently stayed around 100% throughout numerous charging and discharging cycles. The capacity of the NMO/VTCNTs cathode slightly increased over time, likely due to the progressive infiltration of the electrolyte into the gaps between the stacked CNTs. The first three cycles of the NMO/VTCNTs, recorded at a scan rate of 0.1mV s^{-1} and displayed in Figure 3.11d, showed excellent reversibility and cycling stability, indicating a similar electrochemical behavior to NMO/LTCNTs, with comparable redox peak positions and intensities. Further tests at current densities of 1 and 2 A g^{-1} (Figures 3.11e and f) were performed to evaluate the high-rate and long-term cycling performance of NMO/VTCNTs. At 1 A g^{-1}, after 200 cycles, the AZIBs with NMO/VTCNTs cathodes achieved a high specific capacity of 225 mAh g^{-1}—2.21 times higher than that of NMO cathodes. Even at a doubled current density of 2 A g^{-1}, the NMO/VTCNTs cathode maintained a high reversible capacity of 158 mAh g^{-1}, with a retention rate close to 100%.

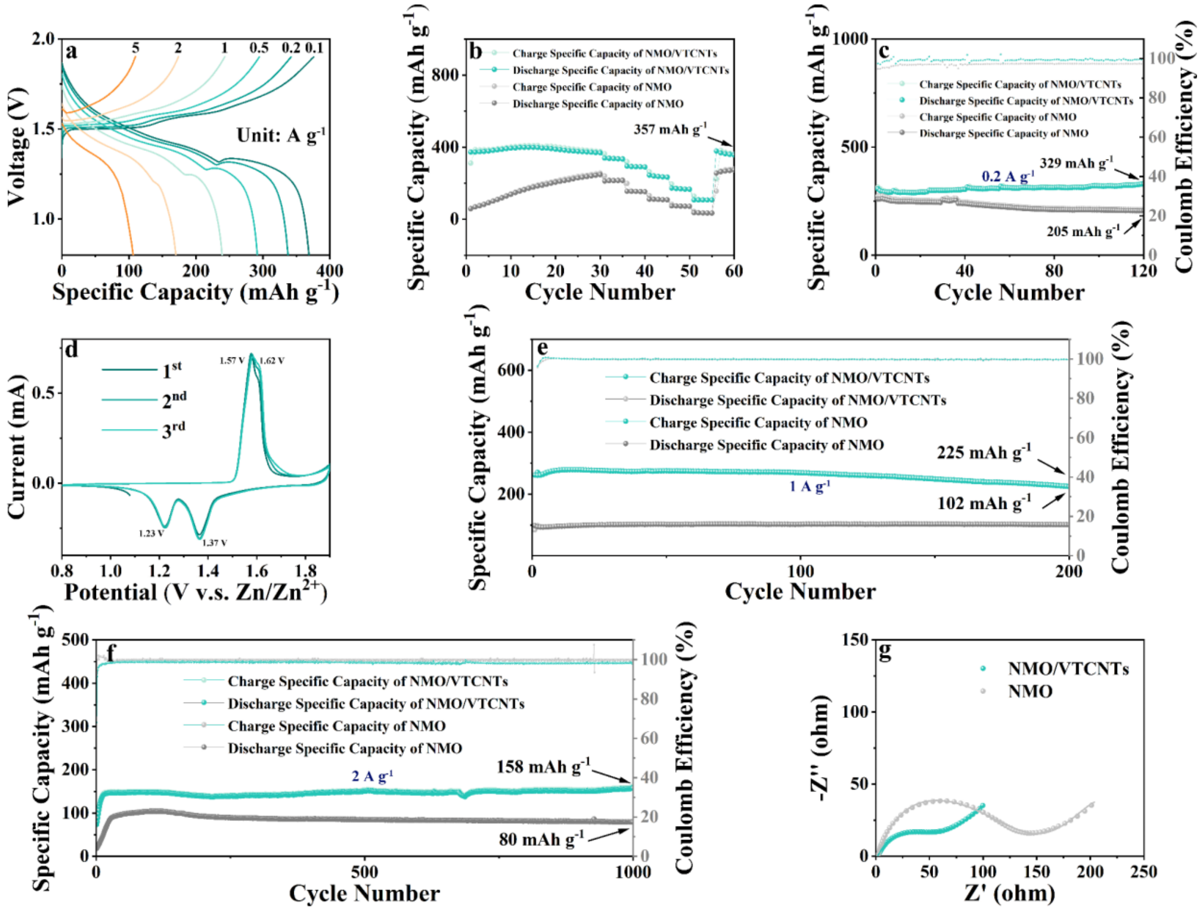

Figure 3.11 (a) Galvanostatic charge-discharge profiles for the NMO/VTCNTs full cell. (b) Comparative cycling performance of NMO/VTCNTs and NMO at varying current densities (0.1–5 A g^{-1}). (c) Low-rate cycling performance of NMO/VTCNTs and NMO at 0.2 A g^{-1}. (d) CV curves of the first three cycles for the NMO/VTCNTs full cell. (e) Cycling performance at 1 A g^{-1}. (f) Long-term cycling performance at 2 A g^{-1}. (g) EIS tests reveal enhanced conductivity for the NMO/VTCNTs cathode compared with NMO.

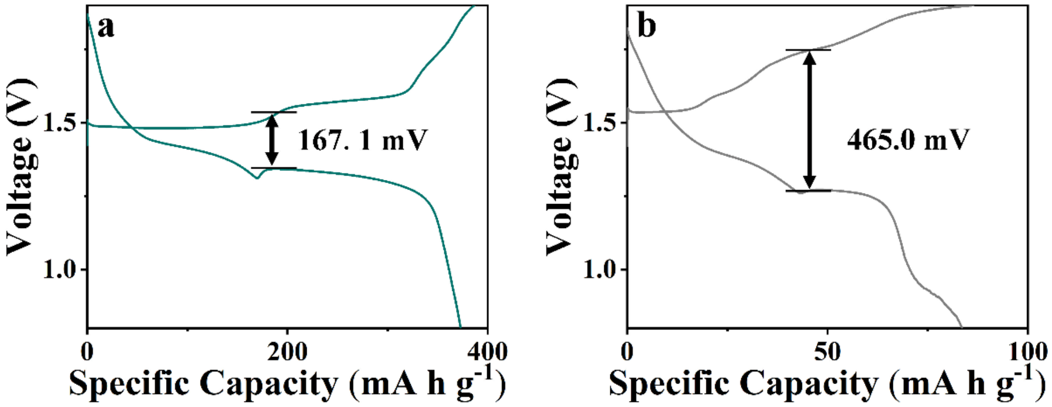

Figure 3.12 Electrochemical profile of initial reversible cycle of (a) NMO/VTCNTs and (b) NMO.

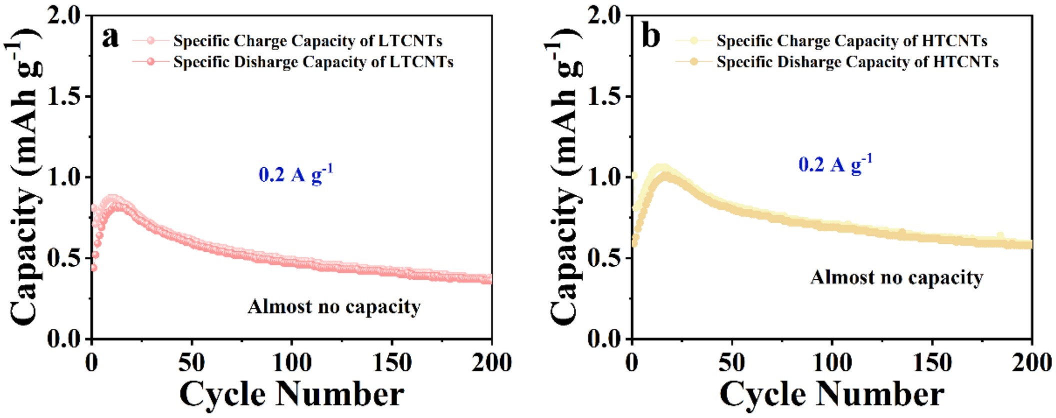

Figure 3.13 Galvanostatic charge-discharge tests of (a) LTCNTs and (b) HTCNTs at a current density of 0.2 A g^{-1}.

EIS tests conducted on NMO/VTCNTs and NMO, depicted in Figure 5g, with equivalent circuit fitting shown in Figure 3.14, highlighted the lower ohmic resistance (R_s = 1.85 Ω) and more effective ion diffusion (R_{ct} = 60.61 Ω) of NMO/VTCNTs compared to NMO (R_s = 2.09 Ω and R_{ct} = 558.18 Ω), signifying improved conductivity. Analysis of the Nyquist plots revealed that NMO/VTCNTs (0.53) had a steeper slope than NMO (0.44), indicating faster ion diffusion within the electrodes as seen in Figures 3.15a and b.

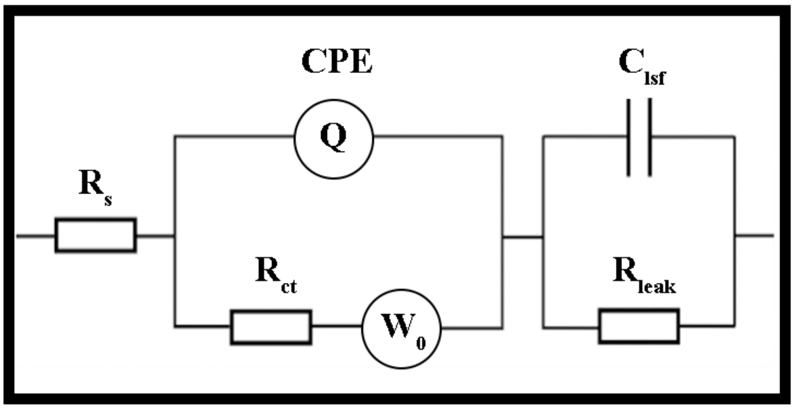

Figure 3.14 The equivalent circuit for EIS fitting.

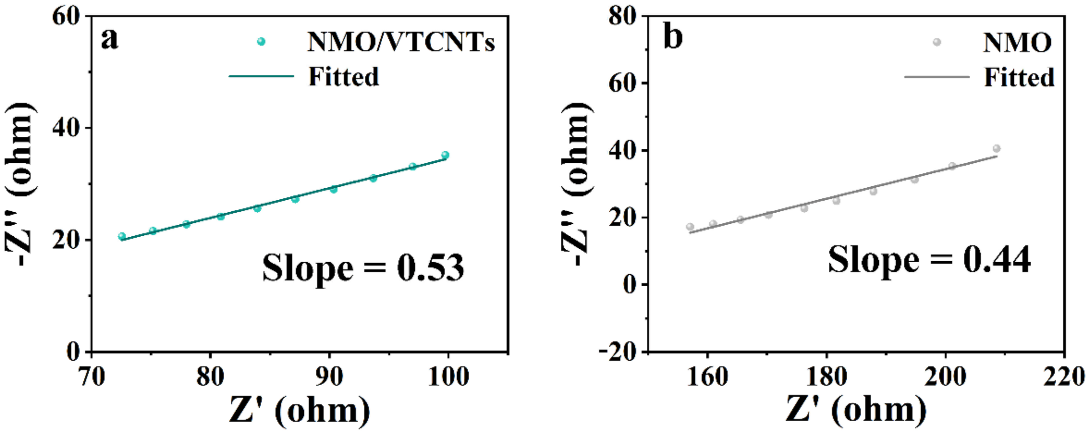

Figure 3.15 Linear fit of (a) NMO/VTCNTs and (b) NMO to the diffusion region in EIS.

Table 3.1 details the electrochemical performance of manganese dioxide and its hybrid structures with carbon materials, particularly CNTs, from research conducted in the 2020-2022. Notably, the exceptional performance of the free-standing, binder-free NMO/VTCNTs cathodes under various current density conditions stands out, offering valuable insights for potential industrial applications.

Table 3.2 The development of MnO_2-based cathode materials in AZIBs compared from 2020 to 2022.

Electrode material	Current density	Cycle	Capacity	Ref
K-δ-MnO_2	0.3 A g^{-1}	100	270 mAh g^{-1}	[43]
	2 A g^{-1}	1000	64 mAh g^{-1}	
Na-δ-MnO_2	0.3 A g^{-1}	100	222 mAh g^{-1}	
	2 A g^{-1}	1000	50 mAh g^{-1}	
Li-δ-MnO_2	0.3 A g^{-1}	100	229 mAh g^{-1}	
	2 A g^{-1}	1000	40 mAh g^{-1}	
CuMO	0.2 A g^{-1}	90	263 mAh g^{-1}	[44]
	5 A g^{-1}	700	101 mAh g^{-1}	
MnO_2@N	0.5 A g^{-1}	500	175 mAh g^{-1}	[6]
	5 A g^{-1}	1000	103 mAh g^{-1}	
β-MnO_2	0.2 A g^{-1}	1000	110 mAh g^{-1}	[45]
CNT@MnO_2	1 A g^{-1}	100	70 mAh g^{-1}	[46]
α-MnO_2/CNTs	2 A g^{-1}	2000	116 mAh g^{-1}	[47]
CNT/MnO_2-PPy	1 A g^{-1}	1000	150 mAh g^{-1}	[48]
CNT@MnO_2	3.6 A g^{-1}	1000	105 mAh g^{-1}	[49]
CNT-CaMO	3 A g^{-1}	6000	90 mAh g^{-1}	[50]
KMO-CNT/graphene	3 A g^{-1}	1000	129 mAh g^{-1}	[51]
	2 A g^{-1}	700	127 mAh g^{-1}	
CNF/MnO_2	3 A g^{-1}	2750	130 mAh g^{-1}	[52]
Zn_xMnO_2/CNTs	3 A g^{-1}	1000	100 mAh g^{-1}	[53]
ɣ-MnO_2/rGO	0.1232 A g^{-1}	200	230 mAh g^{-1}	[54]
MorphGE	6.16 A g^{-1}	500	100 mAh g^{-1}	[55]
PDA@MnO_2@NMC	1 A g^{-1}	3500	200 mAh g^{-1}	[56]
NMO/VTCNTs	0.2 A g^{-1}	120	329 mAh g^{-1}	This work
	1 A g^{-1}	200	225 mAh g^{-1}	
	2 A g^{-1}	1000	158 mAh g^{-1}	

3.5 Summary

In this study, a method was derived for fabricating Mn-based, free-standing, binder-free cathodes utilizing CNTs of varying diameters. This approach not only increases the unit area mass loading of the active material but also boosts the ionic and electronic conductivity of the electrode. By incorporating Na-intercalated Mn oxide into three-dimensional networks of CNTs with varied thicknesses, the specific capacity of AZIBs has been significantly enhanced. The cathodes fabricated using this method demonstrate outstanding capacity performance, achieving 329 mAh g^{-1} after 120 cycles at 0.2 A g^{-1}, 225 mAh g^{-1} after 200 cycles at 1 A g^{-1}, and maintaining 158 mAh g^{-1} at 2 A g^{-1} even after 1000 cycles. This performance is attributed to the effective composite structure of layered NMO integrated with a CNTs network. Beyond just showcasing a cathode material with superior electrochemical properties for AZIBs, this work proposes a scalable approach to utilize CNTs of different thinness to achieve high material loading while preserving high specific capacity. Additionally, the integration of CNTs with NMO creates wider ion conduction channels at the interface, as confirmed by DFT calculations, offering valuable insights for future studies on nanocomposite interfaces.

3.6 References

[1] Y.-Y. Hsieh, H.-Y. Tuan, *Energy Stor. Mater.*, (2024) 103361.

[2] J. Li, W. Zhang, W. Zheng, *Energy Stor. Mater.*, **53** (2022) 646-683.

[3] G. Li, L. Sun, S. Zhang, C. Zhang, H. Jin, K. Davey, G. Liang, S. Liu, J. Mao, Z. Guo, *Adv. Funct. Mater.*, **34** (2024) 2301291.

[4] X. Wang, Z. Zhang, B. Xi, W. Chen, Y. Jia, J. Feng, S. Xiong, *ACS Nano*, **15** (2021) 9244-9272.

[5] T. Zhou, L. Zhu, L. Xie, Q. Han, X. Yang, L. Chen, G. Wang, X. Cao, *Journal of Colloid and Interface Science*, **605** (2022) 828-850.

[6] Y. Zhang, Y. Liu, Z. Liu, X. Wu, Y. Wen, H. Chen, X. Ni, G. Liu, J. Huang, S. Peng, *J. Energy Chem.*, **64** (2022) 23-32.

[7] N. Zhang, Y.-R. Ji, J.-C. Wang, P.-F. Wang, Y.-R. Zhu, T.-F. Yi, *J. Energy Chem.*, **82** (2023) 423-463.

[8] Z. Azmi, K.C. Senapati, A.K. Goswami, S.R. Mohapatra, *J. Power Sources*, **613** (2024) 234816.

[9] W. Shi, W.S.V. Lee, J. Xue, *ChemSusChem*, **14** (2021) 1634-1658.

[10] M.A. Kamenskii, F.S. Volkov, S.N. Eliseeva, E.G. Tolstopyatova, V.V. Kondratiev, *Energies*, **16** (2023) 3221.

[11] Y. Xu, G. Zhang, J. Liu, J. Zhang, X. Wang, X. Pu, J. Wang, C. Yan, Y. Cao, H. Yang, *Energy Environ. Mater.*, **6** (2023) e12575.

[12] A. Hashem Abdelmohsen, S.A. El-khodary, N. Ismail, Z. Song, J. Lian, *Chem. Eur. J.*, **31** (2025) e202403425.

[13] X. Gao, H. Zhang, X. Liu, X. Lu, *Carbon Energy*, **2** (2020) 387-407.

[14] Q. Song, S. Zhou, S. Wang, S. Li, L. Xu, J. Qiu, *J. Chem. Eng.*, **461** (2023) 142033.

[15] P. Yadav, N. Kumari, A.K. Rai, *J. Power Sources*, **555** (2023) 232385.

[16] Y. Zou, J. Sun, Y. Chi, X. Cheng, D. Yang, *EcoEnergy*, (2024).

[17] J. Zhu, Z. Tie, S. Bi, Z. Niu, *Angew. Chem., Int. Ed.*, (2024) e202403712.

[18] N. Bensalah, Y. De Luna, *Energy Technology*, **9** (2021) 2100011.

[19] B. Zhao, P. Jia, L. Yu, Y. Song, Z. Li, Y. Wang, R. Feng, H. Li, X. Cui, H. Cui, *J. Energy Storage*, **73** (2023) 109174.

[20] J.P. Perdew, K. Burke, M. Ernzerhof, *Phys. Rev. Lett.*, **77** (1996) 3865.

[21] D. Vanderbilt, *Phys. Rev. B*, **41** (1990) 7892.

[22] T.A. Halgren, W.N. Lipscomb, *Chemical Physics Letters*, **49** (1977) 225-232.

[23] G. Henkelman, H. Jónsson, *The Journal of chemical physics*, **113** (2000) 9978-9985.

[24] G. Henkelman, B.P. Uberuaga, H. Jónsson, *The Journal of chemical physics*, **113** (2000) 9901-9904.

[25] X. Gao, X. Sun, Z. Jiang, Q. Wang, N. Gao, H. Li, H. Zhang, K. Yu, C. Su, *New J. Chem.*, **43** (2019) 3907-3912.

[26] V. Petkov, *Materials Today*, **11** (2008) 28-38.

[27] H. Dong, J. Li, S. Zhao, Y. Jiao, J. Chen, Y. Tan, D.J. Brett, G. He, I.P. Parkin, *ACS Appl. Mater. Interfaces*, **13** (2020) 745-754.

[28] Y. Qiu, Z. Zhang, T. Zhang, P. Zhang, *Science of the Total Environment*, **848** (2022) 157802.

[29] S. Qiu, R. Guo, Q. Wang, F. Yang, Y. Han, X. Peng, H. Yuan, X. Wang, *International Journal of Energy Research*, **45** (2021) 14985-14994.

[30] R. Chen, C. Zhang, J. Li, Z. Du, F. Guo, W. Zhang, Y. Dai, W. Zong, X. Gao, J. Zhu, *Energy Environ. Sci.*, **16** (2023) 2540-2549.

[31] W. Zhang, Y. Dai, R. Chen, Z. Xu, J. Li, W. Zong, H. Li, Z. Li, Z. Zhang, J. Zhu, *Angew. Chem., Int. Ed.*, **62** (2023) e202212695.

[32] H.-S. Wang, D.-Q. Huang, R.-M. Liu, *Journal of Electroanalytical Chemistry*, **570**

(2004) 83-90.

[33] Q. Liu, A.A. Shinkle, Y. Li, C.W. Monroe, L.T. Thompson, A.E. Sleightholme, *Electrochemistry Communications*, **12** (2010) 1634-1637.

[34] H. Dong, R. Liu, X. Hu, F. Zhao, L. Kang, L. Liu, J. Li, Y. Tan, Y. Zhou, D.J. Brett, *Adv. Sci.*, **10** (2023) 2205084.

[35] X. Deng, J.K. Sarpong, G. Zhang, J. Hao, X. Zhao, L. Li, H. Li, C. Han, B. Li, *InfoMat*, **5** (2023) e12382.

[36] Y. Wu, Y. Tao, X. Zhang, K. Zhang, S. Chen, Y. Liu, Y. Ding, M. Cai, X. Liu, S. Dai, *Science China Materials*, **63** (2020) 1196-1204.

[37] Y. Dai, X. Liao, R. Yu, J. Li, J. Li, S. Tan, P. He, Q. An, Q. Wei, L. Chen, *Adv. Mater.*, **33** (2021) 2100359.

[38] Z. Wu, K. Pei, L. Xing, X. Yu, W. You, R. Che, *Adv. Funct. Mater.*, **29** (2019) 1901448.

[39] Z. Xu, M.M. Rahman, L. Mu, Y. Liu, F. Lin, *J. Mater. Chem. A*, **6** (2018) 21859-21884.

[40] Y.S. Xu, S.J. Guo, X.S. Tao, Y.G. Sun, J. Ma, C. Liu, A.M. Cao, *Adv. Mater.*, **33** (2021) 2100409.

[41] D. Xie, Y. Wang, L. Tian, H. Huang, J. Sun, D.W. Kim, J. Zhao, J. Mao, *Adv. Funct. Mater.*, (2024) 2413993.

[42] M. Zameni, *Magna Scientia Advanced Research and Reviews*, **10** (2024) 123-131.

[43] Q. Xie, G. Cheng, T. Xue, L. Huang, S. Chen, Y. Sun, M. Sun, H. Wang, L. Yu, *Materials Today Energy*, **24** (2022) 100934.

[44] R. Zhang, P. Liang, H. Yang, H. Min, M. Niu, S. Jin, Y. Jiang, Z. Pan, J. Yan, X. Shen, *Chemical Engineering Journal*, **433** (2022) 133687.

[45] W. Liu, X. Zhang, Y. Huang, B. Jiang, Z. Chang, C. Xu, F. Kang, *Journal of Energy Chemistry*, **56** (2021) 365-373.

[46] Y. Ren, F. Meng, S. Zhang, B. Ping, H. Li, B. Yin, T. Ma, *Carbon Energy*, (2022).

[47] J. Xie, G. Liu, J. Sun, R. Zheng, W. Zhao, T. Chu, H. Lin, Y. Xu, S. Gao, Z. Sui, *Diamond and Related Materials*, **125** (2022) 109024.

[48] Y. Zhang, G. Xu, X. Liu, X. Wei, J. Cao, L. Yang, *ChemElectroChem*, **7** (2020) 2762-2770.

[49] A. Huang, J. Chen, W. Zhou, A. Wang, M. Chen, Q. Tian, J. Xu, *Journal of*

Electroanalytical Chemistry, **873** (2020) 114392.

[50] W. Wang, C. Zhang, Z. Chen, R. Huang, Y. Nie, P. Liu, K. Liu, J. Yan, *Dalton Transactions*, **51** (2022) 9477-9485.

[51] T.-H. Xu, S. Liou, F.-L. Hou, Y.-Y. Li, *Journal of Alloys and Compounds*, **913** (2022) 165278.

[52] X. Chen, W. Li, Z. Zeng, D. Reed, X. Li, X. Liu, *Chemical Engineering Journal*, **405** (2021) 126969.

[53] F. Jing, J. Pei, Y. Zhou, Y. Shang, S. Yao, S. Liu, G. Chen, *Journal of Colloid and Interface Science*, **609** (2022) 557-565.

[54] N. Subjalearndee, N. He, H. Cheng, P. Tesatchabut, P. Eiamlamai, P. Limthongkul, V. Intasanta, W. Gao, X. Zhang, *Advanced Fiber Materials*, **4** (2022) 457-474.

[55] F. Cao, B. Wu, T. Li, S. Sun, Y. Jiao, P. Wu, *Nano Research*, **15** (2022) 2030-2039.

[56] B. Wang, Y. Zeng, P. Chen, J. Hu, P. Gao, J. Xu, K. Guo, J. Liu, *ACS Applied Materials & Interfaces*, (2022).

Chapter 4 Co-intercalation strategy for simultaneously boosting two-electron conversion and bulk stabilization of manganese-based cathodes in aqueous Zn-ion batteries

4.1 Introduction

MnO_2 cathodes possess a high theoretical capacity (308 mAh g^{-1}), outstanding cycling stability, and robust high-rate capabilities—essential for practical AZIBs applications.[1] While tunnel structures in MnO_2 provide open pathways and ample active sites for Zn^{2+} diffusion and storage, they are susceptible to structural collapse during discharge.[2] In contrast, layered MnO2, featuring channel spacings of around 7 Å, is inherently more favorable for rapid, reversible Zn^{2+} insertion and extraction.[3] However, challenges remain, such as the phase transitions in δ-MnO_2 during cycling, which can cause significant volume changes and structural collapses, adversely affecting the battery's performance.[4] Additionally, the Jahn-Teller effect, due to the degeneracy of electronic energy levels in [MnO_6] octahedra, can distort and dissolve Mn-based active materials, reducing cycling stability.[5-7] Moreover, the *in-situ* formation of ZHS on the cathode surface, while facilitating electron transfer during cycling, leads to increased polarization and gradual deactivation of the cathode materials due to its poor reversibility.[8]

To successfully industrialize AZIBs, it is urgent to develop methods that are both economically viable and scalable for cathode production.[9] While the use of advanced materials like CNTs can enhance battery performance, their high cost and production complexities make them difficult to use extensively in industrial applications.[10] This challenge necessitates exploring alternative strategies that focus on cost-effectiveness and scalability without compromising performance.[11] One promising approach is the development of new Mn-based cathode materials. By synthesizing new Mn-based cathodes, it is possible to leverage the inherent advantages of manganese — such as high energy density and environmental benignity — while potentially overcoming the limitations associated with current cathode materials used in AZIBs.[12] Moreover, innovations in the synthesis of Mn-based cathodes could lead to improvements in battery stability and energy efficiency, thereby enhancing the overall performance and reducing production costs.[13] Such advancements would make the large-scale deployment of AZIBs more feasible, promoting their adoption in grid storage and other applications where efficient, large-scale energy storage solutions are required.[14]

Researchers have devoted considerable efforts to overcoming challenges in battery technology through innovative strategies like material combinations, ion intercalation, etc.[15-17] Specifically, in the domain of Mn-based cathode materials, stability in Zn^{2+} storage has been achieved through a process known as ion pre-intercalation. This technique, which involves inserting ions such as H^+, metal cations, and NH_4^+ into host materials prior to battery operation, effectively expands the interplanar spacing within these materials.[18-20]. On the other hand, transitioning from traditional alkaline electrolytes to a weakly acidic $ZnSO_4$-based electrolyte helps mitigate parasitic reactions and curb the formation of passivation by-products, enabling MnO_2 to exhibit a reversible theoretical specific capacity of 308 mAh g^{-1} through the Mn^{4+}/Mn^{3+} redox pair.[21] On the other hand, adjusting the pH of the electrolyte and increasing the charge voltage could potentially unlock a higher theoretical capacity of 616 mAh g^{-1} for MnO_2 by activating the Mn^{4+}/Mn^{2+} redox pair.[22] Although the single-electron Mn^{4+}/Mn^{3+} redox reactions often lead to poor durability due to the octahedral structure of MnO_2 being unsuitable for Zn^{2+} insertion/extraction, the two-electron Mn^{4+}/Mn^{2+} redox processes offer considerable promise.[23] These processes have been effectively demonstrated in $MnSO_4$ electrolytes enhanced with strongly acidic conditions, which promote Mn vacancies and facilitate rapid proton and electron kinetics, thus maximizing the electrolysis of MnO_2.[24] However, the application of such acidic electrolytes in industrial-scale energy storage is limited due to concerns over equipment corrosion and safety.[25] Therefore, it is key to develop Zn//MnO_2 batteries that operate based on a two-electron transfer mechanism under more moderate conditions to align with industrial requirements and ensure safety.

Various methods have been suggested to enhance the Mn^{2+}/Mn^{4+} two-electron transfer in AZIBs.[26] Liang et al. introduced an ion concentration/dilution strategy in the electrolyte, which has demonstrated the capability to reach high capacity up to 460 mAh g^{-1}.[27] Additionally, the use of acetate in the electrolyte has proven effective in facilitating two-electron transfers in MnO_2, achieving a specific capacity of 556 mAh g^{-1}.[28] However, these electrolyte modifications primarily influence surface reactions, and the most effective results—high capacity and stable cycles—are often achieved with thin electrodes under low mass loading conditions, typically less than 1 mg cm^{-2}. The challenge lies in simultaneously enhancing surface Mn^{2+}/Mn^{4+} two-electron transfers while maintaining the structural integrity of the host material, particularly at higher mass loadings. Recent studies have shown that MnO_2 intercalated with Cu^{2+} can boost the Mn^{2+}/Mn^{4+} redox activity in cathodes of AZIBs, though its cycling stability is compromised at high mass loadings.[29] The effect of Cu^{2+} on manganese deposition and dissolution stems from a complex interplay that includes the Jahn-Teller (JT) effect in the host material and the reversible nature of by-product ZHS, among other contributing factors.[29] Thus, deepening our understanding of how ion pre-intercalation and the in-situ generation and dissolution of ZHS on the active material surface interact is crucial for improving the performance and durability of Mn-based cathodes in AZIBs.

Here, a δ-MnO_2 (NCMO) cathode was devised by co-intercalating sodium and copper ions, offering both stable cycling and high specific capacity at elevated mass loadings in AZIBs (Figure 4.1). Copper ion introduction catalyzes the Mn^{2+}/Mn^{4+} redox transition, while Na^+ pre-intercalation amplifies this effect. The smaller ionic radius of Cu^{2+} expedites its diffusion in the electrolyte, facilitating rapid $Cu^{(0)}/Cu^{2+}$ conversion during charging and discharging, and also accelerates the dissolution of the transient $Zn_yMnO(OH)_2$ phase by inducing JT distortion. Consequently, the combined action of

Na^+ and Cu^{2+}, along with the formation and dissolution of $ZnyMnO(OH)_2$ and ZHS, boosts the cathode's conversion processes and improves structural stability throughout electrochemical cycling.

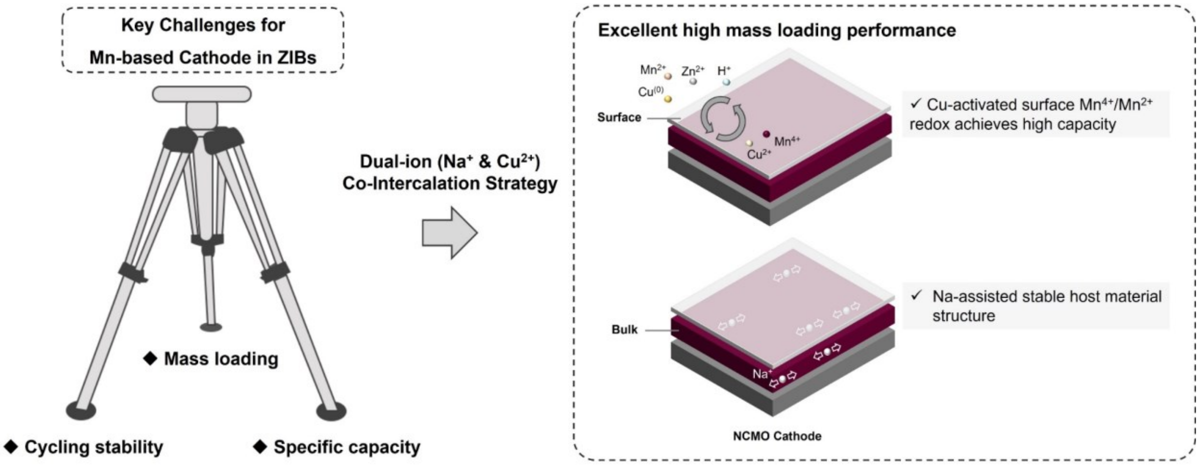

Figure 4.1 Schematic illustration of a manganese oxide cathode employing a dual-ion co-intercalation strategy, which enhances the Mn^{2+}/Mn^{4+} two-electron redox process at the surface while preserving the stability of the host structure to address key challenges involving mass loading, cycling stability, and specific capacity in manganese-based cathodes.

4.2 Experimental Section

4.2.1 Chemicals

All chemicals were used as purchased without further purification. Poly(vinylidene fluoride), average Mw ~534,000, powder (Sigma-Aldrich); 1-methyl-2-pyrrolidinone, 99% (Sigma-Aldrich); $Cu(NO_3)_2$, 99% (Sigma-Aldrich); $Mn(NO_3)_2 \cdot 4H_2O$, 99% (Sigma-Aldrich); NaOH, reagent grade, 97%, powder (Sigma-Aldrich); H_2O_2, 30 % (w/w) in H_2O (Sigma-Aldrich); $MnSO_4 \cdot 1H_2O$ (≥99%) (Sigma-Aldrich); $ZnSO_4 \cdot 7H_2O$ (≥99%) (Sigma-Aldrich).

4.2.2 Synthesis of NCMO

NCMO was synthesized through a straightforward co-precipitation process. Specifically, solution **A** was prepared by dissolving 4 mmol of $Mn(NO_3)_2 \cdot 4H_2O$ in 10 mL of deionized water, while solution **B** consisted of 3 mmol of $Cu(NO_3)_2$ in 10 mL of deionized water. For solution **C**, 27.5 mmol of NaOH was dissolved in 10 mL of deionized water, and solution **D** was made by mixing 6 mL of 30 wt% H_2O_2 with 45 mL of deionized water. After sonicating solution **C** for 20 mins and stirring solutions **A** and **B** for 10 mins, solutions **B** and **C** were quickly added to solution **A** and stirred for another 5 mins. Then, solution **D** was rapidly poured into the mixture under vigorous stirring for 10 more mins, producing a black precipitate. This mixture was kept in an ice bath for 48h to form solution **E**. After sufficient aging, solution **E** was centrifuged at 4500 r min^{-1} for 10 mins, and the resulting brown-black powder was freeze-dried for 48h, yielding the NCMO nanomaterial. For comparison, NMO was synthesized following the same procedure described in previous work.

4.2.3 Materials characterization

The crystal structure evolution following ion intercalation was examined by XRD (Rigaku miniFlex600) using Cu-Kalpha radiation (λ=0.70 nm) in the 2theta range of 5° to 40°, and Mo-Kalpha radiation (λ=0.15 nm) in the 2theta range of 5° to 70°. Sample morphologies were observed via field emission scanning electron microscopy (FE-SEM, FEI Verios G4 UC) equipped with an EDS attachment; the samples were coated with platinum before SEM imaging. For TEM (JEOL JEM2100F), samples were dispersed in acetone and placed on a holey carbon grid. XPS measurements were carried out on a K-Alpha+ (Thermo Fisher Scientific Messtechnik) to investigate the oxidative states at different voltages. Imaging Processing and Data Analysis: Micro-CT (ZEISS Xradia 620 Versa with 40x lens) projections were reconstructed using a filtered-back projection algorithm (XMReconstructor, Carl Zeiss Inc.). The reconstructed datasets were then imported into Avizo 2020.2 (ThermoFisher) for segmentation and quantification, with a median filter applied to improve the signal-to-noise ratio. The pristine material, imaged by micro-CT, was segmented (based on grayscale values) into three phases: active material (NMO), carbon nanotubes, and pores.

4.2.4 Electrochemical measurement

The slurry was prepared by combining the active materials (NCMO, NMO, and ZHS), carbon black (Super P, TIMCAL Graphite & Carbon), and poly(vinylidene fluoride) (PVDF, MW 534000, Sigma-Aldrich) at a weight ratio of 7:2:1 in N-methyl-2-pyrrolidone (NMP). The mixture was then applied onto carbon paper using an automatic coating machine. After drying in a vacuum oven at 60 °C for 24h, cathodes with approximately 1–10.9 mg cm^{-2} of active material were obtained. CR2032 coin cells were assembled in an open-air environment by standard methods, using glass fibers (Whatman GF/A) as the separator and zinc foils as the anode. Additionally, 2 M $ZnSO_4$, as well as 2 M $ZnSO_4$ and 0.2 M $MnSO_4$ were used as the electrolyte. The electrolyte for ZHS full cells were 2 M $ZnSO_4$, 2 M $ZnSO_4$ and 0.2 M $MnSO_4$ as well as 2 M $ZnSO_4$, 0.2 M $MnSO_4$ and 0.1M $CuSO_4$. The electrolyte of the proton full cell is H_2SO_4 whose pH value is adjusted to be the same as that of 2M $ZnSO_4$. The coin cells were tested using NEWARE test systems at 25 °C. The current density and specific capacity were calculated using only the weight of the active material. CV tests were performed using a ZIVE SP1 potentiostat analyzer (WonA Tech, Korea) at 25 °C. CV tests were performed at various scan rates (0.8 to 1.9 V versus Zn^{2+}/Zn). EIS tests were performed using a ZIVE SP1 impedance analyzer (WonA Tech, Korea) in the frequency range of 10^5–10^{-1} Hz.

4.3 Computational methods

In the present study, the computational work was done by Dr. Chengyi Zhang and Dr. Chen Shen and the VASP was used[30] based on DFT and the projector-augmented-wave (PAW) pseudopotential approach.[31, 32] Perdew–Burke–Ernzerhof (PBE) generalized gradient approximation (GGA) functional[33] and Hubbard correction[34] with U_{eff} 5.00 eV are used. The cutoff energy for plane-wave basis is set high enough at 800 eV, and the magnetic moment of each Mn atom is initially set at ±3.00 μ_B corresponding to Mn. Geometrical optimizations were undertaken with unit-cell relaxations. For the k-points, a Γ-centered grid with 12 × 12 × 4 for MnO_2 was used. The tetrahedron method was used for the DOS calculations.[35]

4.4 Results and discussion

4.4.1 Theoretical analysis

To investigate the stacking-selective self-intercalation in δ-MnO_2, DFT calculations were used. The antiferromagnetic δ-MnO_2 phase was chosen as our host structure for these simulations. As depicted in Figure 4.2a, two distinct structural models of δ-MnO_2 were examined, involving the intercalation of both individual elements (Na, Cu) and a combination of these elements (Na & Cu). The δ-MnO_2 phase is characterized by a hexagonal lattice structure within the space group P63/mmc (194), as detailed in Figure 4.2a. The geometrically optimized lattice constants obtained were a = 2.925 Å and c = 11.427 Å, consistent with previous studies.[36] The band structure for pristine δ-MnO_2 is shown in Figure 4.2b, indicating its semiconductive nature with a band gap of 1.70 eV. Upon intercalation of either single elements (Na or Cu), the band gap diminishes, suggesting an introduction of net charges by the intercalants. This is illustrated in Figures 4.2c and d, where one or two flat bands intersect the Fermi level, implying enhanced electronic conductivity of δ-MnO_2 when intercalated with a single element, thus improving its electron transfer capabilities. For the binary intercalation of Na and Cu, additional bands intersect the Fermi level as shown in Figure 4.2e, creating more effective pathways for charge conduction. The DFT findings clearly show that the combined intercalation of Na and Cu effectively alters the electronic structure of δ-MnO_2, facilitating faster electron transfer processes.

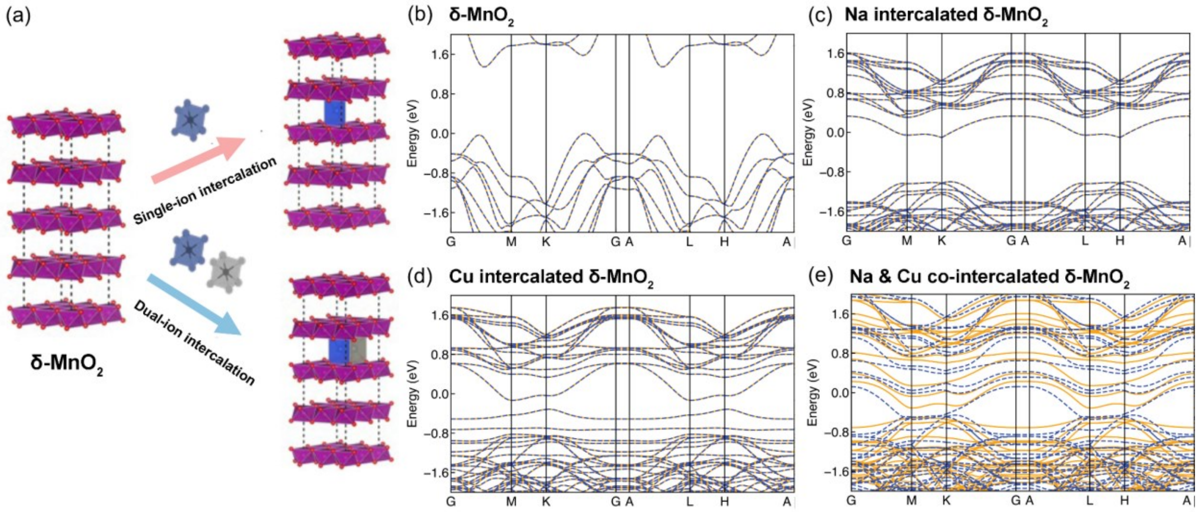

Figure 4.2 (a) Utilized ion intercalation strategy for δ-MnO_2 cathode materials. Band structures of (b) δ-MnO_2, (c) Na intercalated δ-MnO_2, (d) Cu intercalated δ-MnO_2, and (e) Na & Cu co-intercalated δ-MnO_2 based on DFT modeling.

4.4.2 Materials characterization

Capitalizing on the advantages of dual-ion intercalation in cathode materials, we synthesized δ-MnO_2 co-intercalated with Na^+ and Cu^{2+} (NCMO). Scanning electron microscopy (SEM) reveals a uniform flake-like morphology measuring 1–1.5 μm in diameter (Figure 4.3a), while the enlarged view (Figure 4.3b) shows flake thicknesses around 50 nm, contributing to a sizable surface area favorable for electrochemical reactions. Scanning transmission electron microscopy (STEM) images (Figures 4.3c–e) provide further insight into the crystal structure of NCMO, with an interlayer spacing of 3.53 Å (Figure 4.3d)—a bit over half the distance of the (001) plane, indicating facilitated ion intercalation. A top view of the MnO_6 octahedron (Figure 4.3e) underscores the layered structure, featuring a 2.22 Å d-spacing corresponding to the (201) plane. Elemental mapping (Figures 4.3f–j) confirms a uniform distribution of Na, Cu, Mn, and O, demonstrating their homogeneous integration within the cathode material.

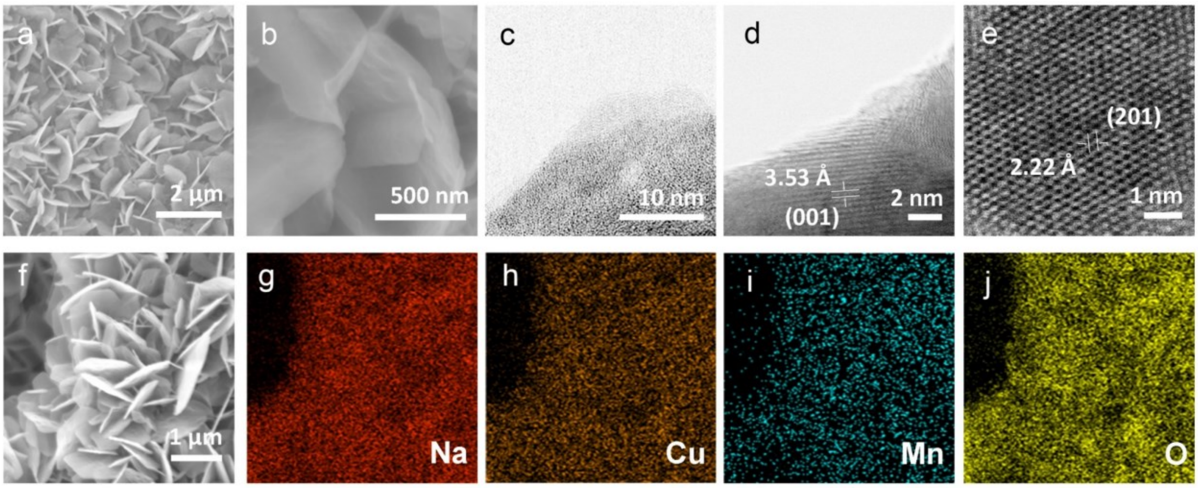

Figure 4.3 (a) low-, (c) high-resolution SEM images of the morphology of the NCMO. (d) low-, (e) high-resolution and (f) atomic resolution STEM images for surface structures of NCMO. (g-k) EDS mapping images of NCMO show that Na, Cu, Mn, and O elements are uniformly distributed.

XRD patterns of NCMO, displayed in Figure 4.4a, reveal characteristic peaks at 2θ angles of 5.893°, 11.751°, 15.250°, 16.481°, and 27.734°, corresponding to the (001), (002), (200), (111), and (001) planes, respectively.[37] These peaks align with the Birnessite structure (JCPDS no. 43-1456), which has lattice parameters a = 5.175(3) Å, b = 2.849(1) Å, c = 7.338(5) Å, with $\alpha = \gamma$ = 90° and β = 103.19(4)°, and a unit cell volume of 105.3(6) Å3.[38] This structure matches that of previously reported Na-intercalated Mn oxide, indicating that the addition of Cu does not alter the crystal structure.[39] XPS was used to analyze the atomic ratios and average oxidation states (AOS) of the elements. A high oxygen content was noted, attributed to surface oxygen adsorption. The Mn 2p spectrum exhibits two peaks with a binding energy difference of 11.8 eV, whereas the Mn 3s spectrum shows a difference of 5.28 eV (see Figures 4.4b and c). The AOS of Mn, calculated from the Mn 3s peak using the formula AOS = 8.956 – 1.126ΔEs, is 3.01.[39] The integration of Cu is confirmed by a Cu LM3 peak observed between the Mn 2p peaks and a distinct Cu 2p peak in Figure 4.4d.[40] Na presence is verified by a characteristic Na 1s peak at 1071 eV in Figure 4.4e. The O 1s spectrum in Figure 4.4f is decomposed into three peaks corresponding to adsorbed water (H–O–H, 532.5 eV), surface-adsorbed oxygen (Mn–OH, 531.2 eV), and lattice oxygen (Mn–O–Mn, 529.6 eV).

X-ray micro-Computed Tomography (CT) was employed to inspect the 3D morphology of the NCMO electrode, showing a uniform distribution of NCMO nanoparticles on the current collector. Segmentation of the active material, carbon fiber, and pore phases based on grey scale levels allowed visualization of a complex 3D structure with a varied pore size distribution in Figure 4.5a. Simulations of tortuosity and flux density based on the segmented structures indicate similar mass transfer capabilities in three dimensions, with a porosity ε of 0.72 and tortuosity factors of 1.8-1.9 in the X direction (see Figure 4.5b), and 1.3-1.5 in the Y (Figure 4.5c) and Z (Figures 4.4g and 4.5d) directions. The effective diffusion coefficient, ranging from 0.40 to 0.55 as shown in Figure 4.4h, suggests superior reactant transport capabilities compared to previous studies in AZIBs and LIBs.

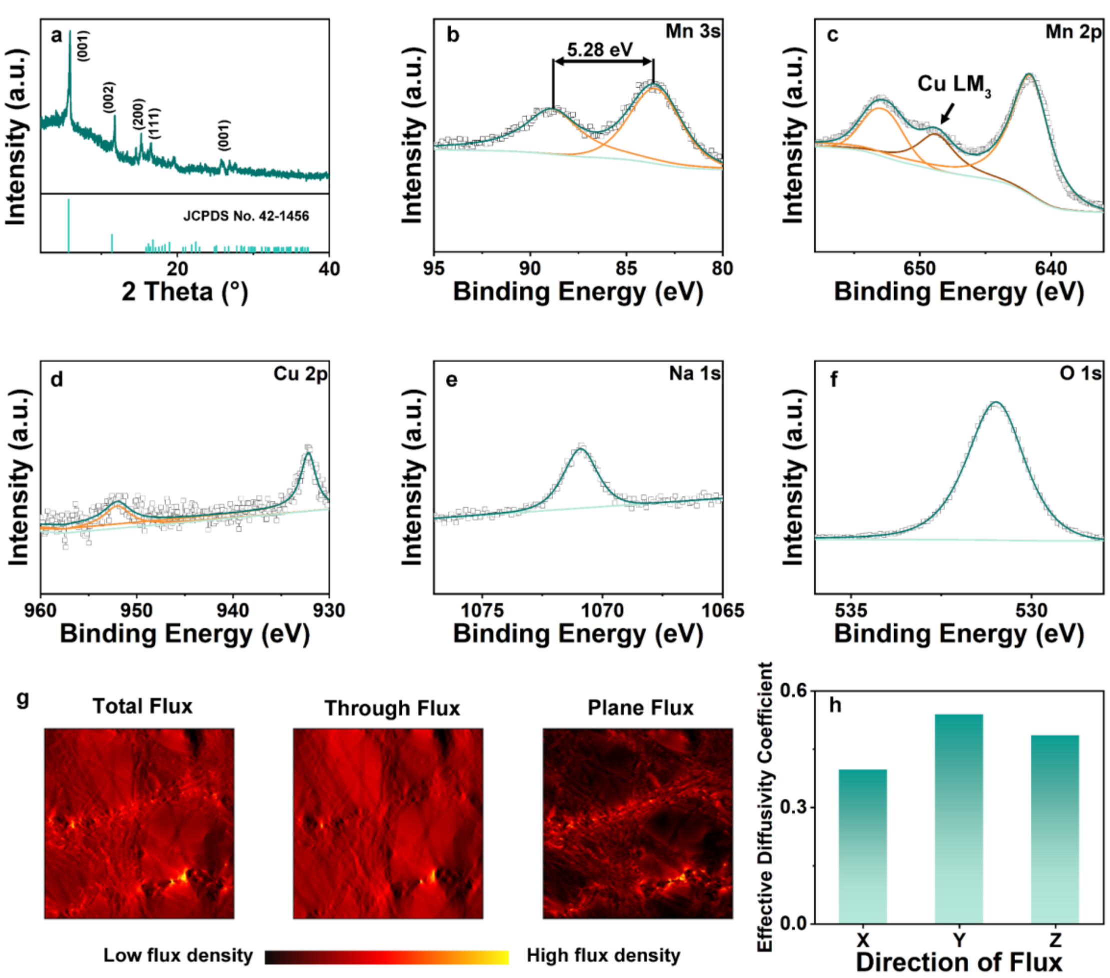

Figure 4.4 (a) (a) XRD pattern of NCMO. (b–f) XPS spectra focusing on Mn 3s, Mn 2p, Cu 2p, Na 1s, and O 1s, respectively. (g) Flux density heatmap in the Z direction. (h) Effective diffusivity coefficients of 0.40, 0.55, and 0.49 in the X, Y, and Z directions, respectively.

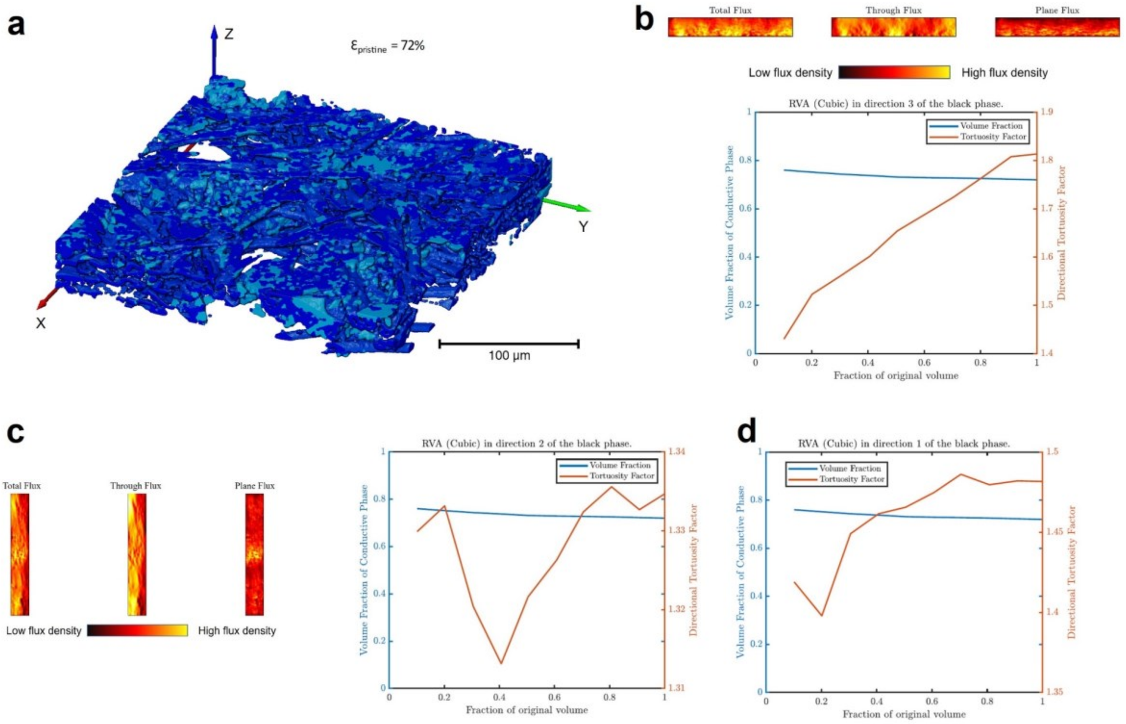

Figure 4.5 (a) A CT image of the NCMO cathode reveals a uniform distribution of the active material. (b) The flux density heatmap in the X direction, along with the volume fraction, tortuosity, and fraction of original volume plotted against the X-axis. (c) The flux density heatmap in the Y direction, showing the corresponding volume fraction, tortuosity, and fraction of original volume at the Y-axis. (d) The relationships among volume fraction, tortuosity, and fraction of original volume at the Z-axis.

4.4.3 Electrochemical characterizations

The electrochemical behaviors of two cathode types—NCMO and NMO—were evaluated. NMO served as a control and was synthesized following previously established methodologies. The primary objective was to assess the impact of Cu intercalation on the electrochemical properties of the cathodes. To this end, CV tests were conducted on both NCMO and NMO cathodes prepared using identical procedures, including the incorporation of binder, carbon additives, and carbon paper collectors. These tests were carried out over a range of scan rates from 0.1 to 1 mV s^{-1} within a potential window of 0.8 to 1.9 V. The CV results, illustrated in Figures 4.6a and d, demonstrate that at lower scan rates, the NCMO cathode exhibits two distinct pairs of redox peaks, with reduction peaks observed at 1.37 and 1.23 V, and oxidation peaks at 1.55 and 1.59 V. In contrast, the NMO cathode displays similar redox pairs at 1.36, 1.23, 1.56, and 1.61 V, though these exhibit slightly larger polarization compared to those of the NCMO cathode.

The cells equipped with NCMO cathodes not only mirror the redox peak shapes seen with NMO, indicating comparable charge storage mechanisms, but also suggest that typical Mn-based cathodes undergo similar redox reactions within an aqueous $ZnSO_4$ electrolyte during cycling.[41] Furthermore, the CV curves of the NCMO cathodes maintain consistency across various scan rates, reinforcing the similarity in reaction behaviors and kinetics irrespective of the applied rate. As the scan rate increases, the NMO electrode exhibits a noticeable shift in behavior. Beginning at 0.2 mV s^{-1}, two pairs of redox peaks gradually merge into a single pair; by 0.3 mV s^{-1}, both oxidation peaks have converged and shifted to higher potentials. Generally, in quasi-reversible electrochemical reactions, the potential difference ($\Delta\varphi$) between oxidation and reduction peaks widens with increasing scan rate, though this effect is less pronounced in highly reversible systems. As shown in Figure 4.6d, the peak shifts for P1, P2, and P3 in the NMO cathode are 0.049, 0.059, and 0.047 V, respectively. In contrast, the NCMO cathode (Figure 4.6a) exhibits much smaller shifts of 0.018, 0.030, and 0.025 V. Notably, the reduction peak associated with Zn^{2+} in the NCMO cathode is more prominent, suggesting a more stable and reversible electrochemical system.[42] This enhanced reversibility and reduced polarization in the NCMO cathode are likely due to the beneficial effects of Cu intercalation, which sustains minimal variation between peak positions across both high and low scan rates.

To deepen the understanding of the kinetic behaviors of different cathode materials, an analysis of their diffusion-controlled and capacitive contributions was conducted, focusing on the three prominent peaks observed in Figures 4.6a and d. The relationship between the peak current (i) and the sweep rate (v) is crucial for evaluating these contributions. This relationship is theoretically described by Equation (4.1), which stipulates how these variables interact within the electrochemical framework.

$$i = a\upsilon^{b} \tag{4.1}$$

hence, $\log(i) = \log(a) + b\cdot\log(\upsilon)$

For the NCMO cathode, the b values for peaks P1, P2, and P3 were found to be 0.60, 0.55, and 0.73, respectively.[28] These values indicate that the cathode's reactions are primarily controlled by diffusion processes. Similarly, the NMO cathode shows b values of 0.63, 0.59, and 0.71 for peaks P1, P2, and P3, respectively, suggesting a similar dominance of diffusion-controlled kinetics. As depicted in Figures 4.6c and f, the normalized capacity of the NMO cathodes decreases more sharply with increasing sweep rates compared to the NCMO cathodes. This trend suggests that NCMO cathodes offer superior performance at higher rates, making them potentially more suitable for applications requiring rapid charging and discharging.

Ex-situ XRD analysis was conducted to clarify the energy storage mechanism of NCMO cathodes under different voltage conditions. Specifically, the structural evolution of NCMO was monitored at selected charge and discharge states over a potential range of 0.8 to 1.9 V at 1 A g^{-1}, as shown in Figure 4.7a. The XRD patterns indicated no significant alterations to the overall phase structure during cycling, although the characteristic (002) peak shifted by approximately 1° upon charging. This peak then diminished in prominence during the discharge cycle. This phenomenon is attributed to the reversible intercalation and deintercalation of Zn^{2+}, which affects the intensity of the XRD peaks.[43] Similar to previous reported AZIBs research, the formation of $Zn_4SO_4(OH)_6\cdot xH_2O$ (ZHS, where x = 4 or 5) was observed during the discharge phase, marked by the disappearance of this compound's deposition peaks during charging, as shown in Figure 4.7a.[28] This observation highlights the reversible nature of cation intercalation in the NCMO cathodes.[44] During the discharge process, both H^+ and Zn^{2+} migrate towards the cathode, contributing to the formation of ZHS.

Conversely, during charging, these ions are removed from the cathode, leading to the breakdown of ZHS. The chemical reaction governing the formation and dissolution of ZHS is crucial for understanding the charge storage mechanism in these batteries and is outlined in Equation (4.2).[45]

$$12OH^- + 2SO_4^{2-} + 8Zn^{2+} + 2xH_2O \rightleftharpoons 2Zn_4(OH)_6SO_4 \cdot xH_2O \tag{4.2}$$

During the discharge phase from 1.9 V down to 0.8 V, the formation of ZHS on the cathode increases, a phenomenon that aligns with findings reported in other studies. Throughout the charge and discharge cycles, two distinct phases of ZHS are typically observed: $Zn_4SO_4(OH)_6{\cdot}4H_2O$ and $Zn_4SO_4(OH)_6{\cdot}5H_2O$. In the cycling process of the NCMO cathode, as depicted in Figure 4.7a, the ZHS predominantly forms as $Zn_4SO_4(OH)_6{\cdot}5H_2O$ during the initial full discharge. As the potential varies, the phase transitions to $Zn_4SO_4(OH)_6{\cdot}4H_2O$, reflecting consistency with previously published literature.[46-48] These observations demonstrate that the cycling behavior of the NCMO cathode adheres to the typical patterns seen in manganese-based cathodes, and importantly, the intercalation of Cu does not markedly influence the formation of different ZHS phases. Additionally, during the initial cycles, a notable improvement in the Mn-OH peak was observed. This enhancement is directly related to the proton (H^+) intercalation and deintercalation within the MnO_2-based cathode, as detailed in Equation (4.3).[45]

$$MnO_2 + H^+ + e^- \rightleftharpoons MnOOH \tag{4.3}$$

As the number of cycles increases, the poor reversibility of ZHS leads to its accumulation on the surface of the cathode material in the NMO cathode. This phenomenon occurs after extensive cycling, specifically 100 cycles at a current density of 1 A g^{-1}. Consequently, this accumulation enhances the visibility of ZHS peaks in the electrochemical spectra, even when the battery is fully charged. Conversely, in full cell configurations using an NCMO cathode, ZHS demonstrates significantly better reversibility. After 100 cycles at the fully charged state, ZHS peaks are virtually undetectable, suggesting minimal accumulation. However, robust ZHS peaks are still apparent in the fully discharged state, indicating effective reversibility of ZHS within the NCMO cathode system. This contrast underscores the importance of cathode material choice in influencing the reversibility and stability of battery components during cycling.

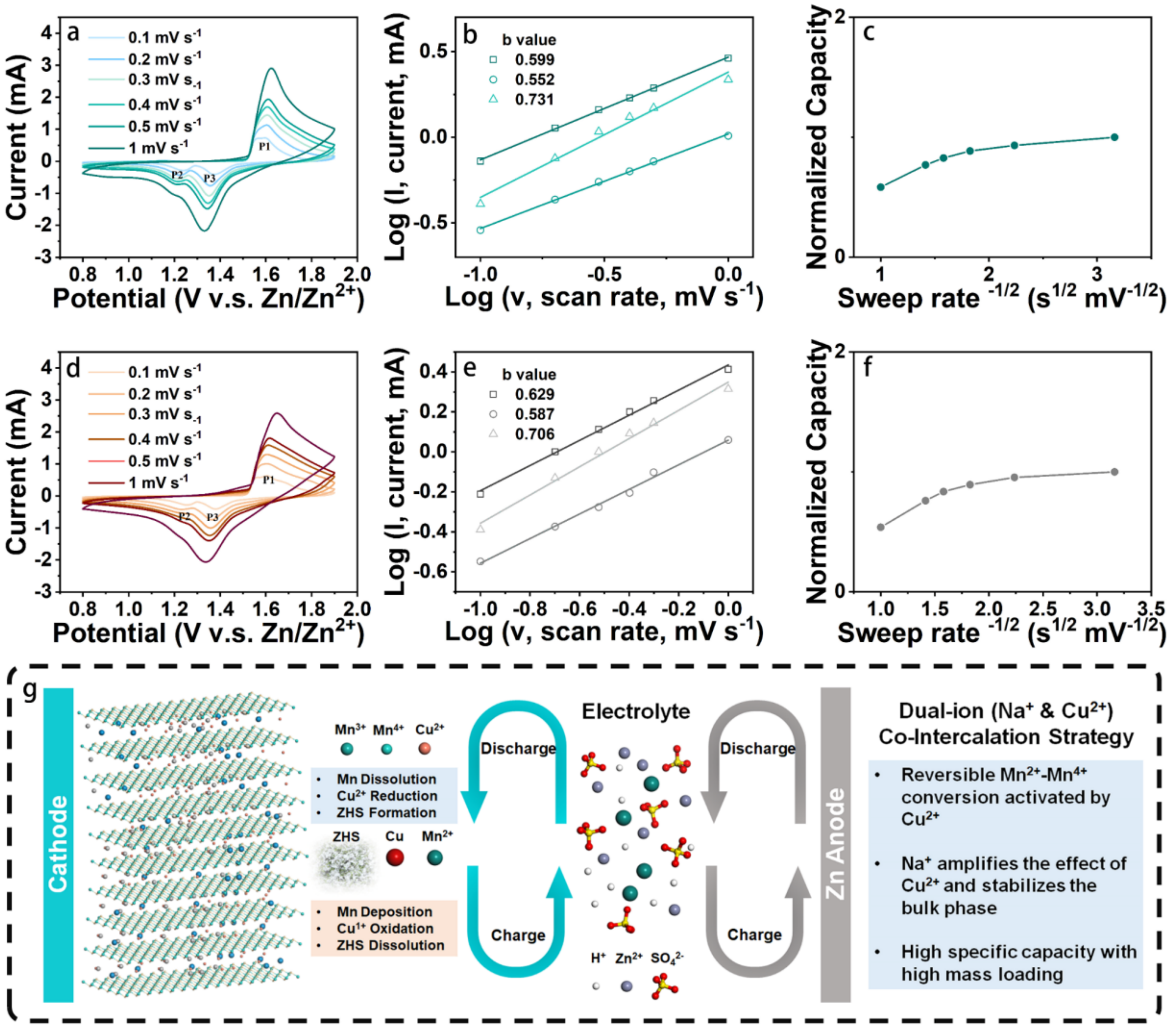

Figure 4.6 (a, d) CV curves with scan rates ranging from 0.1 to 1 mV s^{-1}, (b, e) diffusion-capacitive control contribution, and (c, f) the relationship between normalized capacity and sweep rate of NCMO and NMO, respectively. (g) Schematic diagram illustrating the charge and discharge process of NCMO cathodes in AZIBs.

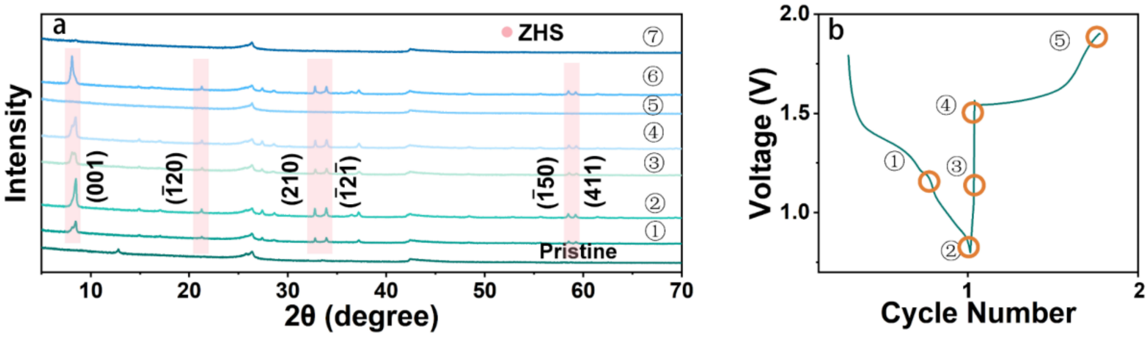

Figure 4.7 (a) *Ex-situ* XRD spectra of the NCMO cathode in the full cell at different potentials marked in (b) during the initial cycle (1-5), and the fully discharged (6) and fully charged (7) states after 50 cycles.

In Figures 4.8a-f, the XPS spectra provided insights into the evolution of the valence states of Mn and Cu in the NCMO structure. High-resolution XPS spectra comparisons of Mn 2p at fully discharged and fully charged states are depicted in Figures S6a and b. Notably, there was a significant increase in the proportion of Mn^{4+} during the charging process. The average valence state of Mn at both the fully charged and discharged states was quantified by the energy difference (ΔE) between two Mn 3s peaks, as shown in Figures 4.8c and d. The results indicated average valences of 3.43 in the fully charged state and 2.77 in the fully discharged state, respectively. The cycling behavior of the cathode was further examined through changes in the satellite peaks of Cu^{2+}, as evidenced in Figures 4.8e and f. These peaks, indicative of Cu^{2+} states, disappeared during discharge and re-emerged upon recharging to 1.90 V, suggesting the reduction and subsequent reoxidation of Cu^{2+}.[49]

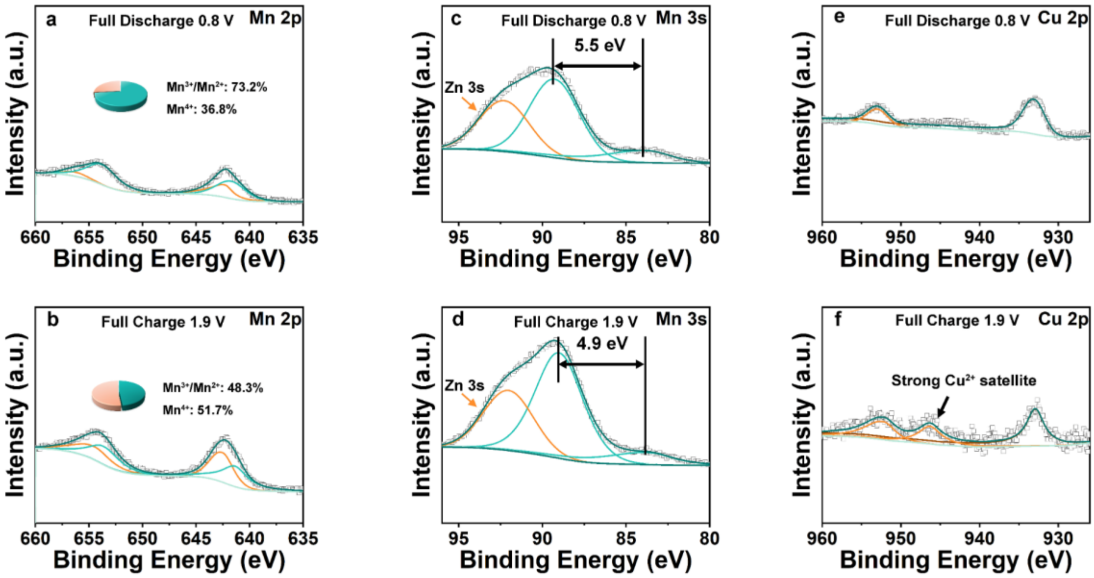

Figure 4.8 Changes in the valence states of Mn and Cu elements during charge and discharge are determined by high resolution *ex-situ* XPS spectra of (a, b) Mn 2p, (c, d) Mn 3s, and (e, f) Cu 2p in full discharge and full charge, respectively.

Throughout the cycling process of typical MnO_2-based AZIBs, Mn^{2+} from the electrolyte plays a crucial role by participating in the cycle of ZHS and contributing to the formation of birnessite-type MnO_2. This process involves the joint interaction of H^+, Zn^{2+}, Mn^{2+}, and ZHS within the cycling system. The addition of Cu to the system enhances the intercalation of both H^+ and Zn^{2+}, as evidenced by the data presented in Figures 4.9a and b. Initially, the NCMO cathode, which incorporates Cu, shows a higher capacity for proton batteries in the electrochemical process without Zn^{2+}, though maintaining this performance over multiple cycles proves challenging. However, the introduction of Zn^{2+} into the system significantly stabilizes and prolongs the activation process of NCMO. The dual-ion intercalation strategy, as illustrated in Figure 4.6g, leverages the role of Cu to enhance the intercalation of protons and Zn^{2+}. This effect is further amplified with the co-intercalation of Na^+. Cu^{2+} also potentially boosts ZHS reversibility within the cycling system. Conversely, in the NMO cathode, the birnessite phase's wide interplanar spacing facilitates Zn^{2+} intercalation; concurrently, the ZHS generated on the surface from proton intercalation contributes significantly to electron transfer, thus providing much of the battery's capacity. However, the poor reversibility of ZHS and its by-products gradually cover the active material over cycles, diminishing the capacity derived from ion intercalation. Despite these challenges, the presence of Mn^{2+} in the electrolyte allows for the deposition of the birnessite structure, which in turn offers additional surfaces for ZHS deposition, establishing a dynamic balance in terms of capacity performance. Over time, the formation of more irreversible Zn_xMnO_2 on the surface and the depletion of Mn^{2+} in the electrolyte lead to a sharp decline in specific capacity, critically limiting the lifespan of Mn-based AZIBs.

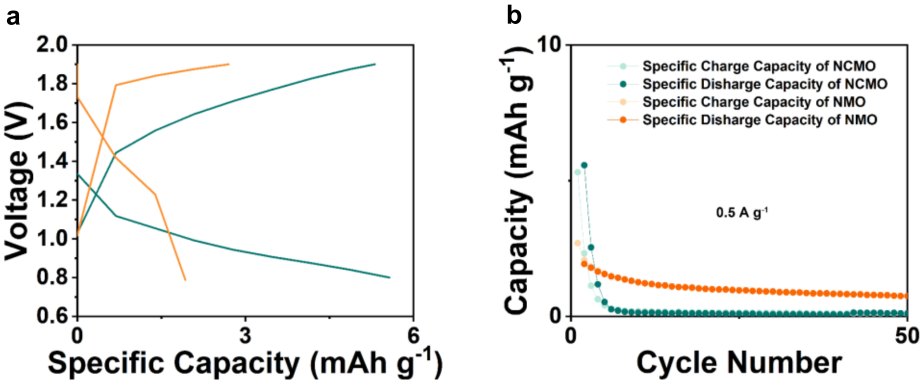

Figure 4.9 Galvanostatic charge and discharge profiles of 1st cycle for NMO and NCMO full cell in the electrolyte of 2 M H_2SO_4 electrolyte without Zn^{2+}. (b) Cycle performance of NCMO and NCMO cathodes at a current density of 0.5 A g^{-1} in 2 M H_2SO_4 electrolyte without Zn^{2+}.

The comparative electrochemical behavior of NCMO and NMO cathodes during cycling, particularly with and without the addition of Mn^{2+} to the electrolyte, is illustrated through Figures 4.10-4.13. In the initial cycle within a Mn^{2+}-free electrolyte, NCMO demonstrated higher activity and did not require an activation process, unlike NMO. A notable observation from the data is the difference in the potential during charge/discharge at half the reversible capacity, $\delta(V(Q/2))$, which at the 100th cycle is approximately 0.19 V for NCMO, significantly lower than the 0.25 V observed in NMO. This smaller potential difference in NCMO indicates lower hysteresis and superior kinetic performance compared to NMO. Furthermore, during the first cycle, NCMO exhibits a capacity that is attributed to the dissolution of active manganese, a phenomenon does not present in the initial stages of cycling for NMO. The activation process observed in NMO, especially in $MnSO_4$-free electrolyte, stems from the necessity to generate ZHS during the first cycle. However, when Mn^{2+} is present (originating from the dissolution of solid MnO_2), ZHS acts as a reaction that promotes a deposition reaction. This reaction leads to the formation of layered zinc vernadite ($Zn_xMnO(OH)_2$) nanosheets on the cathode surface during the charging process, which exhibit a plateau voltage of approximately 1.5 V vs Zn/Zn^{2+}. During the discharging phase, ZHS is reintegrated, facilitating the recombination process and simultaneously accelerating the proton interaction with $Zn_xMnO(OH)_2$, which results in the dissolution of the $Zn_xMnO(OH)_2$ nanosheets. This reversible conversion reaction between ZHS and $Zn_xMnO(OH)_2$ underpins the reversible energy storage reactions in aqueous Mn-based AZIBs, showcasing a dynamic interplay that enhances the battery's cycling efficiency and energy output. Thus, the electrochemical cycling of NCMO and NMO highlights fundamental differences in their performance and mechanisms, influenced significantly by the presence or absence of Mn^{2+} in the electrolyte.[50]

During the charge process:

$$Zn_4SO_4(OH)_6 \cdot xH_2O + Mn^{2+} \rightarrow Zn_yMnO(OH)_2 + xH^+ + SO_4^{2-} + 2e^- \quad (4.4)$$

During the discharge process:

$$Zn_yMnO(OH)_2 + 4H^+ + 2e^- \rightarrow Mn^{2+} + Zn^{2+} + 3H_2O \quad (4.5)$$

$$4Zn^{2+} + SO_4^{2-} + 6OH^- + xH_2O \rightarrow Zn_4SO_4(OH)_6 \cdot xH_2O \quad (4.6)$$

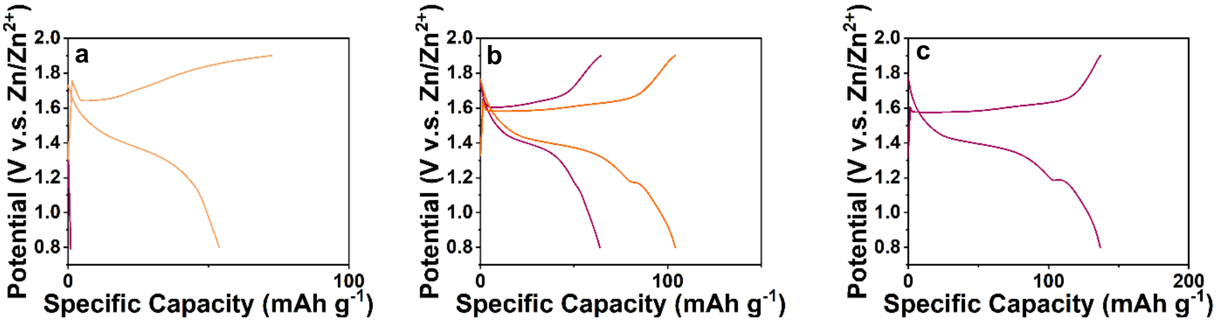

Figure 4.10 Galvanostatic charge and discharge profiles of (a) 1st, (b) 10th and 50th, and (c) 100th cycles for NMO full cell in the electrolyte of 2 M $ZnSO_4$.

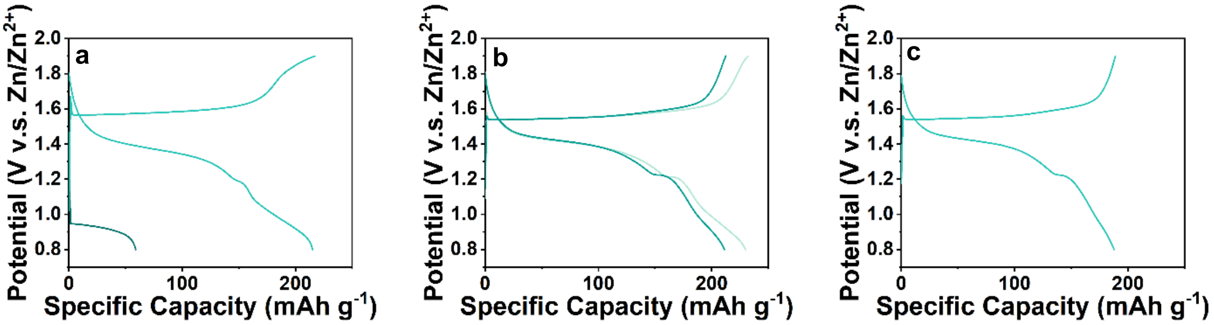

Figure 4.11 Galvanostatic charge and discharge profiles of (a) 1st, (b) 10th and 50th, and (c) 100th cycles for NCMO full cell in the electrolyte of 2 M $ZnSO_4$.

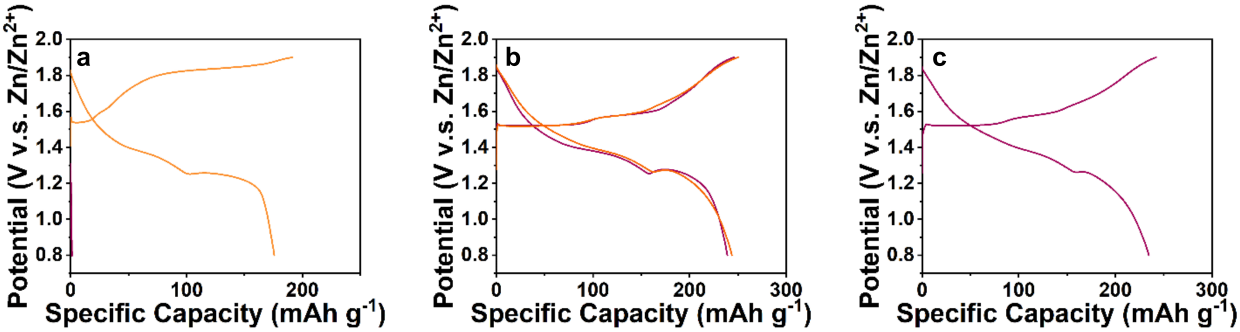

Figure 4.12 Galvanostatic charge and discharge profiles of (a) 1st, (b) 10th and 50th, and (c) 100th cycles for NMO full cell in the electrolyte of 2 M $ZnSO_4$ and 0.2 M $MnSO_4$.

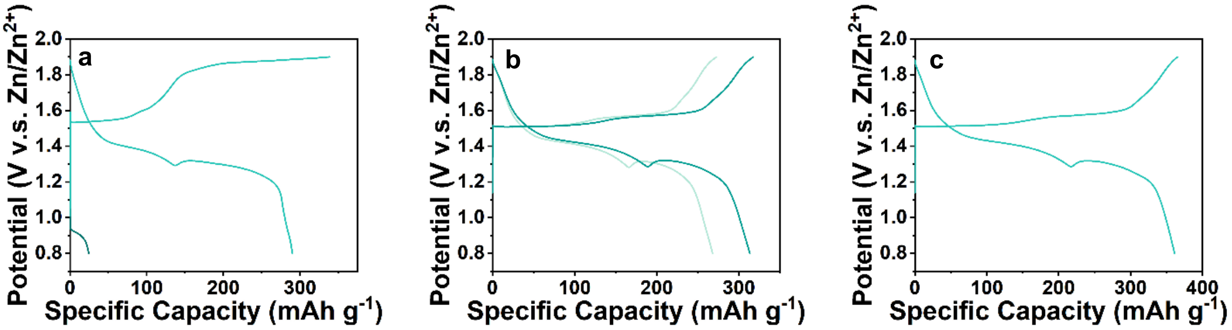

Figure 4.13 Galvanostatic charge and discharge profiles of (a) 1st, (b) 10th and 50th, and (c) 100th cycles for NCMO full cell in the electrolyte of 2 M $ZnSO_4$ and 0.2 M $MnSO_4$.

During the charging process of Mn-based materials, the generation of Cu^{2+} notably promotes the dissolution of $Zn_yMnO(OH)_2$, particularly evident in reactions such as those described in Equation (4.4), which accelerates the interaction between ZHS and Mn^{2+}. This is corroborated by the CV results shown in Figure 4.14b, where a scan rate of 0.3 mV s^{-1} revealed that $Cu^{(0)}$ oxidizes to Cu^{2+} with considerable reversibility, aligning with findings from XPS analyses. The Cu^{2+}, characterized by a d9 electron configuration, results in a degenerate set of d orbitals under symmetric conditions, rendering it susceptible to JT distortions. When Cu^{2+} and $Zn_yMnO(OH)_2$ are simultaneously generated, the JT effect facilitates the distortion of the $[MnO_6]$ octahedral structure, thereby enhancing the dissolution of $Zn_yMnO(OH)_2$ and enabling two-electron transfer processes on the surface.[51] In contrast, the addition of Na^+ aids in maintaining the stability of the bulk structure throughout the cycling process. The NMO cathode, given its unique birnessite structure, allows for the intercalation of protons and Zn^{2+} during discharge, providing initial capacity.[3, 52] In electrolytes containing Mn^{2+}, the NCMO cathode displays enhanced reversibility and an increment in cycle capacity. Remarkably, the voltage plateau of NCMO at approximately 1.2 V vs Zn/Zn^{2+} remains distinct even after 100 cycles, showcasing the highly reversible nature of Mn deposition reactions. However, for the NMO cathode, the clarity of the Mn cycling plateau diminishes after 100 cycles, illustrating an improvement in the reversibility of Cu in Mn deposition and dissolution. SEM and EDS mapping of the NCMO cathode post-100 cycles at a current density of 0.1 A g^{-1}, depicted in Figure 4.15, confirm the structural stability of NCMO as a host material, with the cathode maintaining its morphology akin to its initial state without significant structural degradation.

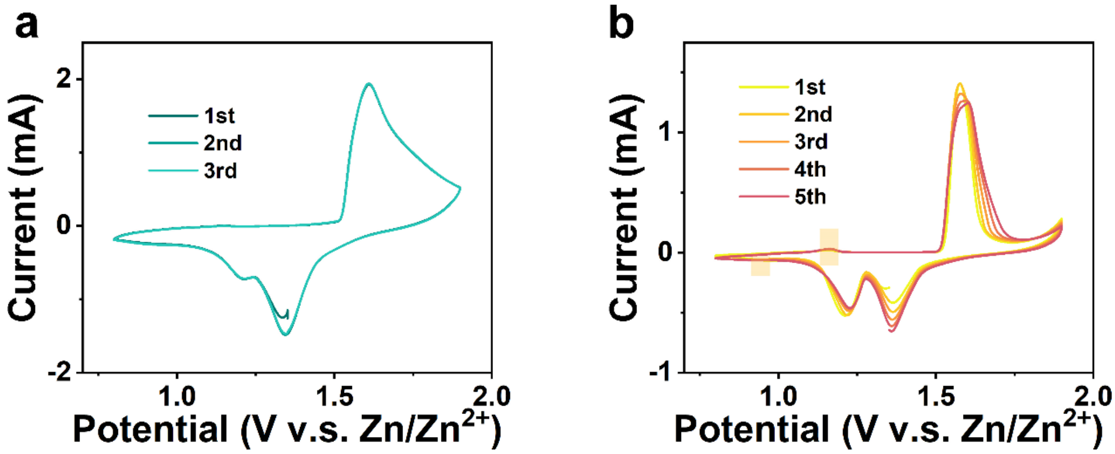

Figure 4.14 CV curves for the (a) first three cycles at a scan rate of 0.5 mV s^{-1} after activation and (b) first five cycles at a scan rate of 0.3 mV s^{-1} after activation of NCMO full cell.

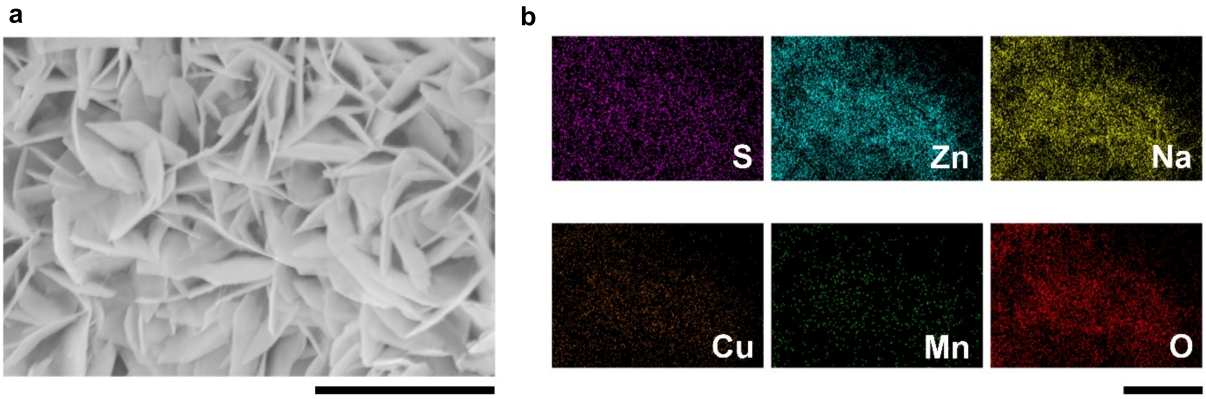

Figure 4.15 (a) SEM and (b) EDS mapping of NCMO cathode after 100 cycles at a current density of 0.1 mA g^{-1}, with scale bars of 5 μm.

The impact of Cu^{2+} on the ZHS cathode during the charge and discharge cycles in ZIBs was also investigated. Results shown in Figure 4.16a indicate that in the absence of Mn^{2+} in the electrolyte, the ZHS cathode yields negligible capacity. However, upon the addition of $MnSO_4$ (Figure 4.16b), ZHS initially provides nearly 200 mAh g^{-1} capacity, though this capacity decays after the first cycle without an activation process. This suggests that while ZHS participates in the Mn^{2+}/Mn^{4+} conversion process, the insufficient reversibility of this mechanism limits stable cycling. When an electrolyte containing 0.1M $CuSO_4$ (alongside 2M $ZnSO_4$ and 0.2M $MnSO_4$) is introduced, the ZHS cathode initially delivers extraordinary capacities exceeding 330 mAh g^{-1} over the first 7 cycles with a slight activation process evident in Figure 4.16c, highlighting Cu's promotive effect on the Mn deposition and dissolution dynamics within the ZHS cathode. Despite these initial gains, the capacity rapidly declines post the 7th cycle due to the instability of ZHS as a host material, affirming that Cu enhances the Mn^{2+}/Mn^{4+} conversion process integral to ZHS functionality.

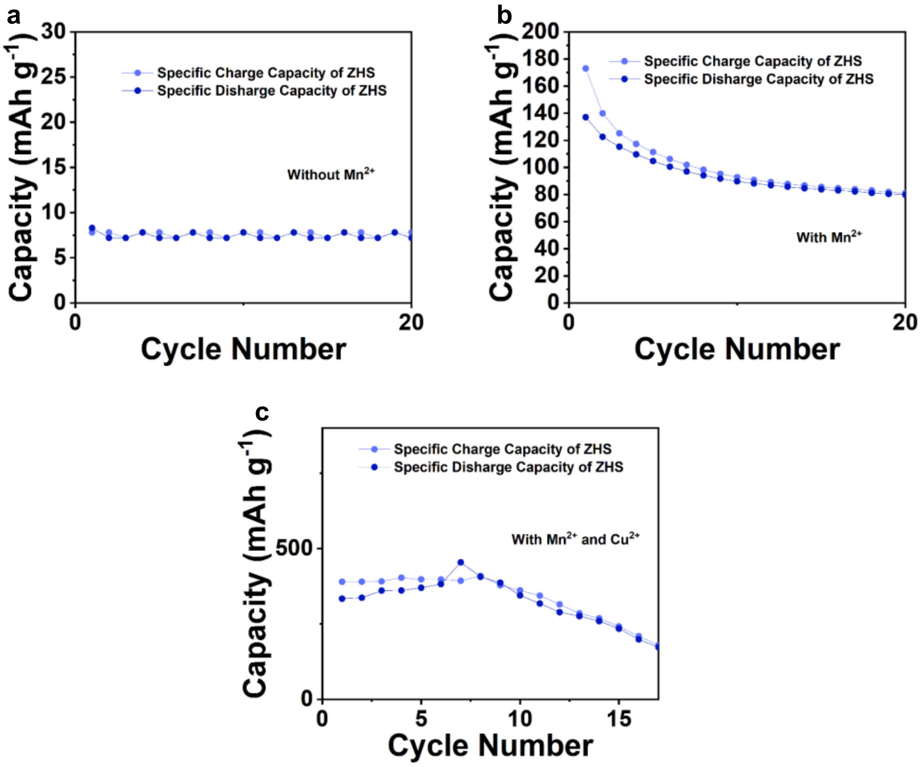

Figure 4.16 (a) Cycle performance of ZHS at a current density from 0.1 A g^{-1} in the electrolyte of 2 M $ZnSO_4$. (b) Cycle performance of ZHS at a current density from 0.1 A g^{-1} in the electrolyte of 2 M $ZnSO_4$ and 0.2 M $MnSO_4$. (c) Cycle performance of ZHS at a current density from 0.1 A g^{-1} in the electrolyte of 2 M $ZnSO_4$, 0.2 M $MnSO_4$ and 0.1M $CuSO_4$.

The rate performances of the NCMO and NMO were evaluated across a spectrum of current densities with 0.2-10 A g^{-1} in Figure 4.17a. With increasing current densities, a decline in the specific capacities of both electrodes was observed, a phenomenon attributed to the constraints in electrochemical reaction kinetics. Nonetheless, the Zn//NCMO battery showcased superior rate capability, achieving high capacities at varying currents: 364 mAh g^{-1} at 0.2 A g^{-1}, 290 mAh g^{-1} at 0.5 A g^{-1}, 247 mAh g^{-1} at 1 A g^{-1}, 196 mAh g^{-1} at 2 A g^{-1}, 125 mAh g^{-1} at 5 A g^{-1}, and 85 mAh g^{-1} at 10 A g^{-1}. Remarkably, the capacities of the NCMO electrode were about 1.5 times higher than those of the NMO electrode at comparable current densities. Furthermore, the excellent rate cyclability of the NCMO electrode was underscored by its ability to recover a reversible capacity of approximately 365 mAh g^{-1} at 0.2 A g^{-1} without any noticeable degradation. The galvanostatic discharge/charge curves of the NCMO electrode, illustrated in Figure 4.17b, revealed distinct charge/discharge plateaus at various current densities, confirming its enhanced rate performance. This improvement is likely due to better electron transport and ion diffusion kinetics, enhanced by the co-intercalation of Na^+ and Cu^{2+} into the NMO structure. However, both NMO and NCMO showed self-discharge after full charge, and their voltage slowly decreased from 1.9 V to 1.7 V within 10 mins. *Ex-situ* SEM images provided evidence of the underlying charge storage mechanism and morphological stability of the NCMO cathode throughout the cycling. The flake-like morphology was consistently preserved, suggesting a robust host structure. Complementary *ex-situ* XRD, XPS, and SEM analyses confirmed the reversible formation and dissolution of ZHS, the stability of the NCMO structure, and the efficient valence conversion of Mn during cycling, as mentioned in previous experimental results. Moreover, as shown in Figure 4.14a, after an initial activation using a low current, the Zn//NCMO full cell was tested for CV at a scan rate of 0.5 mV s^{-1}. The resulting CV curve demonstrated a high degree of consistency, indicative of stable and highly reversible cycling performance.

To assess the cycling stability of the synthesized materials, low-rate cycling tests were conducted at a current density of 0.5 A g^{-1} for both NCMO and NMO electrodes. As illustrated in Figure 4.17c, the NCMO cathode, with an active material mass loading of approximately 1 mg cm^{-2}, demonstrated a gradual and consistent increase in specific capacity over time. Remarkably, after 100 cycles, it achieved a discharge capacity of 576 mAh g^{-1}, nearly tripling the performance of the NMO cathode. This significant increase in capacity correlates with the progressive deposition of Mn-based materials onto the cathode, facilitated by the Mn^{2+}-enriched electrolyte. It is worth noting that when Cu was introduced, the activation process seemed to be longer and exhibited a surprisingly high reversible specific capacity after long-term cycle.

Figure 4.17d demonstrates the high-rate and long-term cycling performance of the NCMO cathode, tested at a current density of 2 A g^{-1}. At this rate, AZIBs equipped with NCMO cathodes exhibited exceptional durability, maintaining ~100% capacity retention over 1000 cycles and achieving a specific capacity of 200 mAh g^{-1}, which is 3.33 times higher than that of NMO cathodes, which only retained about 82% capacity. This outstanding performance prompted further testing to assess the industrial viability of NCMO under high-loading conditions. An NCMO cathode with a moderate active material loading of approximately 7.5 mg cm^{-2} was crafted to investigate the regulation of Mn deposition and dissolution in more demanding scenarios. Displayed in Figure 4.17e, at a reduced current density of 0.1 A g^{-1} (equivalent to 0.75 mA cm^{-2}), this cathode delivered a specific capacity of 1.36 mAh cm^{-2} (181 mAh g^{-1}) and showed nearly 90% capacity retention after 100 cycles. When the active material loading was increased to about 10.9 mg cm^{-2}, the electrode demonstrated stable electrochemical reactions, as evidenced in Figure 4.17f. After 50 cycles, the voltage plateau of the full cell remained stable, with a capacity retention rate of 81%. Figure 4.17g shows that, in its initial cycle, the NCMO cathode with high active material loading delivered a high specific capacity of 2.60 mAh cm^{-2} (239 mAh g^{-1}) and maintained a reversible capacity of 2.10 mAh cm^{-2} (193 mAh g^{-1}) after 50 stable cycles at a current density of 1.09 mA cm^{-2} (0.1 A g^{-1}). This suggests that strategies aimed at enhancing both surface reactivity and bulk stability of the cathode material are critical. The introduction of Cu^{2+} promotes efficient two-electron transfer of Mn^{2+}/Mn^{4+} on the surface, while Na^{+} contributes to the bulk stability, leading to smoother cycling as cathode mass loading increases. Interestingly, despite a lower specific capacity at higher mass loadings due to a reduced surface ratio, the NCMO cathodes still demonstrate robust performance, attributed to their stable bulk structure and enhanced surface reactivity. Figure 4.17h compares various cathodes' performances over the past three years with mass loadings ranging from 1 to 10.5 mg cm^{-2}, illustrating that the dual-ion pre-intercalation strategy employed in this work delivers superior operating capacity, recovery efficiency, and high specific capacity, setting a promising benchmark for future developments in manganese oxide cathodes for aqueous AZIBs.[16, 53-58]

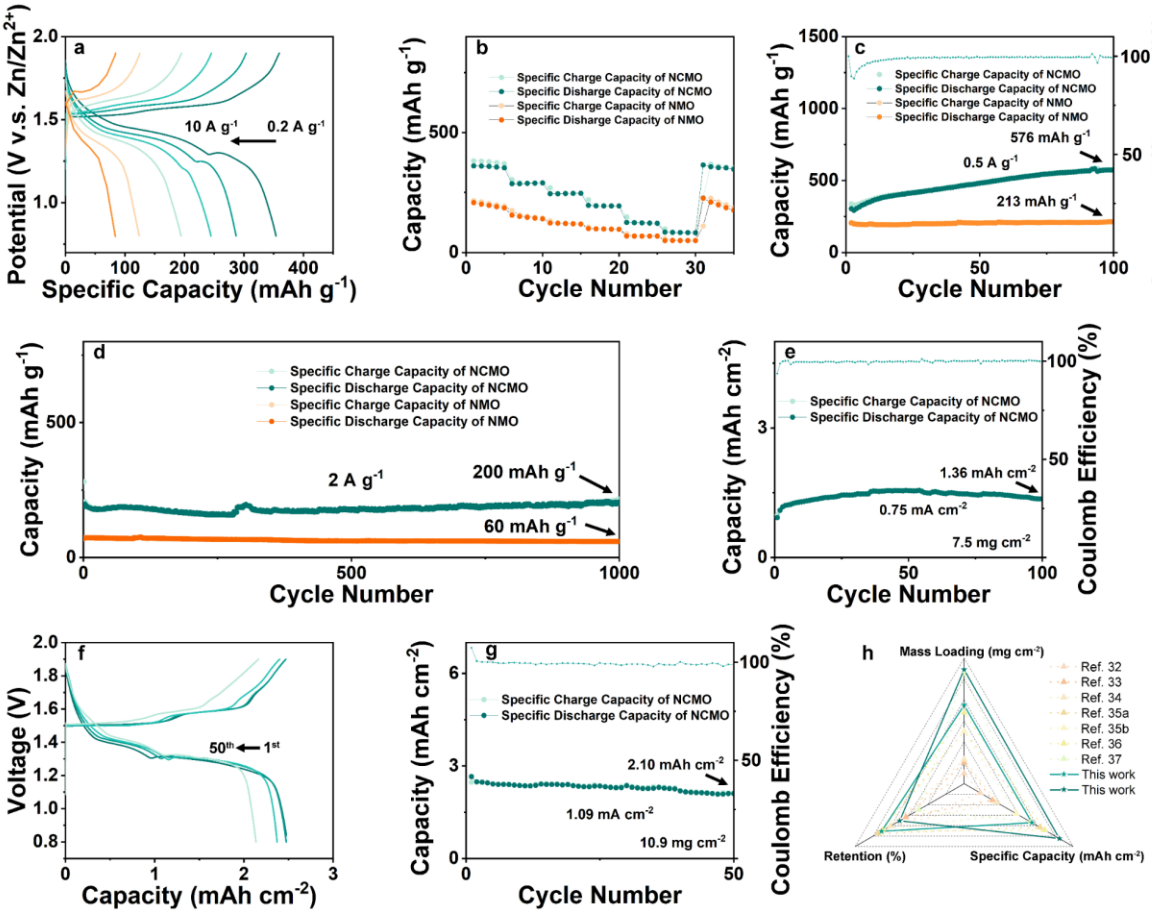

Figure 4.17 (a) Galvanostatic charge and discharge profiles for NCMO full cell and (b) cycle performance of NCMO compared with NMO at different current densities from 0.2 to 10 A g^{-1}. (c) Low-rate cycle performance of NCMO and NMO at a current density of 0.5 A g^{-1}, which shows that the NCMO can exhibit a reversible specific capacity of 576 mAh g^{-1} after 100 cycles. (d) Long-term cycle performance of NCMO and NMO cathode at a current density of 2 A g^{-1}, which shows that the NCMO can exhibit a reversible specific capacity of 200 mAh g^{-1} after 1,000 cycles. (e) Low-rate cycle performance of NCMO with a high active material mass loading of 7.5 mg cm^{-2} at a current density of 0.1 A g^{-1} (i.e., 0.75 mA cm^{-2}), which shows that the NCMO exhibits a reversible specific capacity of 1.36 mAh cm^{-2} (181 mAh g^{-1}) after 100 cycles. (f) Galvanostatic charge and discharge profiles for NCMO full cell with a cathode active material mass loading of 10.9 mg cm^{-2} and the corresponding (g) low-rate cycling

performance of NCMO cathodes at a current density of 0.1 A g^{-1} (i.e., 1.09 mA cm^{-2}), which shows that the NCMO exhibits a reversible specific capacity of 2.10 mAh cm^{-2} (193 mAh g^{-1}) after 50 cycles. (h) Radar chart comparing the performance of this work with recent MnO_2-based cathode work from the three dimensions of mass-loading, retention, and specific capacity.

4.5 Summary

In summary, the co-intercalation of Na^+ and Cu^{2+} into birnessite manganese oxide cathodes was proven to be a highly effective strategy for boosting the electrochemical performance of AZIBs. This technique enhances the electrochemical reactivity by amplifying the activation effect of Cu^{2+} on the Mn^{2+}/Mn^{4+} redox pair at the surface, while Na^+ contributes to stabilizing the host structure during charge and discharge cycles. This dual intercalation approach results in improved specific capacity and cycling stability, supporting prolonged capacity increases at low mass loadings and facilitating a highly reversible process of manganese deposition and dissolution at higher mass loadings. The method for achieving high mass loading in this research leverages a straightforward and well-established electrode coating process, which is both cost-effective and scalable. The NCMO cathode demonstrates exceptional specific capacity and cycling stability across a range of mass loadings, and it notably approaches the theoretical capacity for Mn^{2+}/Mn^{4+} two-electron transfer, positioning it among the most promising in recent studies of AZIBs. This work not only showcases the highest mass loading stable cycling observed in such studies but also underscores its potential for practical and efficient energy storage solutions. The mechanisms by which Cu^{2+} promotes the deposition and dissolution of Mn in the cathode during cycling are also explored, highlighting the integral role of Cu^{2+} in enhancing the performance. The findings of this study advocate for a strategy that simultaneously promotes surface two-electron transfer and maintains the stability of the host material, presenting a compelling approach for the development of advanced cathode materials for high-performance AZIBs.

4.6 References

[1] L. Meng, Y. Zhu, Y. Lu, T. Liang, L. Zhou, J. Fan, Y.C. Kuo, P. Guan, T. Wan, L. Hu, *ChemElectroChem*, **11** (2024) e202300495.

[2] W. Li, Q. Song, Q. Dong, J. Zhang, J. Wang, Y. Wu, Y. Yu, X. Li, *Adv. Mater.*, (2024) 2414019.

[3] Z. Shang, S. Wang, H. Zhang, W. Zhang, S. Lu, K. Lu, *Nanoscale*, **14** (2022) 14433-14454.

[4] S. Wei, Y. Wang, S. Chen, L. Song, *Chem. Sci.*, (2024).

[5] Z. Hou, J. Wang, N. Dai, S. Yao, S. Wang, Y. Ji, X. Gao, H. Zhang, Z. Tang, Y. Sun, *Adv. Energy Mater.*, **14** (2024) 2302477.

[6] A. Sacchetti, (2005).

[7] T. Shang, A. Gao, D. Xiao, Q. Zhang, X. Rong, Z. Tang, W. Lin, T. Lin, F. Meng, X. Li, *Natl. Sci. Rev.*, **11** (2024) nwae255.

[8] T.N.T. Tran, S. Jin, M. Cuisinier, B.D. Adams, D.G. Ivey, *Scientific Reports*, **11** (2021) 20777.

[9] S.W. Gourley, R. Brown, B.D. Adams, D. Higgins, *Joule*, **7** (2023) 1415-1436.

[10] Y. Hu, P. Wang, M. Li, Z. Liu, S. Liang, G. Fang, *Energy Environ. Sci.*, (2024).

[11] W. Du, E.H. Ang, Y. Yang, Y. Zhang, M. Ye, C.C. Li, *Energy Environ. Sci.*, **13** (2020) 3330-3360.

[12] X. Wang, Z. Zhang, B. Xi, W. Chen, Y. Jia, J. Feng, S. Xiong, *ACS Nano*, **15** (2021) 9244-9272.

[13] W. Shi, W.S.V. Lee, J. Xue, *ChemSusChem*, **14** (2021) 1634-1658.

[14] B. Yong, D. Ma, Y. Wang, H. Mi, C. He, P. Zhang, *Adv. Energy Mater.*, **10** (2020) 2002354.

[15] B. Zhang, J. Chen, W. Sun, Y. Shao, L. Zhang, K. Zhao, *Energies*, **15** (2022) 4698.

[16] Y. Zhao, P. Zhang, J. Liang, X. Xia, L. Ren, L. Song, W. Liu, X. Sun, *Energy Stor. Mater.*, **47** (2022) 424-433.

[17] X. Wang, Y. Wang, A. Naveed, G. Li, H. Zhang, Y. Zhou, A. Dou, M. Su, Y. Liu, R. Guo, *Adv. Funct. Mater.*, **33** (2023) 2306205.

[18] X. Zhao, L. Mao, Q. Cheng, F. Liao, G. Yang, X. Lu, L. Chen, *Energy Stor. Mater.*, **38** (2021) 397-437.

[19] I.R. Tay, J. Xue, W.S.V. Lee, *Adv. Sci.*, **10** (2023) 2303211.

[20] J. Huang, J. Zhou, S. Liang, *Acta Phys. Chim. Sin*, **37** (2021) 2005020.

[21] X. Zhang, J. Li, H. Ao, D. Liu, L. Shi, C. Wang, Y. Zhu, Y. Qian, *Energy Stor. Mater.*, **30** (2020) 337-345.

[22] Z. Deng, J. Huang, J. Liu, L. Ren, L. Zhu, X. Xiao, M. Tan, *Materials Letters*, **248** (2019) 207-210.

[23] S. Zeng, Y. Song, X. Shi, W. Xu, D. Zheng, F. Wang, C. Xu, X. Lu, *Journal of Alloys and Compounds*, **913** (2022) 165207.

[24] M. Li, C. Liu, J. Meng, P. Hei, Y. Sai, W. Li, J. Wang, W. Cui, Y. Song, X.X. Liu, *Adv. Funct. Mater.*, (2024) 2405659.

[25] H. Li, Z. Huang, B. Chen, Y. Jiang, C. Li, W. Xiao, X. Yan, *J. Power Sources*, **527** (2022) 231198.

[26] L. Dai, Y. Wang, L. Sun, Y. Ding, Y. Yao, L. Yao, N.E. Drewett, W. Zhang, J. Tang, W. Zheng, *Adv. Sci.*, **8** (2021) 2004995.

[27] X. Xie, H. Fu, Y. Fang, B. Lu, J. Zhou, S. Liang, *Adv. Energy Mater.*, **12** (2022) 2102393.

[28] X. Zeng, J. Liu, J. Mao, J. Hao, Z. Wang, S. Zhou, C.D. Ling, Z. Guo, *Adv. Energy Mater.*, **10** (2020) 1904163.

[29] R. Zhang, P. Liang, H. Yang, H. Min, M. Niu, S. Jin, Y. Jiang, Z. Pan, J. Yan, X. Shen, *J. Chem. Eng.*, **433** (2022) 133687.

[30] G. Kresse, J. Furthmüller, *Phys. Rev. B*, **54** (1996) 11169.

[31] P.E. Blöchl, *Phys. Rev. B*, **50** (1994) 17953.

[32] G. Kresse, D. Joubert, *Phys. Rev. B*, **59** (1999) 1758.

[33] J.P. Perdew, K. Burke, M. Ernzerhof, *Phys. Rev. Lett.*, **77** (1996) 3865.

[34] S.L. Dudarev, G.A. Botton, S.Y. Savrasov, C. Humphreys, A.P. Sutton, *Phys. Rev. B*, **57** (1998) 1505.

[35] P.E. Blöchl, O. Jepsen, O.K. Andersen, *Phys. Rev. B*, **49** (1994) 16223.

[36] Y. Noda, K. Ohno, S. Nakamura, *Phys. Chem. Chem. Phys.*, **18** (2016) 13294-13303.

[37] H. Dong, J. Li, S. Zhao, Y. Jiao, J. Chen, Y. Tan, D.J. Brett, G. He, I.P. Parkin, *ACS Appl. Mater. Interfaces*, **13** (2020) 745-754.

[38] H. Kawaoka, M. Hibino, H. Zhou, I. Honma, *ECS Solid State Lett.*, **8** (2005) A253.

[39] X. Gao, C. Zhang, Y. Dai, S. Zhao, X. Hu, F. Zhao, W. Zhang, R. Chen, W. Zong, Z. Du, *Small Structures*, **4** (2022) 2200316.

[40] X. Yin, Y. Li, W. Cai, C. Fan, W. Liu, N. Wang, G. Qin, Z. Xie, X. Chen, Y. Han,

Appl. Surf. Sci., **624** (2023) 157124.

[41] V. Srinivasan, J.W. Weidner, *J. Power Sources*, **108** (2002) 15-20.

[42] P. Daubinger, J. Kieninger, T. Unmüssig, G.A. Urban, *Phys. Chem. Chem. Phys.*, **16** (2014) 8392-8399.

[43] A. Moezzi, M.B. Cortie, A.M. McDonagh, *Dalton Trans.*, **42** (2013) 14432-14437.

[44] L. Godeffroy, I. Aguilar, J. Médard, D. Larcher, J.M. Tarascon, F. Kanoufi, *Adv. Energy Mater.*, **12** (2022) 2200722.

[45] X. Gao, Y. Dai, C. Zhang, Y. Zhang, W. Zong, W. Zhang, R. Chen, J. Zhu, X. Hu, M. Wang, *Angew. Chem., Int. Ed.*, **62** (2023) e202300608.

[46] J. Wang, B. Zhang, Z. Cai, R. Zhan, W. Wang, L. Fu, M. Wan, R. Xiao, Y. Ou, L. Wang, *Sci. Bull.*, **67** (2022) 716-724.

[47] I. Aguilar, P. Lemaire, N. Ayouni, E. Bendadesse, A.V. Morozov, O. Sel, V. Balland, B. Limoges, A.M. Abakumov, E. Raymundo-Piñero, *Energy Stor. Mater.*, **53** (2022) 238-253.

[48] D. Wu, L.M. Housel, S.T. King, Z.R. Mansley, N. Sadique, Y. Zhu, L. Ma, S.N. Ehrlich, H. Zhong, E.S. Takeuchi, *J. Am. Chem. Soc.*, **144** (2022) 23405–23420.

[49] Y. Chen, S. Gu, S. Wu, X. Ma, I. Hussain, Z. Sun, Z. Lu, K. Zhang, *J. Chem. Eng.*, **450** (2022) 137923.

[50] H. Chen, C. Dai, F. Xiao, Q. Yang, S. Cai, M. Xu, H.J. Fan, S.J. Bao, *Adv. Mater.*, **34** (2022) 2109092.

[51] X. Xia, Y. Zhao, Y. Zhao, M. Xu, W. Liu, X. Sun, *Nano Research*, **16** (2023) 2511-2518.

[52] M. Huang, X. Wang, X. Liu, L. Mai, *Adv. Mater.*, **34** (2022) 2105611.

[53] S. Luo, J. Xu, B. Yuan, L. Chen, L. Xu, R. Zheng, Y. Wang, M. Zhang, Y. Lu, Y. Luo, *Carbon*, **214** (2023) 118334.

[54] C. Wang, Y. Zeng, X. Xiao, S. Wu, G. Zhong, K. Xu, Z. Wei, W. Su, X. Lu, *J. Energy Chem.*, **43** (2020) 182-187.

[55] Y. Zhang, S. Deng, Y. Li, B. Liu, G. Pan, Q. Liu, X. Wang, X. Xia, J. Tu, *Energy Stor. Mater.*, **29** (2020) 52-59.

[56] X. Gao, C. Zhang, Y. Dai, S. Zhao, X. Hu, F. Zhao, W. Zhang, R. Chen, W. Zong, Z. Du, *Small Structures*, **4** (2023) 2200316.

[57] Y. Zhao, R. Zhou, Z. Song, X. Zhang, T. Zhang, A. Zhou, F. Wu, R. Chen, L. Li, *Angew. Chem., Int. Ed.*, **61** (2022) e202212231.

[58] L. Wu, Y. Mei, Y. Liu, W. Xu, M. Zhang, Y. Dong, Z.-S. Wu, *J. Chem. Eng.*, **459** (2023) 141662.

Chapter 5 Break the trilemma: enhanced surface-to-bulk proton transfer to unlock the potential scale-up for aqueous batteries

5.1 Introduction

To achieve carbon neutrality, the global share of renewable energy is projected to rise from 14% in 2018 to approximately 74% by 2050, necessitating an eightfold annual increase.[1] The urgent need for sustainable energy solutions has intensified the focus on developing advanced battery technologies, especially as the world shifts from fossil fuels to renewable but meanwhile intermittent energy sources.[2, 3] While LIBs have led the way in commercialization, their flammable electrolytes and the limited rate performance of $LiFePO_4$ (LFP) cathodes (typically 0.5-1 C) highlight the need for alternative stationary energy storage solutions.[4] Aqueous batteries are emerging as a promising candidate in the post-LIBs era due to their inherent safety, low cost, and environmental friendliness.[5] Among these, aqueous Zn-ion batteries (AZIBs) are gaining significant research interest because of their high energy density, high-rate performance, and established Zn metal recycling process.[6] Recent advancements in electrolyte formulations and electrode materials have significantly enhanced their cycle life and efficiency, bringing AZIBs closer to industrialization.[7] However, a major challenge in AZIBs is the mass production of cathodes that can be stable during repeated cycling. Achieving a uniform distribution of active materials, a smooth electrode surface, and avoiding obvious powder and particle agglomeration are crucial for economical electrode manufacture.[8] The thicker the cathode material slurry coated on the current collector, the higher its mass loading, which reduces the electrical and ionic conductivities and electrolyte wettability, seriously affecting the electrochemical performance, resulting in low specific capacity and insufficient cycle stability.[9] Additionally, when considering mass production, the whole energy-based manufacturing capacity of AZIBs production lines is limited by the low median voltage of the cathode. Cathodes that achieve high mass loading (manufacturing level), high specific energy (material-development level), and high stability (device-design level) represent a “trilemma” in the path to industrialization.[10]

From a material-level perspective, manganese dioxide (MnO_2) offers multiple benefits as a cathode material for AZIBs.[11] MnO_2 is an abundant and cost-effective material with a high theoretical capacity of 308 mAh g^{-1} via one-electron transfer. Serving as cathode materials, they exhibit relatively high voltage plateaus (~1.5 V vs. Zn/Zn^{2+}), impressive cycling stability, and robust high-rate capabilities.[12] Challenges include insufficient electrical conductivity and the dissolution of cathode materials under acidic conditions, which increases polarization and degrades cathode materials. Although material-level optimizations like ion pre-intercalation and efficient conductive networks have been implemented, the MnO_2 cathode's reaction mechanism remains debated, with recent studies indicating that proton intercalation significantly contributes to the high-rate performance in AZIBs. For practical AZIBs systems, further improvements and successful commercialization will depend on a thorough understanding of the underlying chemistry. Table 5.1 presents physicochemical properties of ions relevant to ion insertion chemistry in AZIBs. Enhancing proton storage from the surface to the bulk of the cathode material is an effective strategy for improving overall electrochemical performance and accelerating the use of high-loading cathode materials in practical applications. From a mass production perspective, improved proton storage is expected to enhance the power density of battery cells, thereby boosting the manufacturing capacity of the entire production line. Proton reactions generally exhibit smaller overpotentials, less microstructural change, and lower energy barriers compared to Zn^{2+}.[13] In aqueous environments, protons exist as hydronium ions (H_3O^+) rather than free H^+.[14] H_3O^+ further interacts with other water molecules to form Eigen and Zundel cations ($H_9O_4^+$ and $H_5O_2^+$, respectively).[15] During the discharge process, promoting the dehydration of H_3O^+ on the cathode surface facilitates their entry into the bulk of active materials. The Shannon radius of protons is particularly significant as its negative value suggests favorable O-H semi-covalent interactions and establishes a consistent trend for other ionic species in oxide-based solids.[16] Dehydration of H_3O^+ to form H^+ increases theoretical specific capacity and reduces phase transitions caused by intercalation/deintercalation during cycling, thereby extending the battery's lifespan.[17] To achieve deep intercalation of H^+ in practical high-loading cathodes, delicate modifications such as morphology regulation, phase engineering, and composite structure construction can be beneficial.[18] However, these modifications are often costly and challenging to implement on a large scale in the battery industry.

Table 5.1 Physicochemical Properties of the Insertion Cations Commonly Encountered in Zn-Ion Batteries (AZIBs) Electrodes

	Cationic Species		
	H^+	**H_3O^+**	**Zn^{2+}**
Common coordination number (C.N.)	1, 2	varies	4, 6
Shannon crystal radius (Å)	–0.24 (C.N. 1)	<1.38[a]	0.74 (C.N. 4)
charge density (e $Å^{-3}$)[b]	N/A	0.091	1.178
standard reduction potential, E^0 (V)	0.00	0.00	–0.76
theoretical specific capacity (mA h g^{-1})	26536	1409	820

[a] The configuration is not well-established. As an approximation, the kinetic radius of H_2O can be assumed (1.38 Å), with the fact that H coordination reduces the molar volume of H_2O.[19]

[b] Obtained from the Shannon crystal radius.

Previous research on Zn-based energy storage has been confined to lab-scale studies, with limited progress in overcoming the "trilemma" of high mass loading on the path to industrialization. Traditional approaches have largely focused on altering the phase of the cathode, modifying the separator, or incorporating conventional electrolyte additives. While these methods have yielded promising outcomes in laboratory settings, they fall short under high-loading conditions due to the intrinsic barriers of solid-state ion diffusion. Specifically, the challenge of efficient solid ion transport across inter-particle interfaces remains unresolved. Moreover, these strategies often fail to balance practicality and cost-effectiveness, limiting their scalability and commercial viability. To advance practical and commercially viable AZIBs to the market, it is essential to implement research innovations at an industrial scale, with the consideration of reducing manufacturing costs and maximizing production line capacity. Here, a LIBs production line was redesigned to adapt for aqueous battery production and economically introduced acetic acid (HAc) into the slurry mixing process to assist proton storage in high-loading cathodes, based on the 15-meter automated web coating machine and commercial electrolytic γ-MnO_2, as illustrated in Figure 5.1a. By introducing HAc in the slurry mixing process, the power-based manufacturing capacity (power capacity) of the production line was increased by 44.2% and achieved mass-produced 7.5-Ah AZIBs prototype. Our innovative strategy pivots away from these traditional methods, centering on a groundbreaking modification of the cathode mixing step. This approach enables uniform modifications across all particle surfaces and interfaces, ensuring consistent performance throughout the cathode material. Unlike conventional methods that focus solely on electrode-bulk level modifications or H^+ desolvation promotion, our strategy addresses both these aspects while extending to the single-particle level. This comprehensive modification ensures optimal H^+ desolvation, thereby enhancing the overall efficiency and functionality of the cathode according to our design specifications. By targeting the cathode at a granular level, not only the solid-state ion transport was improved but also the issues associated with high-loading conditions was mitigated. This strategy ensures that each particle within the cathode contributes effectively to the battery’s performance, overcoming the limitations of traditional methods. The uniform modification of particle-particle interfaces facilitates seamless ion transport, significantly boosting the battery's operational efficiency. This approach balances innovation with practicality and cost-effectiveness, making it a viable solution for large-scale applications. By addressing the core challenges of ion diffusion and interface transport, our strategy represents a significant advancement in AZIBs. This innovation not only enhances the battery's performance under high-loading conditions but also paves the way for more practical and commercially viable energy storage solutions.

5.2 Experimental Section

5.2.1 Chemicals

All chemicals were used as purchased without further purification. Poly(vinylidene fluoride), average Mw ~534,000, powder (Sigma-Aldrich); N-methyl-2-pyrrolidone (NMP), 99% (Sigma-Aldrich); MnO_2 99% (Vastech-Energy); $MnSO_4·1H_2O$ (≥99%) (Sigma-Aldrich); $ZnSO_4·7H_2O$ (≥99%) (Sigma-Aldrich).

5.2.2 High mass loading cathode manufacturing on production line

As shown in Figure 5.1a, in a 50 L planetary mixer, 5.5 kg of γ-type MnO_2 (active material), 1.2 kg of carbon black (Super P), and 25 L of deionized water were mixed, stirred with impeller at 35 rpm and dispersed with dispersion disc at 3500 rpm for 120 minutes. After the MnO_2 and Super P powders were dispersed, 350 g of Carboxymethylcellulose (CMC) powder was added and the mixture was stirred and dispersed with the same speed for 60 mins to ensure a homogeneous slurry without CMC powder accumulation. Subsequently, 750 g of 48% solid content styrene–butadiene rubber (SBR) emulsion was incorporated and stirred similarly, first at 100 rpm for 10 minutes and then at 600 rpm for 30 minutes. For Hac treatment (HAcT) in the slurry, 0.3 L of 99% HAc was added and stirred at 600 rpm for no more than 60 minutes. The resulting slurry was then coated onto a carbon-coated stainless-steel current collector using a web coating machine to mass produce high mass loading cathodes.

5.2.3 Materials characterization

The structural changes induced by ion intercalation were examined using an X-ray diffractometer (Rigaku miniFlex600), operating with both Cu-Kα radiation (λ=0.70 nm) across 2θ=5–40° and Mo-Kα radiation (λ=0.15 nm) across 2θ=5–70°. Sample morphology was observed through a field emission scanning electron microscope (FEI Verios G4 UC) equipped with an EDS detector, with platinum sputtering performed beforehand. Raman spectra were acquired on a LabRAM HR Evolution system (laser: 532 nm). Time-of-flight secondary ion mass spectrometry (TOF-SIMS) was carried out using a PHI nano TOF III instrument, where a Bi_3^{++} beam (3 kV, 2 nA, 100 μm raster) was employed for detection, and an Ar^+ beam (2 kV, 100 nA, 400×400 $μm^2$) was applied for depth profiling at a sputtering rate of approximately 9.16 nm min^{-1} on SiO_2. Oxidation states at various voltages were characterized by X-ray photoelectron spectroscopy (K-Alpha+ from Thermo Fisher Scientific Messtechnik). Micro-computed tomography (ZEISS Xradia 620 Versa, 40× lens) data were reconstructed via a filtered-back projection algorithm (XMReconstructor, Carl Zeiss Inc.), and processed in Avizo 2020.2 (ThermoFisher) for segmentation and quantitative analyses. Following a median filter to enhance the signal-to-noise ratio, the pristine sample was segmented by grayscale into three phases—MnO_2, carbon black, and pores.

5.2.4 Electrochemical measurement

The slurry was prepared by mixing the active materials (MnO_2), carbon black (Super P, TIMCAL Graphite & Carbon), and PVDF at a weight ratio of 7:2:1 using NMP; the mixture was then coated on carbon paper or stainless steel using automatic coating machine. After drying in a vacuum oven at 60 °C for 24h, cathodes with ≈ 0.5-21.2 mg cm^{-2} of the active materials were achieved. The coin cells in Chapter 5 assembled and tested in the same way as in Chapter 4.

5.3 Computational methods

The total energy calculations and geometry optimizations based on density functional theory (DFT) were carried out in VASP by Dr. Chen Shen.[20] We used generalized gradient approximation Perdew-Burke-Ernzerhof functional for the exchange-correlation interactions,[21] projected augmented-plane-wave method,[22] cutoff energy of 500 eV, and *k*-point of 2×2×1 for the integration of the electronic Brillouin zone. For geometrical optimizations, the convergence criterion of the total energy was below 10^{-5} eV and the force was below 0.03 eV/Å. The diffusion barriers of H atom on the surface were calculated by using the climbing-image nudged elastic band (CI-NEB) method.[23] The MnO_2 surface was represented by slabs with 2×2 supercell and four layers, and vacuum value was set to 15 Å in the normal direction.

5.4 Results and discussion

5.4.1 Phase characterization of high loading cathodes after HAc treatment

The XRD pattern for commercial MnO_2 is displayed in Figure 5.1b, showing characteristic 2θ peaks at 22.46°, 35.68°, 37.50°, 43.0°, 56.46°, and 67.88°, which correspond to the (110), (130), (021), (121), (211), and (002) planes, respectively. This pattern matches the γ-MnO_2 structure (JCPDS no. 14-0644) with lattice parameters $a = 4.398$ Å, $b = 2.863$ Å, $c = 4.532$ Å, and $\alpha = \beta = \gamma = 90°$.[24] Priced at approximately £0.87 kg^{-1}, this commercial γ-MnO_2 represents an economical choice for fabricating cathodes for AZIBs. Figures 5.1c and 5.1d showcase scanning electron microscope (SEM) images of the MnO_2-based cathodes. Figure 5.1c captures the electrode surface morphology without HAcT after a baseline experiment (BE), showing agglomeration and large particle clusters averaging about 20 μm in diameter. Such agglomeration can degrade the electrode's electrochemical performance by reducing its effective surface area and obstructing ion transport pathways. [25] In contrast, Figure 5.1d illustrates the post-HAcT cathode surface morphology as the differential experiment (DE), where agglomeration is markedly reduced. This treatment disperses the large clusters into a uniform particle distribution with an average size of about 5 μm, thereby enhancing the cathode’s surface area and improving its ionic accessibility and wettability with the electrolyte. Figure 5.1e and 5.1f present 3D time-of-flight secondary ion mass spectrometry (TOF-SIMS) images of various ions including C, O, OH^-, COO^-, CH^+, CO^+, COH^+, and Mn^+ from the BE and DE. The HAcT significantly increases the presence of functional groups such as hydroxyl (OH^-), carboxylate (COO^-), carbonyl (CO^-), and others across both the surface and deeper layers of the cathode material.

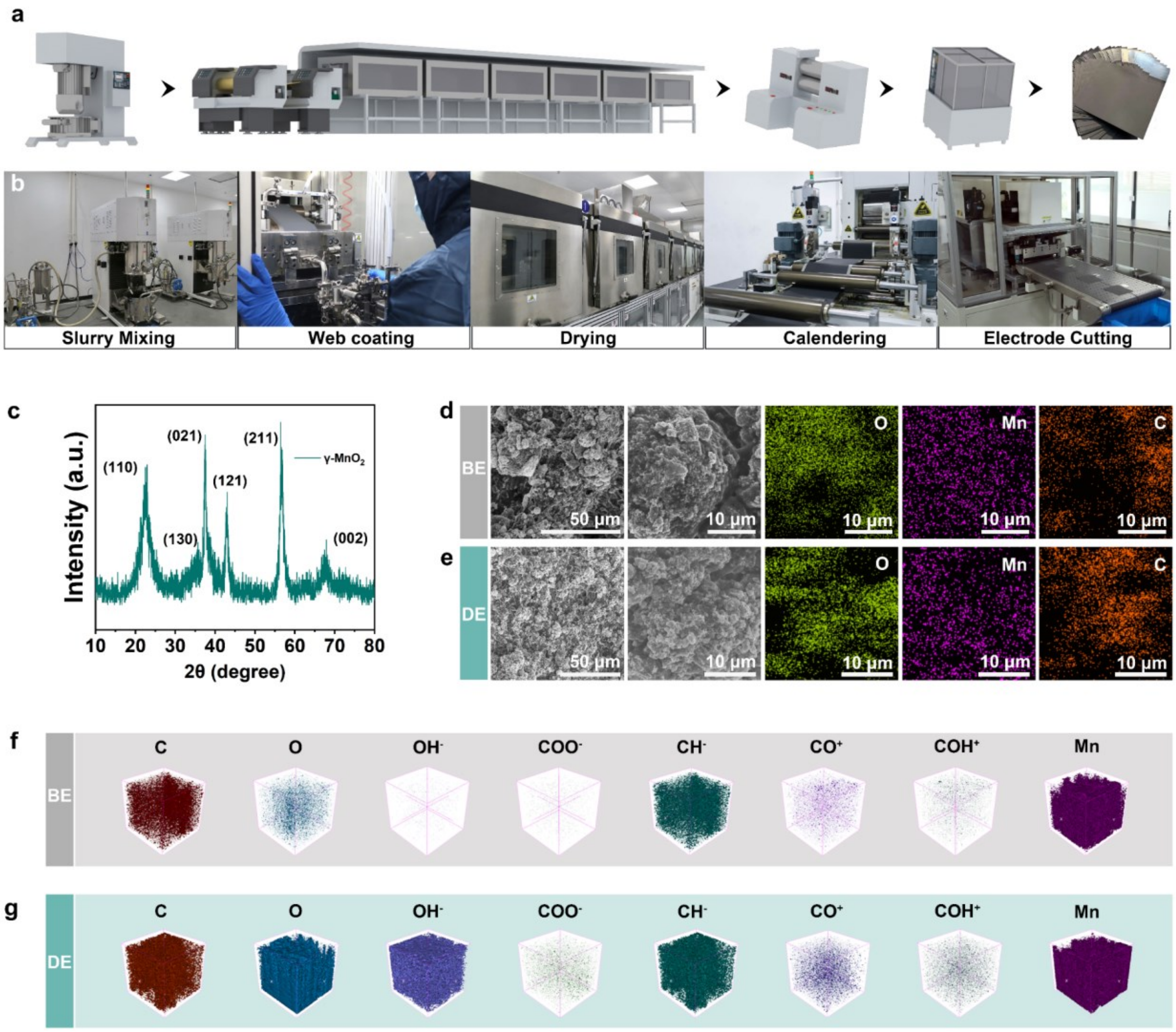

Figure 5.1 (a) Schematic diagram of AZIBs cathode production redesigned according to LIBs production line (b) Optical photo of the automated cathode production line, including slurry mixing, web coating, drying, calendaring, and electrode cutting. (c) XRD pattern of raw material commercial γ-MnO_2. SEM images of (d) BE and (e) DE cathodes after electrode cutting. TOF-SIMS of (f) BE and (g) DE cathodes, showing HAcT introduced various functional groups into the cathodes.

5.4.2 Protons dehydrated on the cathode surface

The electrochemical performance of BE and DE was initially investigated using coin cell configurations, which is a common method in AZIBs research. To understand the effect of HAcT on the cathode's electrochemical behavior, cyclic voltammogram (CV) curves for BE and DE, fabricated with the same method (including binder, carbon agent, and carbon paper current collector), were measured at scan rates ranging from 0.1 to 1 mV s^{-1} within a potential window of 0.8 to 1.9 V. As shown in Figure 5.2a and 5.2e, at low scan rates, DE exhibited two pairs of reduction and oxidation peaks at 1.37, 1.28 V, 1.55 and 1.61 V, respectively. In contrast, BE displayed redox peaks at 1.36, 1.25, 1.56, and 1.62 V, indicating larger polarization compared to DE. Notably, the full cell with the HAcT MnO_2 cathode demonstrated a redox peak shape similar to that of BE, suggesting a proton and Zn^{2+} co-storage mechanisms.[26, 27] Furthermore, DE's CV curves at various scan rates were very similar, indicating consistent reaction behaviors and kinetics across different rates. The potential difference (Δφ) between the oxidation and reduction peaks in a quasi-reversible electrochemical reaction increased with scan rate.[28] However, in a well-reversible electrochemical system, this increase would be alleviated.[29] Figure 5.2a shows that as the scan rate increased, the shifts for BE's peaks P1, P2, P3, and P4 were 0.091, 0.057, 0.064, and 0.075 V, respectively. In comparison, DE's peak shifts (shown in Figure 5.2e) were 0.056, 0.023, 0.050, and 0.048 V, respectively, indicating a more reversible electrochemical system formed by the HAcT cathode. These findings suggest that HAcT not only effectively reduced the polarization of the cathode material but also enhanced the reversibility of its redox reactions, contributing to improved electrochemical performance.

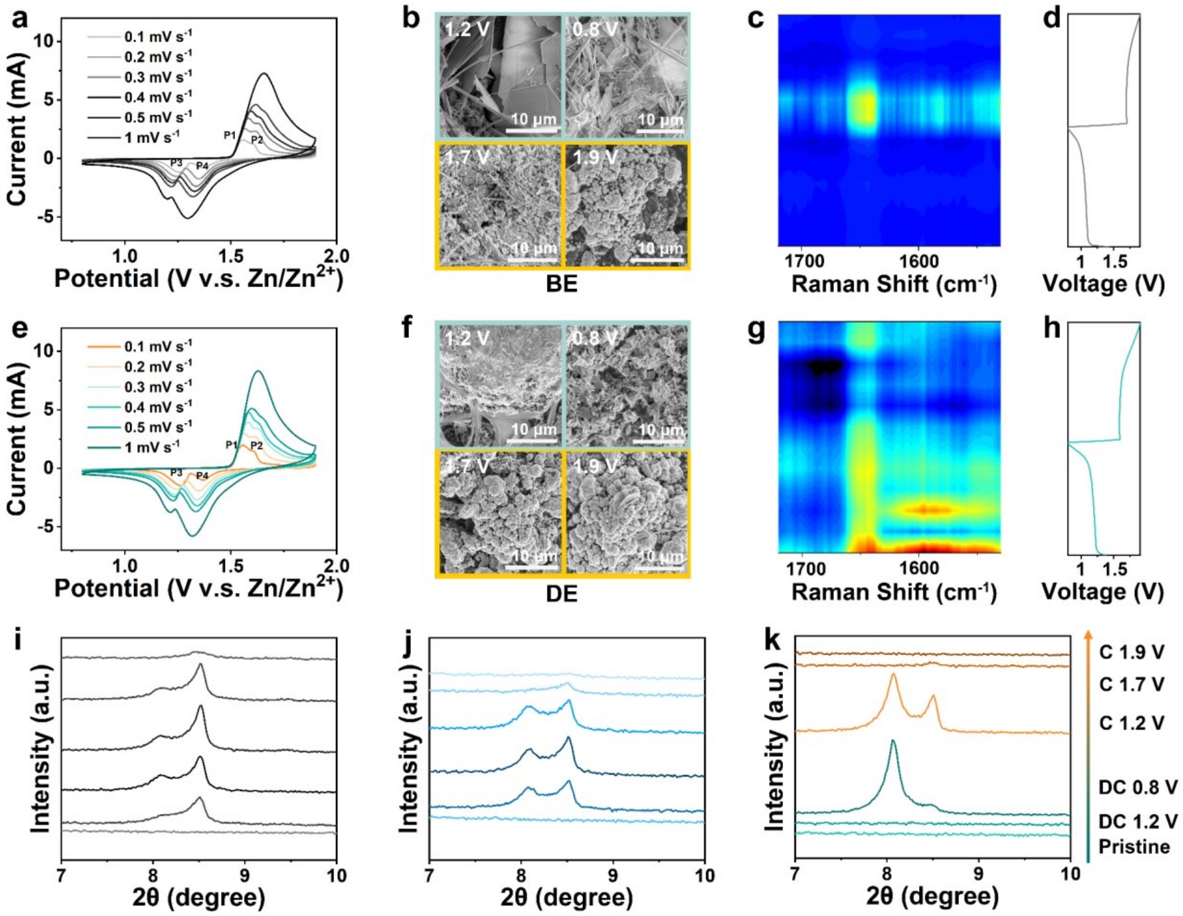

Figure 5.2 CV curves of (a) BE and (e) DE, which shows HAcT reduced the polarization of charge and discharge in AZIBs. *Ex-situ* SEM images of (b) BE and (f) DE at various discharge and charge states: 1.2 V and 0.8 V during the discharge process, 1.7 V and 1.9 V during the charge process. *In-situ* Raman spectra of (c) BE and (g) DE and the corresponding charge and discharge profiles of (d) BE and (h) DE. *Ex situ* XRD pattern of (i) BE, (j) low mass loading HAcT cathodes, and (k) high mass loading HAcT cathodes at various state of discharge/charge (discharge: DC 1.2 V, DC 0.8 V; charge: C 1.2 V, C1.7 V, C 1.9 V) in the first charge and discharge process with focusing on 2θ between 7-10 degree, showing the ratio of $Zn_4SO_4(OH)_6 \cdot 4H_2O$ and $Zn_4SO_4(OH)_6 \cdot 5H_2O$ in generated ZHS.

To further investigate the kinetic processes of different cathodes, their diffusion-controlled and capacitive contributions were evaluated based on the 4 peaks in Figure 5.2a and 5.2d. According to theoretical predictions, the peak current (i) and sweep rate (v) should follow Equation (5.1),[30]

$$i = a v^b \tag{5.1}$$

hence, $\log(i) = \log(a) + b\log(v)$

where a and b can be calculated by fitting a linear curve to the log-log plot of the peak current and the sweep rates (Figure 5.3a and 5.3b). When the value of b is close to 1, the electrochemical reaction is primarily governed by capacitive-controlled kinetic process, while a value near 0.5 indicates a dominance of the diffusive-controlled kinetic process.[31] For the BE cathode, the b values for peaks P1, P2, P3, and P4 were found to be 0.66, 0.72, 0.50, and 0.79, respectively, suggesting that the kinetic behavior of the BE cathode is mainly diffusion-controlled. The DE cathode exhibited b values of 0.62, 0.71, 0.50, and 0.75 for peaks P1, P2, P3, and P4, respectively, indicating that diffusion also predominates in the DE cathode kinetics. Comparing the b values of BE and DE reveals that HAcT significantly influences the electrochemical reaction of protons during the charge/discharge process. Peaks P1 and P4 correspond to the redox peaks of proton electrochemical reactions. A lower b value for them in the DE cathode indicates that HAcT makes the storage of protons more inclined to the (de)intercalation mechanism of the battery compared to the bare MnO_2 cathode. However, HAcT has a minimal effect on the electrochemical reaction behavior of Zn^{2+} (P2 and P3).

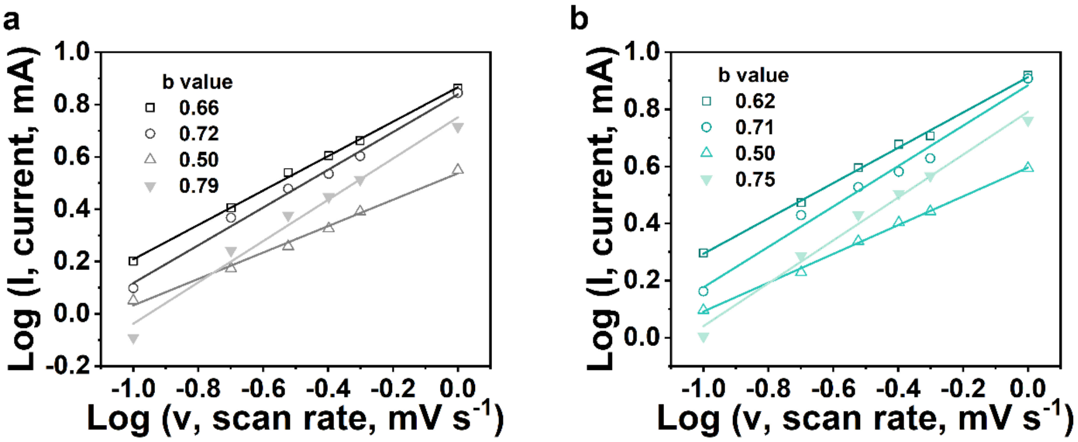

Figure 5.3 Diffusion-capacitive control contribution of (a) BE and (b) DE based on cyclic voltammogram (CV) curves.

As shown in Figure 5.2b and 5.2f, *ex-situ* SEM images of BE and DE (both with the mass loading of ~5 mg cm^{-2}) under 2 A g^{-1} current density conditions show the surface morphology of the cathodes under different potential conditions (0.8, 1.2, 1.7, 1.9 V, respectively). During the discharge process, both BE and DE generated flaky ZHS on the surface. When the discharge process reaches 1.2 V, large flakes of ZHS with a size of 10-30 μm begin to be generated in the BE. When fully discharged to 0.8 V, ZHS in BE maintains 1.2 V. In contrast, when fully discharged to 0.8 V, the ZHS in DE was relatively smaller than BE, only exhibiting a uniform 2 μm. During the charging process, at the same potential of 1.7 V, DE formed uniform flower-like $Zn_xMnO(OH)_y$, while BE did not form, which corresponds to the CV curves, showing smaller polarization of DE. In the fully charged state, uniform flower-like $Zn_xMnO(OH)_y$ is formed on both BE and DE surfaces, indicating a conversion-type mechanism rather than reversible proton storage, which is in agreement with previous studies.[32] *In-situ* Raman spectra of BE and DE were acquired to investigate the HAcT cathode evolution process. As shown in Figure 5.2g, a broad band at 1601 cm^{-1} was observed in the Raman spectra. As the level of carboxymethylation increased, the intensity of this band also increased. The broad band generated at 1601 cm^{-1} corresponds to salt form (COO^-R^+) rather than the carboxylic acid form.[33] The stretching vibration of C=O can be distinguished as two types, according to the location of the bands, a strong band at 1550–1720 cm^{-1} region attributed to carbonyl compounds, and a band in 1740–1800 cm^{-1} ascribed to carboxylic acid.[34] Although the bands at 907, 1310 and 1402 cm^{-1}, and the shoulder band at 1253 cm^{-1}, attributed to the carboxymethyl groups, also showed progressive increases after carboxymethylation, they were not suitable marker bands since they were attributed to other vibrations such as C-H stretching, anomeric skeleton and C-O-H stretching and bending, whereas the 1601 cm^{-1} band was attributed solely to the substituted carboxymethylate species.

During the discharge process of BE, although cations (protons and Zn^{2+}) migrate towards the cathode, there is no significant surface change. In the charge process, free OH^- move towards the cathode, facilitating an enolization reaction, which increases the C=O stretching vibration. Comparing Figure 5.2c and 5.2g, HAcT introduced new surface reactions and divides the DE discharge process into three stages. In the initial stage (1.5 to 1.22 V), the intensity of the broad peaks for carboxylate (O-C=O) and carbonyl (C=O) groups weakens as anions interact with protons and Zn^{2+}, indicating the coordination between Zn^{2+}/proton and carbonyl groups to form Zn-O-C or C-OH groups. During the platform stage (around 1.2 to 1.20 V), the intensity of carboxylate increases, suggesting a dehydration and an initial de-coordination process from $Zn^{2+}(C\text{-}O^{-})_2$ (or C-OH) to Zn^{2+}/H, as cations detach from the surface and move into the bulk.[27] In the final stage of discharge (1.2 to 0.8 V), the carboxylate intensity weakens again while the carbonyl group regains strength, indicating further de-coordination of cations to form C=O. Based on previous studies, a structural model for bulk γ-MnO_2 was constructed, as depicted in Figure 5.4a, for density functional theory (DFT) calculations.[35, 36] The model features a one-dimensional tunnel for proton transport, leading to the construction of the γ-MnO_2 (100) surface shown in Figure 5.4b. Both O and Mn atoms are present on this surface. When carboxylate is introduced onto the γ-MnO_2 surface, the O atoms in carboxylate form covalent bonds with Mn atoms on the (100) surface, as illustrated in Figure 5.4c. The energy profile for the pristine MnO_2 surface (Figure 5.5a) indicates that a proton requires 0.275 eV to diffuse from far away to adsorb on the surface and faces an energy barrier of 0.901 eV to diffuse to a stable adsorbed structure. For the MnO_2 surface functionalized with carboxylate, these energy barriers are reduced to 0.165 eV for proton diffusion to the surface and 0.234 eV for diffusion to the stable structure. This suggests that proton diffusion from the surface to the interior is facilitated after functionalizing the MnO_2 surface with carboxylate.

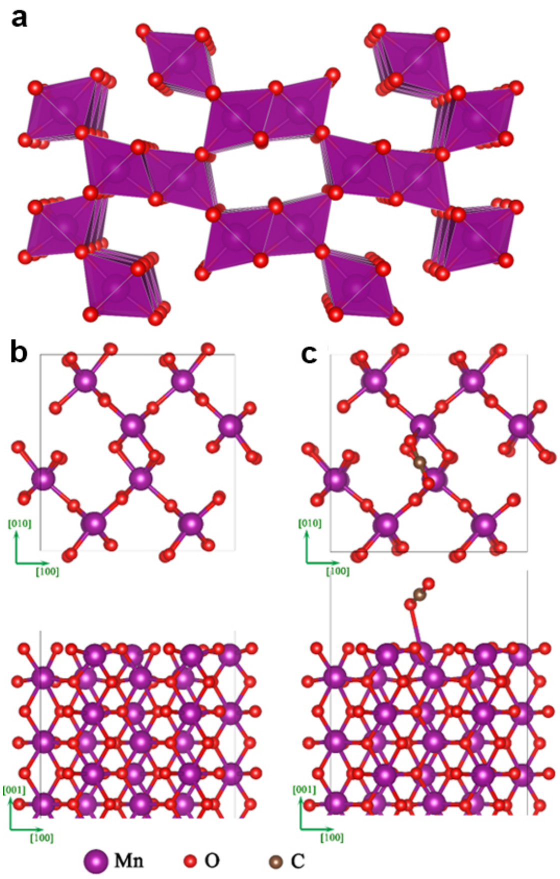

Figure 5.4 (a) Structural model for γ-MnO_2, the purple and red atoms represent Mn and O atoms, respectively. Top and side views of (b) pristine and (c) COO^- functionalized γ-MnO_2 (100) surface.

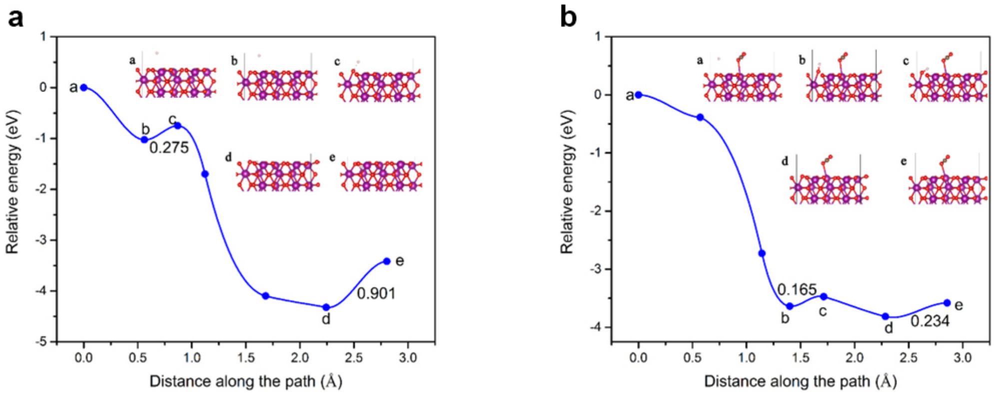

Figure 5.5 Energy profile of a proton diffuse far from the surface into the interstitial layer for (a) pristine MnO_2 (100) surface, (b) MnO_2 surface functionalized with COO^-.

Ex-situ XRD analysis was carried out to investigate the influence of dehydration of proton on regulating byproduct ZHS of HAcT at different voltage, as depicted in Figures 5.6 and 5.7. We examined the structural evolution of DE and BE at similar unit mass loading (~5 mg cm^{-2}) by performing *ex-situ* XRD measurements at specific states of charge and discharge processes, ranging from 0.8 to 1.9 V, at a current density of 2 A g^{-1}. As in other AZIBs, $Zn_4SO_4(OH)_6{\cdot}nH_2O$ (ZHS, n = 4 or 5) was generated on the cathode during discharge when cations moved to the cathode. However, the peak gradually became inconspicuous during the charge process due to the proton and Zn^{2+} leaved from cathodes, which reduced the intensity of the characteristic peaks during cycling.[37] Specifically, during the discharge process, proton and Zn^{2+} migrate to the cathode, leading to the formation of ZHS. The reverse process occurs during the charge, resulting in the disappearance of ZHS. The formation of ZHS can be expressed by Equation (5.2).[37]

$$12OH^- + 2SO_4^{2-} + 8Zn^{2+} + 2nH_2O \rightleftharpoons 2Zn_4(OH)_6SO_4 \cdot nH_2O \quad (n = 4\ or\ 5) \qquad (5.2)$$

During the discharge process to 0.8 V, the amount of ZHS would be increased on the cathode, which is also consistent with previous studies. There would be two different ZHS phases, namely $Zn_4SO_4(OH)_6{\cdot}4H_2O$ (ICDD No. 00-044-0673) and $Zn_4SO_4(OH)_6{\cdot}5H_2O$ (ICDD No. 00-039-0688). During the cycling of BE, as shown in Figure 5.2i, the phase of ZHS was dominated by $Zn_4SO_4(OH)_6{\cdot}4H_2O$ during the discharge process. $Zn_4SO_4(OH)_6{\cdot}5H_2O$ was gradually produced with the change of potential, which is consistent with the previous literature. At the initial potential, H_3O^+ has not been completely dehydrated, and the cathode surface is at a local low concentration of H_2O molecules, so $Zn_4SO_4(OH)_6{\cdot}4H_2O$ is dominant at this time. As part of H_3O^+ gradually dehydrates on the cathode surface, the local concentration of water molecules increases, generating a small amount of $Zn_4SO_4(OH)_6{\cdot}5H_2O$. As shown in Figure 5.2j, the cycle of the DE cathode follows the law of a typical MnO_2-based cathode, but the HAcT increased the proportion of $Zn_4SO_4(OH)_6{\cdot}5H_2O$ during the discharge process. When the HAcT cathode loading increased to ~15 mg cm^{-2}, the peak intensity of ZHS was significantly enhanced (Figure 5.8). It is worth noting that during the cycling process of the HAcT cathode, the proportion of $Zn_4SO_4(OH)_6{\cdot}5H_2O$ in ZHS further significantly increased and became dominant and showed excellent reversibility (Figure 5.2k). As shown in Figure 5.9, DFT results show that when carboxylate and carboxyl are on the γ-MnO_2 surface, water molecules tend to remain on the cathode surface after proton dehydration and form a water-rich interface between the electrolyte and the cathode. However, $Zn_4SO_4(OH)_6{\cdot}4H_2O$ still dominates at the low mass loading conditions after HAcT, because there is not enough bulk space to allow free protons to intercalate, so the protons are not dehydrated enough. Under high mass loading conditions, more surface is provided to generate more ZHS. Thick cathodes provided sufficient bulk phase for the dehydrated protons to intercalate, which increases the local concentration of free water molecular on the surface, making $Zn_4SO_4(OH)_6{\cdot}5H_2O$ the dominant ZHS byproduct.

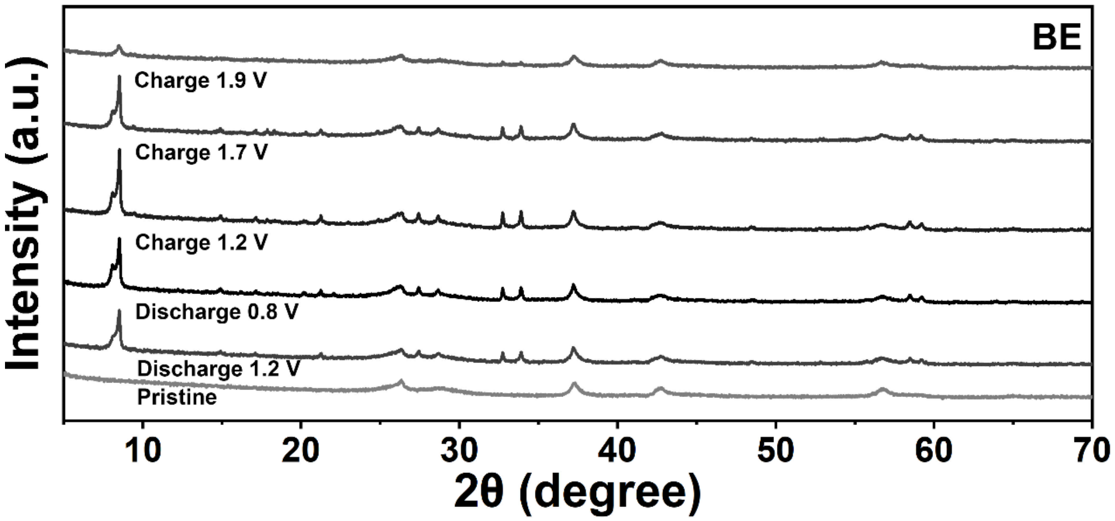

Figure 5.6 *Ex-situ* XRD of BE cathodes at various charge of state in the first charge and discharge process.

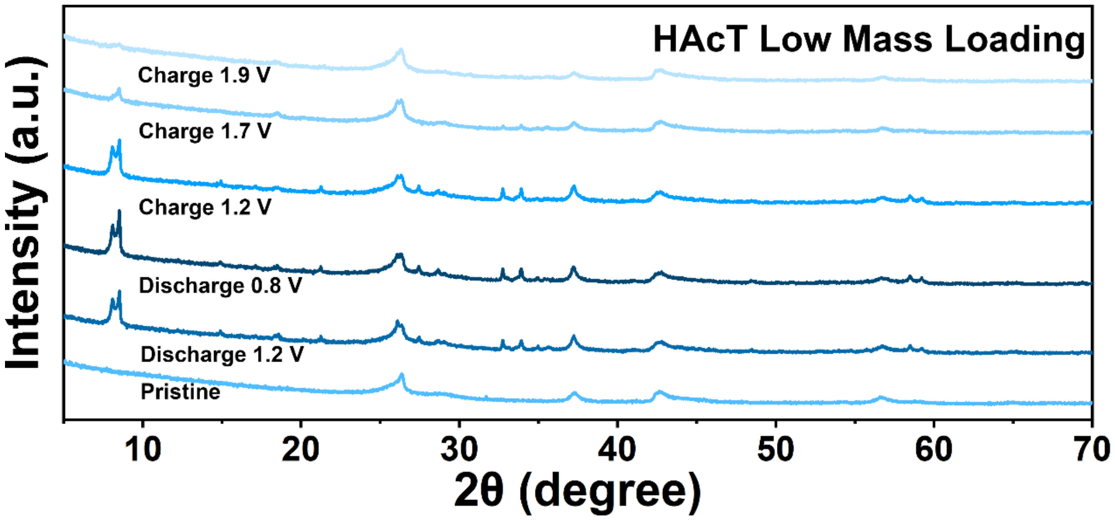

Figure 5.7 Ex-situ XRD of HAcT low mass loading cathodes at various charge of state in the first charge and discharge process.

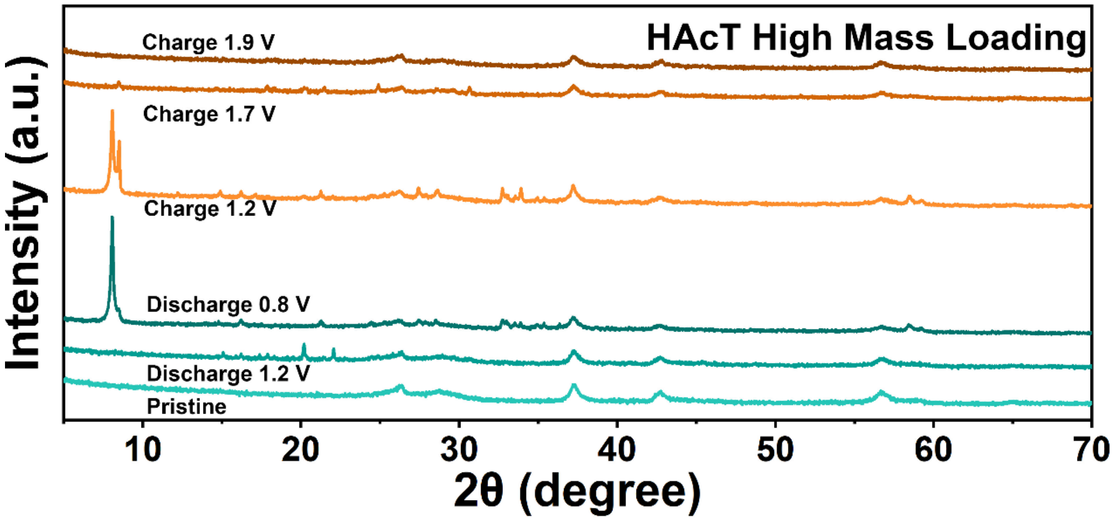

Figure 5.8 Ex-situ XRD of HAcT high mass loading cathodes at various charge of state in the first charge and discharge process.

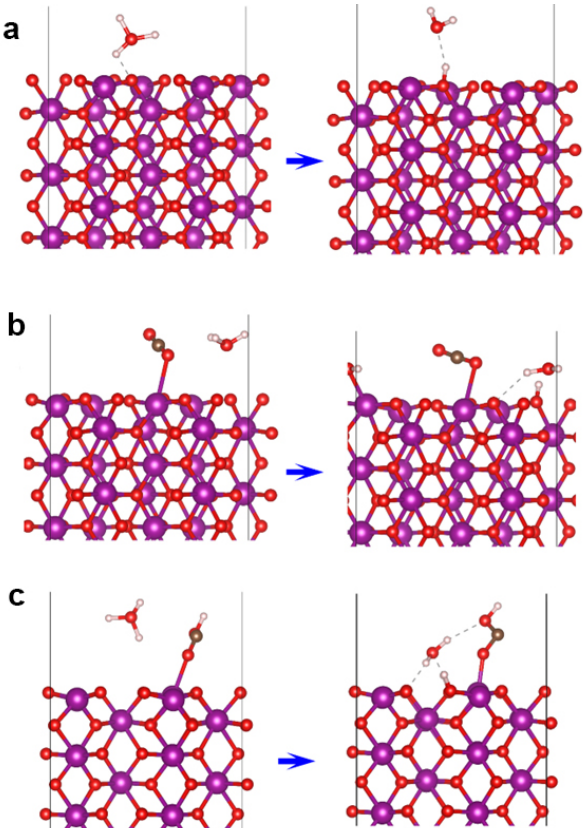

Figure 5.9 Side views of (a) pristine MnO_2 (100) surface, (b) MnO_2 surface functionalized with COO^-, (c) MnO_2 surface functionalized with COOH adsorbing H_3O before and after optimization.

5.4.3 Bulk-contributed capacity increases in high mass loading cathodes

Based on previous study, the surface reaction of MnO_2-based cathode in AZIBs can be expressed as follows to provide electron transfer,[10, 38]

During charge process:

$$Zn_4SO_4(OH)_6 \cdot nH_2O + Mn^{2+} \rightarrow Zn_xMnO(OH)_y + (y-4)H^+ + (n-y+5)H_2O + (4-x)Zn^{2+} + SO_4^{2-} + (y-2x)e^- \tag{5.3}$$

During discharge process:

$$Zn_xMnO(OH)_y + (y+2)H^+ + (y-2x)e^- \rightarrow Mn^{2+} + xZn^{2+} + (y+1)H_2O \tag{5.4}$$

$$4Zn^{2+} + SO_4^{2-} + 6OH^- + nH_2O \rightarrow Zn_4SO_4(OH)_6 \cdot nH_2O \tag{5.5}$$

As shown in Figure 5.10a and 5.11a, the *ex-situ* SEM images shows the generation of $Zn_xMnO(OH)_y$ during the charge process, which corresponds to surface reaction of Equation (5.3). In the fully charged state, the peak of Mn-OH bond was significantly prominent in BE and low loading HAcT cathodes as shown in *ex-situ* XPS (Figures 5.10b and 5.11b). However, the high loading HAcT cathodes exhibited a stable Mn-O-Mn bond throughout the charge-discharge cycle, as shown in the ex-situ XPS in Figure 5.12a and 5.12b, the peak of Mn-O-Mn bond dominates both on the surface at the fully charged and fully discharged state, with proton intercalation and deintercalation dominating rather than conversion between ZHS and $Zn_xMnO(OH)_y$. This shows that under high mass loading, the bulk of the cathode material is stable, and the proportion of capacity contributed by surface reactions was weakened.

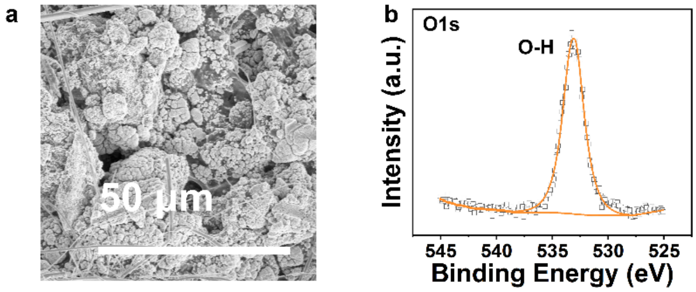

Fully Charged 1.9 V BE

Figure 5.10 *Ex-situ* (a) SEM of surface morphology and (b) XPS of O1s of BE MnO_2 cathode in fully charged state.

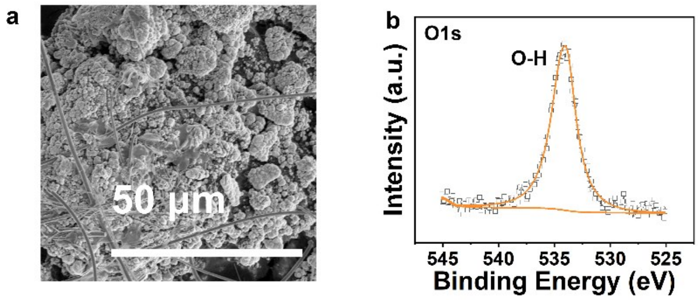

Fully Charged 1.9 V HAcT Low Mass Loading

Figure 5.11 *Ex-situ* (a) SEM of surface morphology and (b) XPS of O1s of low loading HAcT MnO_2 cathode in fully charged state.

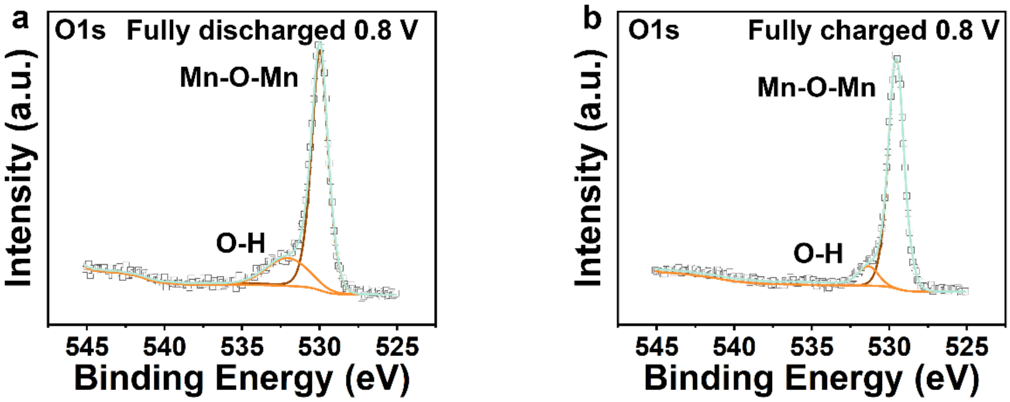

Figure 5.12 *Ex-situ* XPS of O1s of high loading HAcT MnO_2 cathode in (a) fully discharged and (b) fully charged state.

Figures 5.13 and 5.14 show the *ex-situ* SEM images of high mass loading HAcT cathodes during discharge and charge process, respectively. Under high mass loading conditions of HAcT cathodes, the surface of the cathode does not facilitate the formation of new agglomerates of flower-like $Zn_xMnO(OH)_y$, which is with agreement with *ex-situ* XPS of Figure 5.12a and 5.12b. The Mn-OH bond never dominates in the high mass loading cathodes during charge and discharge, and the Mn-O-Mn bond remains stable. As the cathode material became thicker, the process of Equation (5.3) was weakened, the Mn-O-Mn bond remains stable, and no large amount of $Zn_xMnO(OH)_y$ was generated. As a result, the dissolution reaction of MnO_2 caused by Equation (5.4) was weakened during the discharge process, thereby reducing the concentration of Mn^{2+} in the solution compared to low mass loading cathodes. During the charging process, due to Le Chatelier's principle, the low concentration of Mn^{2+}

weakens the conversion of Equation (5.5). $Zn_4SO_4(OH)_6 \cdot nH_2O$ reacts with the released protons and undergoes reversible dissolution. The HAcT promotes proton transport deeper into the bulk material, effectively preventing the formation of new surface agglomerates of flower-like $Zn_xMnO(OH)_y$.

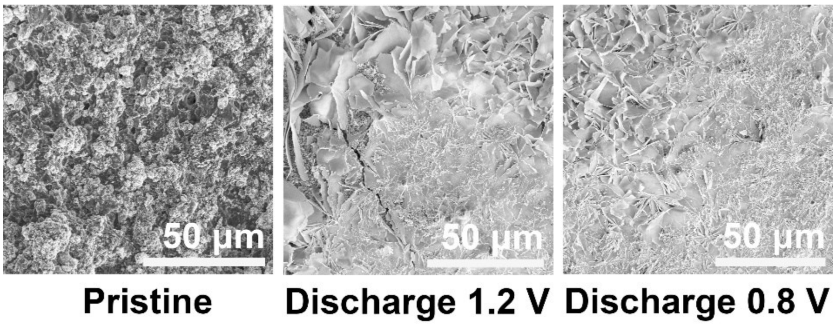

Figure 5.13 *Ex-situ* SEM images of surface morphology of high loading HAcT MnO_2 cathode during discharge process.

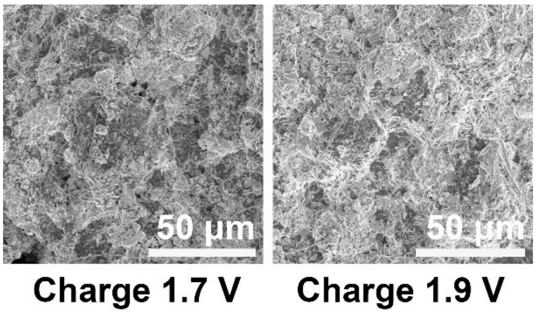

Figure 5.14 *Ex-situ* SEM images of surface morphology of high loading HAcT MnO_2 cathode during charge process.

In order to more intuitively demonstrate the shift from a surface-dominated capacity to a bulk-dominated capacity, the experimental work conducted a systematic increase in mass loading under accurate control from automated cathode production line, with specific mass loadings set at 0.5, 2.8, 6.5, 7.3, 16.9, 19.3, and 21.2 mg cm^{-2}. Figure 5.15a illustrates the cycle performance based on areal specific capacity. At low mass loading of 0.5 mg cm^{-2}, the activation process is markedly evident, with the specific capacity reaching 692 mAh g^{-1} at the 48th cycle. After 48 cycles, the reversible capacity gradually decreased and reached 279 mAh g^{-1} at the 100th cycle. However, as the mass loading increases, the relative contribution of surface reactions diminishes, transitioning the dominant mechanism towards bulk contributions and the activation process gradually fades. At higher loadings, cathodes exhibited lower initial Coulombic efficiencies. For instance, the cathode at 21.2 mg cm^{-2} showed an initial Coulombic efficiency of ~76%. This lower Coulombic efficiency is attributed to the ZHS interface generated to form CEI by the charge-discharge process based on Equation (5.2).[39] Starting from the second cycle, the intercalation/deintercalation mechanism dominates instead of deposition and dissolution reactions on the cathode surface in high mass loading condition. As the mass loading increases, the cycle performance becomes more stable, although the specific capacity decreases. Nonetheless, the areal capacity continues to rise from 0.18 to 1.56 mAh cm^{-2}, highlighting the effective bulk capacity contributions facilitated by HAcT. As the proportion of surface is reduced, the dissolution and deposition of MnO_2 in the surface reaction is no longer dominant, and the double electron transfer reaction turns to single electron transfer, which leads to lower specific capacity in high mass loading condition. Although the specific capacity at high mass loading is lower than that at low mass loading, HAcT cathodes still exhibited considerable cycle performance and higher areal specific capacity in high mass loading due to its stable bulk structure and efficient dehydration of proton.

Improving high-loading cathode performance is crucial for reducing manufacturing costs, decreasing battery cell weight, enhancing production capacity, and advancing emerging battery technology to the market. Unlike mature LIBs and lead-acid batteries, the future market for AZIBs will focus on scenarios requiring high-rate, high-power, and high-safety performance, as different battery technologies have varying "comfortable zone" for discharge rates.[40-43] For AZIBs production, it is essential to lower the power cost of cells, boost their power density, and increase the power manufacturing capacity of production lines. By considering this, the rate performances of the DE and BE cathodes in high mass loading of ~12 mg cm^{-2} were measured over a range of current densities from 0.1 to 1 A g^{-1}. The galvanostatic discharge/charge curves (Figure 5.15b and 5.15c) of the DE and BE at various current densities showed similar charge/discharge platforms, but DE showed smaller polarization, indicating superior rate performance resulting from the improved electron transport and ion diffusion kinetics attributed to the modulated electronic structure and ion/charge storage sites from HAcT. As shown in Figure 5.15d, the specific capacities of both cathodes decreased as the current density increased due to the limited electrochemical reaction kinetics. However, the DE battery demonstrated excellent rate capability, delivering high capacities of 130, 109, 95, 82, 68 mAh g^{-1} at current densities of 0.1, 0.2, 0.3, 0.5, and 1 A g^{-1}, respectively. Remarkably, the DE electrode exhibited excellent high-rate performance and the BE electrode showed nearly no capacity at current densities of 0.5 and 1 A g^{-1} at high mass loading conditions. The excellent rate cyclability was demonstrated by recovering the reversible capacity of ~132 mAh g^{-1} with no observable loss at a current density of 0.1 A g^{-1}.

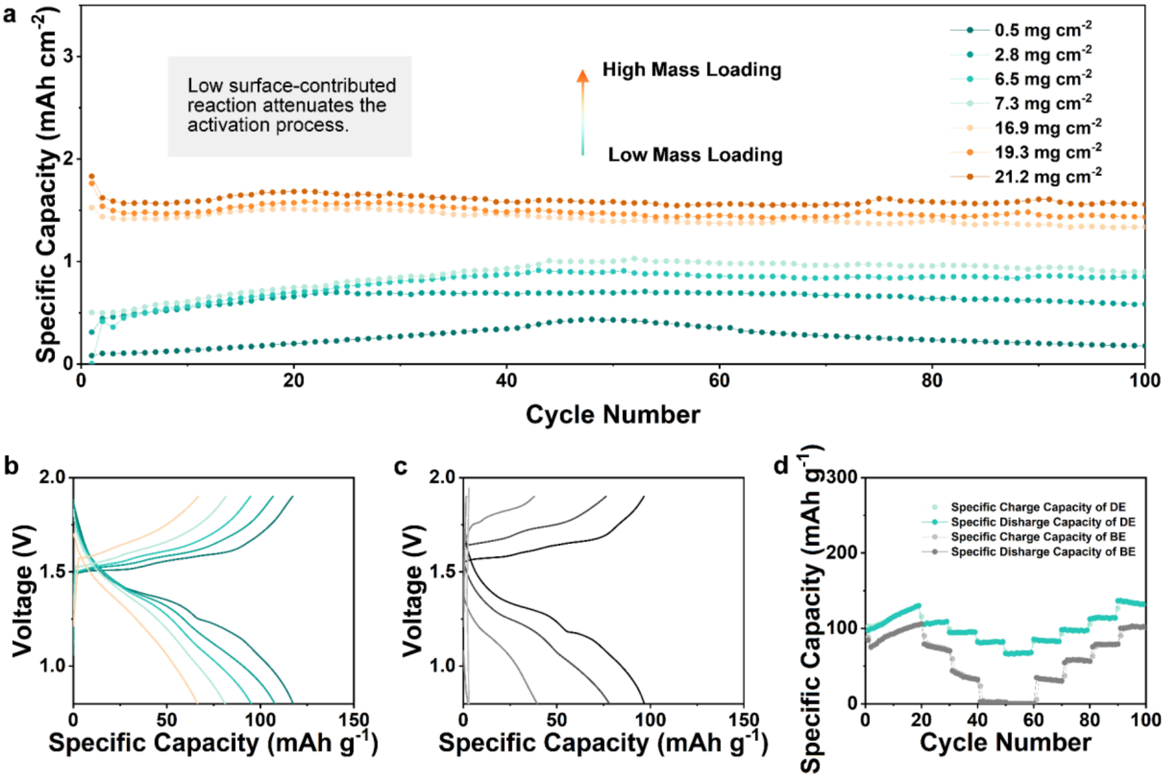

Figure 5.15 (a) Areal specific capacity of HAcT cathodes at various mass loadings (from low to high): 0.5, 2.8, 6.5, 7.3, 16.9, 19.3, and 21.2 mg cm^{-2}. Galvanostatic charge and discharge profiles for (b) DE and (c) BE. (d) Cycle performance of DE compared with BE at different current densities at 0.2, 0.3, 0.4, 0.5 and 1 A g^{-1}.

5.4.4 7.5-Ah prototype AZIBs close to industrialization

To determine the cycle stability of the HAcT cathodes, high-rate tests at a current density of 1 A g^{-1} were carried out on DE and BE, respectively. As shown in Figure 5.16, the HAcT cathode with an active material mass loading of ~6 mg cm^{-2} displayed a discharge capacity of 67 mAh g^{-1} at a current density of 1 A g^{-1} (10C) after 1500 cycles.

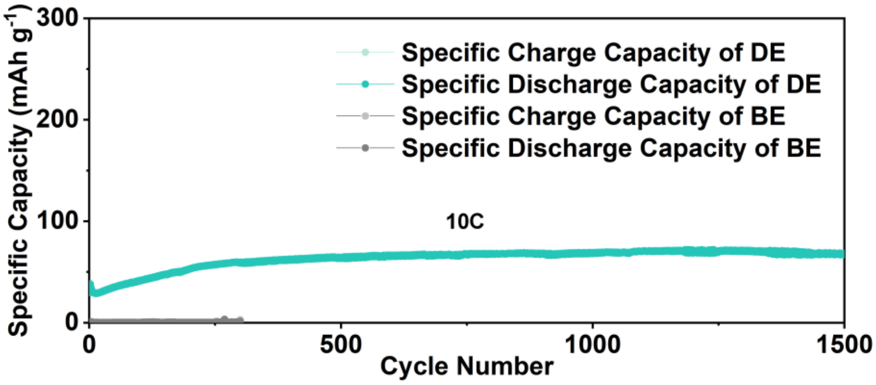

Figure 5.16 Long-term and high-rate cycle performance of DE with a mass loading of 6 mg cm^{-2} at a current density of 1 A g^{-1} (10C), which shows that the HAcT cathode can exhibit a reversible specific capacity of 68 mAh g^{-1} and ~100% retention after 1500 cycles.

Under such high-rate condition, the cathode without HAcT (BE) can hardly provide capacity with the same mass loading. Figure 5.17a shows the schematic diagram of a stacked pouch cell fabricated by the automated production line. Standardized 2-layer stacked 2.2C/1-Ah pouch cells with HAcT were prepared, as shown in Figure 5.17b, showing 100% retention at the 100th cycle, exhibiting an energy density of 50 Wh kg^{-1} and a power density of 110 W kg^{-1}. Furthermore, the optical photo of the 7.5-Ah prototype was shown in Figure 5.17c with 10 layers stacked. The HAcT cathode with a moderate active material loading of ~13.5 mg cm^{-2} and the 7.5-Ah prototype AZIBs was prepared. For safety testing, Nail penetration was conducted to demonstrate the excellent safety of aqueous batteries, as shown in Figure 5.16. At a current density of 0.2 A g^{-1}, the pouch cell delivered ~98% retention after 100 cycles (as shown in Figure 5.17d) with a discharge rate of 1.5C. The energy density reaches 68 Wh g^{-1}. Compared with all research progress of the Ah-level Zn-based pouch cells in the past 2 years (as shown in Figure 5.17e), the prototype pouch cell in this work has achieved highest capacity retention (98% at 100th cycle) and provided over 7 times of capacity compared to other Zn-based energy storage solutions.[44-65] The prototype was tested at different EWs and the corresponding capacity is shown in Table 5.2. Nail penetration was used to demonstrate the prototype's safety performance, with absolutely no smoke or fire as shown in Figure 5.18. The cost calculation of producing AZIBs is shown in Table 5.3. It is worth noting that the energy manufacturing cost of the pouch cells in this work is about £0.13 Wh^{-1}, which is close to commercial stationary LIBs (£0.08 Wh^{-1}). HAcT has almost no increase in manufacturing cost and production time. In other words, by introducing HAc in the slurry mixing process, the power manufacturing capacity of the original production line can be increased by 44.2%, and the power manufacturing cost can be reduced from £0.11 W^{-1} to £0.08 W^{-1}, which is much lower than the power manufacturing cost of stationary LIBs (£0.20 W^{-1}).

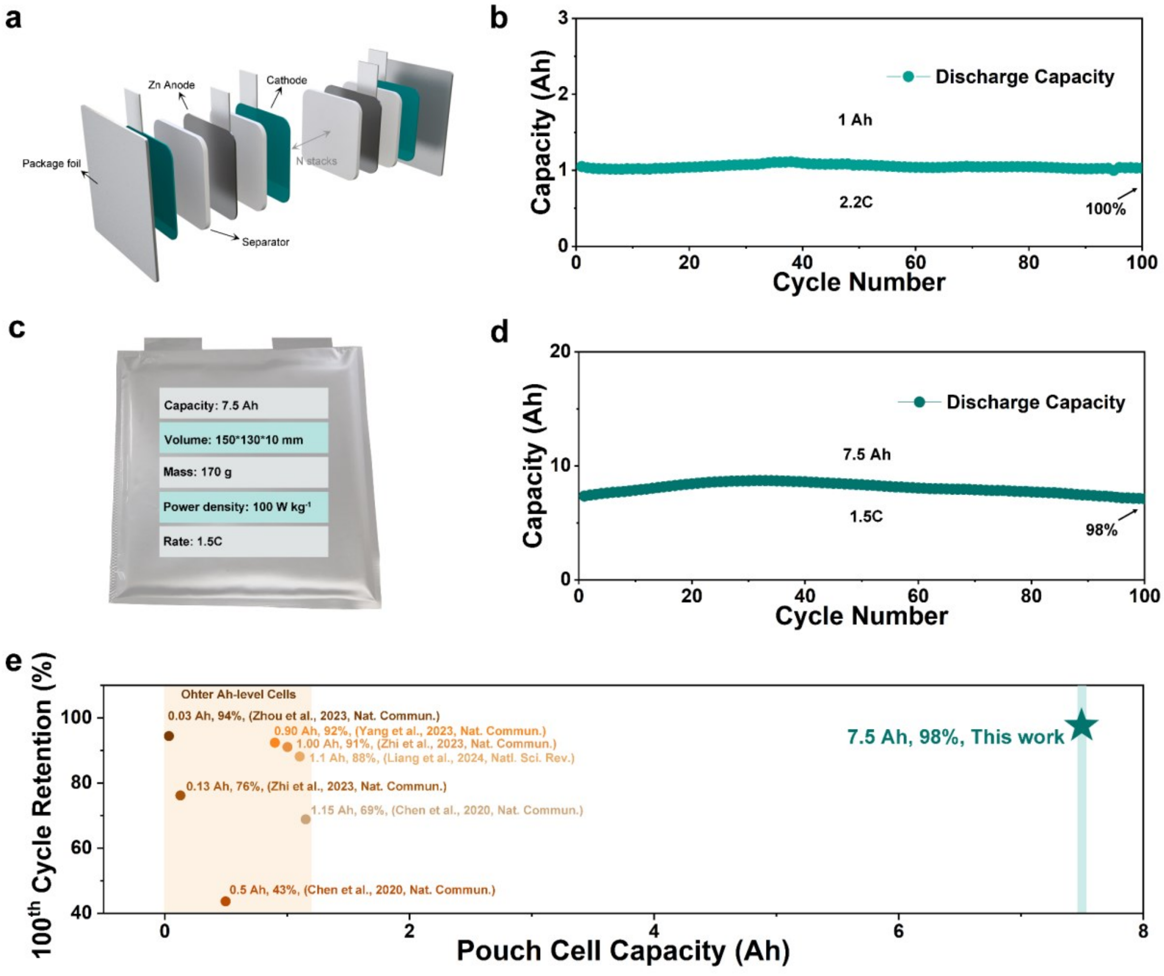

Figure 5.17 (a) Scheme of multi-layer pouch cell. (b) Cycle performance of standardized 1-Ah prototype AZIBs with HAcT cathodes with a discharge rate of 2.2C, showing ~100% retention after 100 cycles. (c) Optical demonstration of 7.5-Ah prototype AZIBs. (d) Cycle performance of 7.5-Ah prototype AZIBs with HAcT cathodes at a current density of 0.2 A g^{-1} with a discharge rate of 1.5C, showing ~98% retention after 100 cycles. (e) Comparison of the AZIBs accomplished in this work with recent advances in Ah-level Zn-based batteries.

Table 5.2 The capacity of soft-pack batteries at different EWs.

Capacity (Ah)	EW
7.5	0.8-1.9
7.2	0.7-1.8
5.3	0.8-1.7
3.8	0.9-1.6
1.1	1.0-1.5

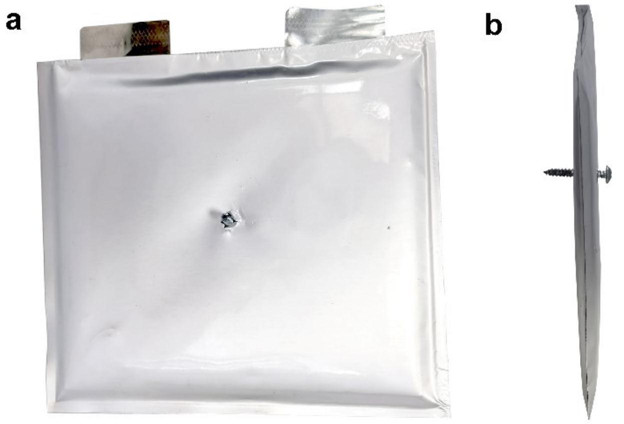

Figure 5.18 Nail penetration test of the pouch cell. (a) Top view; (b) side view.

Table 5.3 Comparison of AZIBs manufacturing cost with and without HAcT

		BE	**DE**
Cell Level	Rate	1.2C	**1.5C**
	Energy density (Wh kg^{-1})	63.1	**68.0**
	Power density (W kg^{-1})	75.7	**102.0**
	Cost per kWh	£143.2	**£132.0**
	Cost per kW	£118.4	**£87.9**
Cathode	Raw material cost (t^{-1})	£866.0	**£869.7**
	Cost per kWh	£4.4	**£4.1**
	Cost per kW	£3.7	**£2.7**
Separator	Raw material cost (m^{-2})	£1.1	**£1.1**
	Cost per kWh	£20.6	**£19.1**
	Cost per kW	£17.1	**£12.7**
Anode	Raw material cost (m^{-2})	£2.6	**£2.6**
	Cost per kWh	£49.9	**£46.3**
	Cost per kW	£41.6	**£30.9**
Electrolyte	Raw material cost (t^{-1})	£1840	**1840**
	Cost per kWh	£4.5	**£4.5**
	Cost per kW	£3.03	**£3.03**
Current collector	Raw material cost (m^{-2})	£2.7	**£2.7**
	Cost per kWh	£51.8	**£48.1**
	Cost per kW	£43.2	**£32.1**
Binder	Raw material cost (t^{-1})	£39003.2	**£39003.2**
	Cost per kWh	£11.1	**£10.3**
	Cost per kW	£8.3	**£6.2**
Conductive agent	Raw material cost (t^{-1})	£18418.2	**£18418.2**
	Cost per kWh	£5.2	**£4.8**
	Cost per kW	£4.3	**£3.2**

5.5 Summary

Small tweak, big leap – a new innovative slurry mixing process fixed small issues and achieved significant performance improvements. This study investigated the effect of enhanced proton storage in detail on the high-rate performance of high-mass-loaded cathodes by redesigning the lithium-ion battery production line to prepare practical MnO_2-based AZIBs and achieved innovation in industrial scale. From the perspective of proton storage, promoting the transition of proton storage from the surface to the bulk of the material is an effective strategy to improve battery performance. By introducing acetic acid (HAc) into the slurry mixing process, significant improvements in proton dehydration and insertion into the cathode material were achieved, which increased the power density of the batteries and boosted manufacturing capacity. Enhanced proton dehydration not only reduces microstructural changes during electrochemical reactions but also lowers energy barriers, thus extending battery lifespan. The HAcT cathode materials demonstrated efficient proton dehydration and insertion mechanisms, significantly improving the cycle stability and high-rate capacity of high-loading cathodes. As the mass loading of the cathode increases, the storage mechanism of the battery undergoes a critical transition from a surface reaction-dominated conversion-type mechanism to a bulk intercalation/deintercalation-type mechanism. This shift effectively prevents the formation of large amounts of $Zn_xMnO(OH)_y$ on the cathode surface, which alleviates the activation process of MnO_2-based AZIBs, maintaining the stability and high electrochemical performance of the cathode materials. By incorporating HAc into the slurry mixing process on a 15-meter automated web coating machine with commercial electrolytic γ-MnO_2, this study achieved the mass production of 7.5-Ah AZIB prototypes. These prototypes demonstrated excellent high-rate cycling performance and 98% capacity retention after 100 cycles, increasing the power manufacturing capacity by 44.2% and reducing power manufacturing costs from £118.4 to £87.9 per kW.

5.6 References

[1] A.I. Osman, L. Chen, M. Yang, G. Msigwa, M. Farghali, S. Fawzy, D.W. Rooney, P.-S. Yap, *Environmental chemistry letters*, **21** (2023) 741-764.

[2] J. Akpan, O. Olanrewaju, *Energies*, **16** (2023) 7049.

[3] A. Kalair, N. Abas, M.S. Saleem, A.R. Kalair, N. Khan, *Energy Stor.*, **3** (2021) e135.

[4] J. Peng, J. Meng, J. Wu, Z. Deng, M. Lin, S. Mao, D.-I. Stroe, *J. Energy Storage*, **71** (2023) 108197.

[5] X. Gao, H. Wu, C. Su, C. Lu, Y. Dai, S. Zhao, X. Hu, F. Zhao, W. Zhang, I.P. Parkin, *Energy Environ. Sci.*, **16** (2023) 1364-1383.

[6] G. Li, L. Sun, S. Zhang, C. Zhang, H. Jin, K. Davey, G. Liang, S. Liu, J. Mao, Z. Guo, *Adv. Funct. Mater.*, (2023) 2301291.

[7] X. Gao, H. Dong, C.J. Carmalt, G. He, *ChemElectroChem*, **10** (2023) e202300200.

[8] X. Fu, Y. Zhou, J. Huang, L. Feng, P. Yu, Q. Zhang, W. Yang, Y. Wang, *Adv. Energy Mater.*, **13** (2023) 2301385.

[9] L. Wang, J. Han, D. Kong, Y. Tao, Q.-H. Yang, *Nanomicro Lett.*, **11** (2019) 1-23.

[10] X. Gao, C. Shen, H. Dong, Y. Dai, P. Jiang, I.P. Parkin, H. Zhang, C.J. Carmalt, G. He, *Energy Environ. Sci.*, **17** (2024) 2287-2297.

[11] H. Yao, H. Yu, Y. Zheng, N.W. Li, S. Li, D. Luan, X.W. Lou, L. Yu, *Angew. Chem., Int. Ed.*, **62** (2023) e202315257.

[12] Y. Zhang, S. Deng, Y. Li, B. Liu, G. Pan, Q. Liu, X. Wang, X. Xia, J. Tu, *Energy Stor. Mater.*, **29** (2020) 52-59.

[13] B. Luo, Y. Wang, L. Sun, S. Zheng, G. Duan, Z. Bao, Z. Ye, J. Huang, *J. Energy Chem.*, **77** (2023) 632-641.

[14] C.A. Reed, *Acc. Chem. Res.*, **46** (2013) 2567-2575.

[15] A.A. Tulub, *The Journal of chemical physics*, **120** (2004) 1217-1222.

[16] S. Saha, J. Jose, *Physical Review A*, **102** (2020) 052824.

[17] L. Zhu, K. Seff, D.H. Olson, B.J. Cohen, R.B. Von Dreele, *The Journal of Physical Chemistry B*, **103** (1999) 10365-10372.

[18] H. Sun, L. Mei, J. Liang, Z. Zhao, C. Lee, H. Fei, M. Ding, J. Lau, M. Li, C. Wang, *Science*, **356** (2017) 599-604.

[19] Y. Marcus, *The Journal of chemical physics*, **137** (2012).

[20] G. Kresse, J. Furthmüller, *Phys. Rev. B*, **54** (1996) 11169.

[21] J.P. Perdew, K. Burke, M. Ernzerhof, *Phys. Rev. Lett.*, **77** (1996) 3865.

[22] P.E. Blöchl, *Phys. Rev. B*, **50** (1994) 17953.

[23] G. Henkelman, B.P. Uberuaga, H. Jónsson, *The Journal of chemical physics*, **113** (2000) 9901-9904.

[24] M. Sun, B. Lan, L. Yu, F. Ye, W. Song, J. He, G. Diao, Y. Zheng, *Materials Letters*, **86** (2012) 18-20.

[25] L. Wu, Y. Dong, *Energy Stor. Mater.*, **41** (2021) 715-737.

[26] J. Chu, Z. Liu, J. Yu, L. Cheng, H.G. Wang, F. Cui, G. Zhu, *Angew. Chem., Int. Ed.*, **136** (2024) e202314411.

[27] Z. Xu, M. Li, W. Sun, T. Tang, J. Lu, X. Wang, *Adv. Mater.*, **34** (2022) 2200077.

[28] X. Fan, Y. Lu, H. Xu, X. Kong, J. Wang, *Journal of Materials Chemistry*, **21** (2011) 18753-18760.

[29] J. Xia, Y. Zhou, J. Zhang, T. Lu, W. Gong, D. Zhang, X. Wang, J. Di, *Small*, **19** (2023) 2301906.

[30] S. Kong, Y. Li, X. Zhang, Z. Xu, X. Wang, Y. Feng, W. Gong, C. Liu, K. Tian, Q. Li, *Small*, **19** (2023) 2304462.

[31] D. Chao, C. Zhu, M. Song, P. Liang, X. Zhang, N.H. Tiep, H. Zhao, J. Wang, R. Wang, H. Zhang, *Adv. Mater.*, **30** (2018) 1803181.

[32] D. Qin, J. Ding, C. Liang, Q. Liu, L. Feng, Y. Luo, G. Hu, J. Luo, X. Liu, *Acta Phys. Chim. Sin.*, **40** (2024) 2310034.

[33] S.-N. Yuen, S.-M. Choi, D.L. Phillips, C.-Y. Ma, *Food chemistry*, **114** (2009) 1091-1098.

[34] N.B. Colthup, L.H. Daly, S.E. Wiberley, *Introduction to infrared and Raman spectroscopy*, (1990) 1-73.

[35] D.A. Kitchaev, H. Peng, Y. Liu, J. Sun, J.P. Perdew, G. Ceder, *Phys. Rev. B*, **93** (2016) 045132.

[36] S. Ma, X. Ye, X. Jiang, W. Cen, W. Jiang, H. Wang, *Journal of Alloys and Compounds*, **852** (2021) 157007.

[37] X. Gao, Y. Dai, C. Zhang, Y. Zhang, W. Zong, W. Zhang, R. Chen, J. Zhu, X. Hu, M. Wang, *Angew. Chem., Int. Ed.*, **62** (2023) e202300608.

[38] H. Chen, C. Dai, F. Xiao, Q. Yang, S. Cai, M. Xu, H.J. Fan, S.J. Bao, *Adv. Mater.*, **34** (2022) 2109092.

[39] N. Zhang, Y.-R. Ji, J.-C. Wang, P.-F. Wang, Y.-R. Zhu, T.-F. Yi, *J. Energy Chem.*, **82** (2023) 423-463.

[40] W. Li, Y. Zhou, H. Zhang, X. Tang, *Energies*, **16** (2023) 4845.

[41] J. Chen, Y. Hu, Q. Zhu, H. Rashid, H. Li, *Energy*, **282** (2023) 128782.

[42] K. Yanamandra, D. Pinisetty, N. Gupta, *Renew. Sustain. Energy Rev.*, **173** (2023) 113078.

[43] S.S. Shah, F. Niaz, M.A. Ehsan, H.T. Das, M. Younas, A.S. Khan, H.U. Rahman,

S.A. Nayem, M. Oyama, M.A. Aziz, *J. Energy Storage*, **79** (2024) 110152.

[44] F. Wang, J. Zhang, H. Lu, H. Zhu, Z. Chen, L. Wang, J. Yu, C. You, W. Li, J. Song, *Nat. Commun.*, **14** (2023) 4211.

[45] Y. Wang, T. Wang, S. Bu, J. Zhu, Y. Wang, R. Zhang, H. Hong, W. Zhang, J. Fan, C. Zhi, *Nat. Commun.*, **14** (2023) 1828.

[46] Q. Cao, Y. Gao, J. Pu, X. Zhao, Y. Wang, J. Chen, C. Guan, *Nat. Commun.*, **14** (2023) 641.

[47] G. Li, Z. Zhao, S. Zhang, L. Sun, M. Li, J.A. Yuwono, J. Mao, J. Hao, J. Vongsvivut, L. Xing, *Nat. Commun.*, **14** (2023) 6526.

[48] H. Jiang, L. Tang, Y. Fu, S. Wang, S.K. Sandstrom, A.M. Scida, G. Li, D. Hoang, J.J. Hong, N.-C. Chiu, *Nature Sustainability*, **6** (2023) 806-815.

[49] S. Jin, J. Yin, X. Gao, A. Sharma, P. Chen, S. Hong, Q. Zhao, J. Zheng, Y. Deng, Y.L. Joo, *Nat. Commun.*, **13** (2022) 2283.

[50] Q. Zhang, Y. Ma, Y. Lu, L. Li, F. Wan, K. Zhang, J. Chen, *Nat. Commun.*, **11** (2020) 4463.

[51] Y. Zhao, S. Guo, M. Chen, B. Lu, X. Zhang, S. Liang, J. Zhou, *Nat. Commun.*, **14** (2023) 7080.

[52] Z. Chen, T. Wang, Z. Wu, Y. Hou, A. Chen, Y. Wang, Z. Huang, O.G. Schmidt, M. Zhu, J. Fan, *Nat. Commun.*, **15** (2024) 3748.

[53] S. Chen, D. Ji, Q. Chen, J. Ma, S. Hou, J. Zhang, *Nat. Commun.*, **14** (2023) 3526.

[54] G. Liang, B. Liang, A. Chen, J. Zhu, Q. Li, Z. Huang, X. Li, Y. Wang, X. Wang, B. Xiong, *Nat. Commun.*, **14** (2023) 1856.

[55] Y. Wang, Q. Li, H. Hong, S. Yang, R. Zhang, X. Wang, X. Jin, B. Xiong, S. Bai, C. Zhi, *Nat. Commun.*, **14** (2023) 3890.

[56] W. Wang, S. Chen, X. Liao, R. Huang, F. Wang, J. Chen, Y. Wang, F. Wang, H. Wang, *Nat. Commun.*, **14** (2023) 5443.

[57] X. Zhang, J. Li, Y. Liu, B. Lu, S. Liang, J. Zhou, *Nat. Commun.*, **15** (2024) 2735.

[58] R. Deng, Z. He, F. Chu, J. Lei, Y. Cheng, Y. Zhou, F. Wu, *Nat. Commun.*, **14** (2023) 4981.

[59] Q. Zhao, W. Huang, Z. Luo, L. Liu, Y. Lu, Y. Li, L. Li, J. Hu, H. Ma, J. Chen, *Sci. Adv.*, **4** (2018) eaao1761.

[60] J. Zhou, M. Xie, F. Wu, Y. Mei, Y. Hao, R. Huang, G. Wei, A. Liu, L. Li, R. Chen, *Adv. Mater.*, **33** (2021) 2101649.

[61] Y. Wang, B. Liang, J. Zhu, G. Li, Q. Li, R. Ye, J. Fan, C. Zhi, *Angew. Chem., Int. Ed.*, **62** (2023) e202302583.

[62] N. Mittal, A. Ojanguren, D. Kundu, E. Lizundia, M. Niederberger, *Small*, **19** (2023) 2206249.

[63] J. Xu, X. Ji, J. Zhang, C. Yang, P. Wang, S. Liu, K. Ludwig, F. Chen, P. Kofinas, C. Wang, *Nature Energy*, **7** (2022) 186-193.

[64] F. Zhang, T. Liao, C. Liu, H. Peng, W. Luo, H. Yang, C. Yan, Z. Sun, *Nano Energy*, **103** (2022) 107830.

[65] S. Guo, L. Qin, J. Wu, Z. Liu, Y. Huang, Y. Xie, G. Fang, S. Liang, *Natl. Sci. Rev.*, (2024) nwae181.

Chapter 6 Conclusions and outlook

6.1 Conclusions

The culmination of this doctoral research presents significant advancements in the development of AZIBs through three progressive studies, each building upon the insights and breakthroughs of its predecessors. This body of work not only enhances our understanding of AZIBs technology but also sets a solid foundation for future explorations and applications in the field of advanced energy storage systems.

The first study introduces a novel fabrication method for Mn-based, free-standing, binder-free cathodes using CNTs of varying diameters. This technique notably increases the unit area mass loading while simultaneously boosting the ionic and electronic conductivity of the electrodes. By embedding Na-intercalated Mn oxide into three-dimensional networks of CNTs, a significant enhancement in the specific capacity of AZIBs has been achieved. The cathodes demonstrated not only a high mass loading of 5 mg cm^{-2} but also sustained excellent capacity performance across various cycling conditions. This performance underscores the effectiveness of integrating layered nanomaterials with CNTs networks, which serves as a scalable approach to achieving high material loading while maintaining high specific capacities.

The second study explored the co-intercalation of Na^+ and Cu^{2+} into birnessite manganese oxide cathodes, a strategy that proved highly effective in enhancing the electrochemical performance of AZIBs. This dual intercalation mechanism enhances electrochemical reactivity by amplifying the activation effect of Cu^{2+} on the Mn^{2+}/Mn^{4+} redox pair at the surface, while Na^+ helps stabilize the host structure during charge and discharge cycles. This approach not only improved the specific capacity and cycling stability but also facilitated a highly reversible process of manganese deposition and dissolution, particularly at higher mass loadings. The insights gained from this study regarding the role of Cu^{2+} in promoting the deposition and dissolution processes in the cathode are invaluable, offering a new dimension to the development of cathode materials for high-performance AZIBs.

The final study marks a significant leap by redesigning the lithium-ion battery production line to prepare practical MnO_2-based AZIBs, focusing on the role of enhanced proton storage. The introduction of HAc into the slurry mixing process led to substantial improvements in proton dehydration and insertion into the cathode material, which in turn increased the power density and boosted manufacturing capacity. This innovative approach not only reduced microstructural changes during electrochemical reactions but also lowered energy barriers, extending the battery's lifespan. The HAcT cathode materials demonstrated high mass loading and efficient proton dehydration and insertion mechanisms, significantly improving the cycle stability and high-rate capacity of high-loading cathodes.

Collectively, these studies represent a substantial contribution to the field of battery technology, particularly in the development of AZIBs. The methodologies developed and the findings obtained not only advance our understanding of material science and electrochemistry but also have practical implications for the production and application of AZIBs in real-world scenarios. The transition from surface reaction-dominated mechanisms to bulk intercalation/deintercalation-type mechanisms, as demonstrated in these studies, is particularly promising for enhancing the stability and electrochemical performance of cathode materials in high-loading conditions.

6.2 Outlook

As we stand on the threshold of transformative advances in AZIBs, it is crucial to consider the future directions and potential impacts of this emerging technology. The developments documented in this doctoral dissertation not only redefine the performance benchmarks for AZIBs but also open avenues for further research and application in energy storage systems. The integration of innovative materials, novel fabrication techniques, and enhanced electrochemical mechanisms documented in the preceding studies provides a robust framework for advancing AZIB technology. The outlook for AZIBs is broad, spanning improvements in material science, scalability of manufacturing processes, and expansion into new market segments.

(1) Scalability and Commercialization

One of the significant achievements of this research has been the demonstration of scalable fabrication techniques for high-performance AZIBs. The next steps would involve optimizing these manufacturing processes for commercial production. This includes refining the automated production line techniques to further reduce costs and increase the output while maintaining high quality and consistency of the battery units. The potential for scaling these technologies to meet industrial demands could revolutionize how energy storage systems are produced, making them more accessible and cost-effective.

(2) Integration into Grid Storage

The application of AZIBs in high-rate scenarios such as frequency regulation, regenerative braking and grid storage present a promising outlook. The superior safety profile, high power density, and fast charging capabilities of AZIBs make them ideal candidates to enhance the efficiency and performance of regenerative braking systems and power management. In the context of grid storage, AZIBs can play a crucial role in stabilizing renewable energy sources by providing quick energy discharge and recharge cycles, essential for frequency regulation and coping with intermittent energy supplies.

(3) Environmental Impact and Sustainability

As the global focus shifts towards sustainable and green technologies, the environmental impact of battery production and disposal becomes increasingly significant. Future research should also focus on the lifecycle analysis of AZIBs, exploring the environmental impacts associated with the extraction of raw materials, production processes, and end-of-life disposal or recycling. Developing strategies for recycling and reusing battery components, particularly the metallic elements like zinc and manganese, could mitigate the environmental impact and bolster the sustainability of AZIBs production.

(4) Policy and Regulatory Framework

The commercialization and widespread adoption of AZIB technology will require supportive policies and regulatory frameworks. This includes standards for safety, performance, and environmental compliance that are specifically tailored to the unique properties of AZIBs. Engaging with policymakers and stakeholders to develop these frameworks will be crucial in ensuring that AZIBs can be seamlessly integrated into existing and future energy systems.

(5) Academic and Industrial Collaboration

To harness the full potential of AZIBs, fostering collaboration between academia and industry is essential. Such partnerships can accelerate the translation of research findings into practical applications and commercial products. Additionally, interdisciplinary collaborations that bring together experts in materials science, electrochemistry, engineering, and environmental science can drive innovation and address the complex challenges associated with developing next-generation batteries. The future of AZIBs technology is vibrant and filled with potential. The continued exploration and development of AZIBs will not only push the boundaries of battery technology but also contribute significantly to the creation of sustainable and efficient energy storage solutions. The journey from laboratory research to real-world applications will require concerted efforts across multiple domains, promising exciting opportunities for innovation and advancement in the years to come.

Publication list

Books

- M. Titirici, X. **Gao**, et al. (2022) Roadmap on multivalent batteries. *Journal of Physics: Energy*
- G. He, C. Carmalt, I. Parkin, **X. Gao**, et al. (2022) Green Chemistry in Electrochemical Energy Storage Technologies: Chapter 2.1. *Singapore: World Scientific Publishing*
- W. Sun., C. Su, K. Ip, **X. Gao**, et al. (2021) *White Paper: Report on Innovation and Entrepreneurship in Universities of China and Portuguese-speaking Countries.* (Associate Editor-in-Chief). China, BJ: China Commerce and Trade Press - Forum for Economic and Trade Co-operation between China and Portuguese-speaking Countries (Macao)

Key Published Paper

- Gao, X., Dong, H., Su, C., Dai, Y., Liu, Y., Parkin, I. P., ... & He, G. (2025). Payback trade-offs from the electrolyte design between energy efficiency and lifespan in zinc-ion batteries. *Energy Environ. Sci.*, *18*(1), 13-18.
- Gao, X.*, Chen, Z., He, G. (2025). Unidirectional Ion Sieve Enabling High-Flux and Reversible Zinc Anodes. *ACS Nano*, *19*(15), 14987-15001.
- Gao, X., Shen, C., Dong, H., Dai, Y., Jiang, P., Parkin, I. P., ... & He, G. (2024). Co-intercalation strategy for simultaneously boosting two-electron conversion and bulk stabilization of Mn-based cathodes in aqueous zinc-ion batteries. *Energy Environ. Sci.*, *17*(6), 2287-2297.
- Gao, X., Dai, Y., Zhang, C., Zhang, Y., Zong, W., Zhang, W., ... & He, G. (2023). When it's heavier: interfacial and solvation chemistry of isotopes in aqueous electrolytes for Zn-ion batteries. *Angew. Chem., Int. Ed.*, *135*(16), e202300608.
- Gao, X., Wu, H., Su, C., Lu, C., Dai, Y., Zhao, S., ... & He, G. (2023). Recent advances in carbon-based nanomaterials for multivalent-ion hybrid capacitors: a review. *Energy Environ. Sci.*, *16*(4), 1364-1383.
- Dai, Y., Zhang, C., Li, J., Gao, X., Hu, P., Ye, C., ... & He, G. (2024). Inhibition of vanadium cathodes dissolution in aqueous Zn-ion batteries. *Adv. Mater.*, *36*(14), 2310645.

- Gao, X., Liu, K., Su, C., Zhang, W., Dai, Y., Parkin, I. P., ... & He, G. (2024). From bibliometric analysis: 3D printing design strategies and battery applications with a focus on zinc-ion batteries. *SmartMat*, *5*(1), e1197.
- Gao, X., Zhang, C., Dai, Y., Zhao, S., Hu, X., Zhao, F., ... & Carmalt, C. J. (2023). Three-dimensional manganese oxide@ carbon networks as free-standing, high-loading cathodes for high-performance zinc-ion batteries. *Small Structures*, *4*(5), 2200316.
- Gao, X., Sun, X., Liu, J., Gao, N., & Li, H. (2019). A carbon-based anode combining with SiOx and nanodiamond for high performance lithium ion battery. *J. Energy Storage*, *25*, 100901.
- Sun, X., Gao, X., Su, C., Cheng, W., Gao, N., Zhang, X., ... & Li, H. (2024). Nanodiamond-Assisted High Performance Lithium and Sodium Ions Co-Storage. *Energy Environ. Mater.*, *7*(6), e12749.
- Sun, X., Gao, X., Li, Z., Zhang, X., Zhai, X., Zhang, Q., ... & Li, H. (2024). Nanowires framework supported porous Lotus-carbon anode boosts lithium-ion and sodium-ion batteries. *Small Methods*, *8*(1), 2300746.
- Su, C., Gao, X., Liu, K., Dai, Y., Dong, H., Liu, Y., ... & He, G. (2024). From lab to market: a review of commercialization and advances for binders in lithium-, zinc-, sodium-ion batteries. *Nano Res. Energy*, *3*(1), e9120094.
- Dong, H., Hu, X., Liu, R., Ouyang, M., He, H., Wang, T., ... & He, G. (2023). Bio-inspired polyanionic electrolytes for highly stable zinc-ion batteries. *Angew. Chem., Int. Ed.*, *135*(41), e202311268.
- Chen, R., Zhang, C., Li, J., Du, Z., Guo, F., Zhang, W., ... & He, G. (2023). A hydrated deep eutectic electrolyte with finely-tuned solvation chemistry for high-performance zinc-ion batteries. *Energy Environ. Sci.*, *16*(6), 2540-2549.
- Dai, Y., Zhang, C., Zhang, W., Cui, L., Ye, C., Hong, X., ... & Mai, L. (2023). Reversible Zn metal anodes enabled by trace amounts of underpotential deposition initiators. *Angew. Chem., Int. Ed.*, *62*(18), e202301192.
- Zhang, W., Wu, Y., Dai, Y., Xu, Z., He, L., Li, Z., ... & Parkin, I. P. (2023). “Mn-locking” effect by anionic coordination manipulation stabilizing Mn-rich phosphate cathodes. *Chem. Sci.*, *14*(32), 8662-8671.
- Chen, R., Zhang, W., Huang, Q., Guan, C., Zong, W., Dai, Y., ... & He, G. (2023). Trace amounts of triple-functional additives enable reversible aqueous zinc-ion

batteries from a comprehensive perspective. *NanoMicro Lett.*, *15*(1), 81.

- Ouyang, Y., Li, X., Zhu, J., Zong, W., Dai, Y., Gao, X., ... & Liu, T. (2024). Interface-induced polymerization strategy for constructing titanium dioxide embedded carbon porous framework with enhanced chemical immobilization towards lithium polysulfides. *Nano Res.*, *17*(3), 1473-1481.
- Zhang, W., Dai, Y., Chen, R., Xu, Z., Li, J., Zong, W., ... & Parkin, I. P. (2023). Highly reversible zinc metal anode in a dilute aqueous electrolyte enabled by a pH buffer additive. *Angew. Chem., Int. Ed.*, *62*(5), e202212695.

Conference presentations

13th China Finance Summit, Beijing, China, UK (Oral Presentation)	2024
Faraday Institution Conference, Birmingham, UK (Poster Presentation)	2023
30th SCI-CSCST Conference, London, UK (Oral Presentation)	2023
Early Career Colloid Conference, Rutherford Appleton Laboratory, UK (Oral Presentation)	2023